Quantifying Wind Tunnel Effects on the Flying V

Thesis Report

AE5211: Thesis Flight Performance & Propulsion

Antonio Machado Jorge

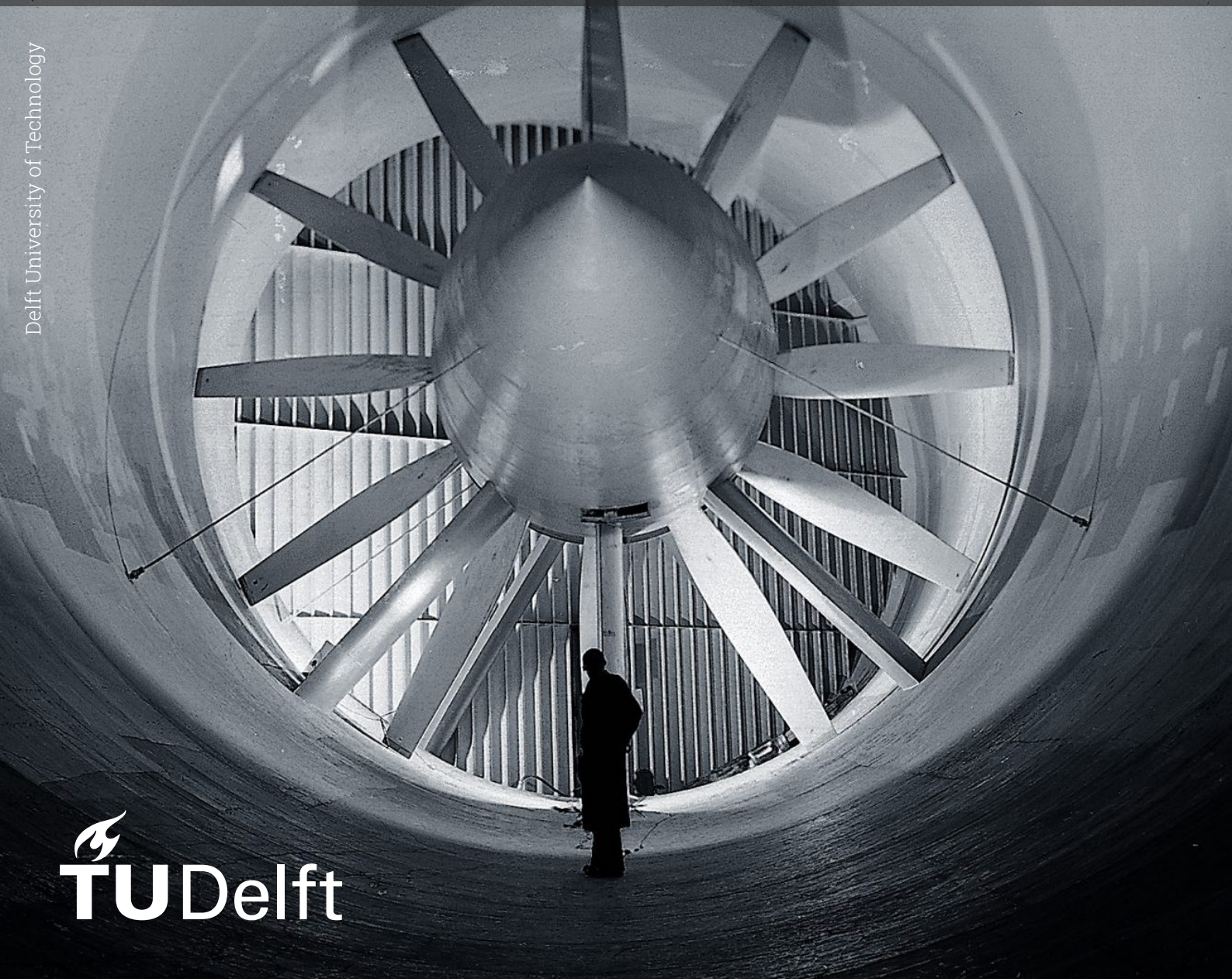

Delft University of Technology

TU Delft

Quantifying Wind Tunnel Effects on the Flying V

Thesis Report

by

Antonio Machado Jorge

to obtain the degree of Master of Science
at the Delft University of Technology,
to be defended publicly on Wednesday December 20, 2023 at 1:00 PM.

Student number:	4678915	
Project duration:	February 14, 2023 – December 8, 2023	
Thesis committee:	Dr. ir. R. Vos,	TU Delft, supervisor
	Dr. F. Oliviero,	TU Delft, chair
	Ir. N. van Luijk,	TU Delft, member

This thesis is confidential and cannot be made public until December 31, 2023.

Cover:	Altitude Wind Tunnel by NASA under CC BY-NC 2.0 (Modified)
Style:	TU Delft Report Style, with modifications by Daan Zwaneveld

An electronic version of this thesis is available at http://repository.tudelft.nl/.

TU Delft

Preface

Presenting this MSc thesis in Aerospace Engineering at Delft University of Technology marks the culmination of my academic journey. I want to express sincere thanks to my supervisor, Roelof Vos, and to Nikki van Luijk for their valuable insights. The collaborative spirit at Delft has been inspiring, and discussions with peers have shaped this work.

I'm grateful for the unwavering support of my family and friends. This thesis is a collective effort, reflecting the contributions of those who have been part of my academic adventure.

As this work joins the academic conversation, I hope it adds something meaningful to the field of Aerospace Engineering.

Antonio Machado Jorge
Delft, December 2023

Abstract

The present thesis report has been completed in advance of an ensuing research project, which is intended to establish the aerodynamic performance of the Flying V in an exhaustive experimental campaign at the Low Turbulence Wind Tunnel (LTT) of TU Delft. The report presents an advanced wind tunnel correction method to be used on the Flying V as a replacement for the classical corrections currently in place. These rely on the method of images, which cannot account for the interference effect of both the walls and the struts on the dominant aerodynamic phenomenon occurring over the Flying V: the leading edge vortices. By replacing the classical method with state-of-the-art computational fluid dynamics (CFD)-based corrections, researchers at the Flight Performance department of the Faculty of Aerospace Engineering at TU Delft will be able to more accurately predict the aerodynamic performance of the Flying V in free-air, whether in sub- or full-scale conditions, thereby advancing the development of this radical new sustainable aircraft design.

The report consists of two overarching parts: the literature study and the scientific article. In the former, literature relevant to the investigation was summarised, spanning recent developments on the Flying V, similar investigations at the LTT, classical and numerical wall interference corrections for both swept and straight wings, expected Reynolds number effects, CFD methods and limitations, and finally advanced approaches towards the design of experiments. In the scientific article, the development, implementation, validation and discussion of the correction method is discussed.

Starting with the literature study, it aggregates recent developments, at the time of writing, concerning the Flying V and similar investigations in the LTT. In a report by NASA, it was found that modelling the walls as viscous has a negligible effect on the solution, while drastically reducing the computational resources required. On the other hand, the effect of the shape of the numerical domain, or digital wind tunnel was unclear. Due to the up and downstream influence of the Flying V on the test section, it was found that both the contraction tube and diffuser should be fully simulated. Existing literature proved that, while popular for simple geometries, classical corrections fail to capture the effect of wind tunnel walls on the complex flow over highly swept wings, which is particularly sensitive to small geometric and attitude changes. Ultimately, it was found that not even more sophisticated empirical methods can account for wall effects on vortex breakdown over highly swept wings, a phenomenon known as the abrupt expansion and subsequent disorderly evolution of the typically well-organised, spiralling, leading-edge vortex flow over the upper surface. The suitability of RANS for numerical corrections was further confirmed by existing literature showcasing the flaws of various empirical methods at estimating the wall interference effects on slender wings. Lin et al. investigated the effect of the Reynolds number on the F19 configuration, which features a 65° leading edge sweep angle and an aspect ratio of roughly 1.5. The simulations primarily investigated the high subsonic regime, and the results showed that the separation behaviour is strongly dependent on the Reynolds number, with turbulence levels having a large effect on the total drag coefficient. At moderate Reynolds numbers, a separation bubble formed along the leading edge of the lambda wing. Furthermore, Hebbar et al. conducted an experimental study to investigate the influence of Reynolds number on vortex interactions/trajectories, and breakdown. The results showed that with an increase in Reynolds number, the strake and wing vortex trajectories tended to move outwards and closer to the model surface, and the vortex breakdown location moved forwards towards the apex of the model. These trends in the vortex interaction and bursting data were consistent with previous wind tunnel data. Concerning CFD methods, non-linear constitutive relations, high-quality meshes, and turbulence production limiters should all improve the prediction accuracy of common turbulence models, such as the SST $k-\omega$ or Spalart-Allmaras models in simulating the vortex flows over slender wings, such as the Flying V. The Euler equations, an inviscid, compressible version of the full Navier-Stokes equations may offer an acceptable level of accuracy at a significantly reduced computational cost. The one factor at a time (OFAT) approach for the design of the proposed investigation was found to not be suitable, since it is not effective at capturing interference effects which are paramount for the scope of the study. Furthermore, the behaviour of

the variables of interest is expected to be very non-linear with the input variables. The modern design of experiments (MDOE) approach focuses on the ability to predict data reliably, using collected data points, rather than directly measuring the responses at relevant points. Response surface modelling aims to build surfaces that accurately predict responses from a limited number of points. To that end, a bivariate non-linear response surface is proposed for the variables of interest using cubic splines. This should yield sufficient accuracy in regions that aren't explicitly measured in the experiment, making the results more useful as a tool to obtain corrections in later investigations. The cubic nature of the splines allows the surface to capture any non-linear effects either due to the input variables directly or due to any interference effects between the variables.

In the scientific article, the proposed method involves comparing the Flying V's aerodynamic performance in wind tunnel; 1.8%-scale, free-air; and full-scale, free-air conditions using RANS CFD. Sea level conditions are used, which, at an airspeed of 50 m/s, yield a chord-based scaled and full-scale Reynolds number of 1.2×10^6 and 62.7×10^6, respectively. The wind tunnel model pivots on two main struts, with a circular strut rigidly connected to the trailing edge of the root pitching the aircraft. The entire assembly yaws about a roof-mounted turntable. Integral forces and moments are presented for 16 equispaced combinations of angle of attack and sideslip, between $[0°, 32°]$, and $[0°, 25°]$, respectively. Thin plate splines are provided for data interpolation. Additionally, pressure coefficients and streamlines are presented on the aircraft surface, while pressure loss contours are shown for slices of constant x. It was found that the walls have a significant impact on the leading-edge vortices, causing them to break down prematurely. This phenomenon causes the aircraft to stall at a lower angle of attack compared to the free-air scenario. The latter of which shows mild separation at an angle of attack of 32°, despite the presence of strong leading-edge vortices. The full-scale model, on the other hand, does not show signs of stall up to the most extreme angle of attack of 32°. The angle of sideslip has a profound effect on the entire flow field over the aircraft, specifically on the strength, coherence and symmetry of the leading edge vortices. Classical corrections do not appear to account for this behaviour. An improved thin-plate spline-based surrogate model for the corrections is presented using the current results.

Contents

List of Figures

Nomenclature

Acronyms

Abbreviation	Definition
AIAA	American Institute of Aeronautics and Astronautics
APISAT	Asia-Pacific International Symposium on Aerospace Technology
CAD	Computer Aided Design
CFD	Computational Fluid Dynamics
DC	Direct Current
DDES	Delayed Detached Eddy Simulation
GP	Gaussian Process
IGES	Initial Graphics Exchange Specification
IPCC	Intergovernmental Panel on Climate Change
LDV	Laser Doppler Velocimetry
LES	Large Eddy Simulation
LH	Latin Hypercube
LS-BICSA	Least Squares Bi-Cubic Spline Approximation
LTT	Low Turbulence Tunnel
MDOE	Modern Design Of Experiments
NACA	National Advisory Committee for Aeronautics
NASA	National Aeronautics and Space Administration
NS	Navier-Stokes
OFAT	One Factor At a Time
OJF	Open Jet Facility
PIV	Particle Image Velocimetry
RANS	Reynolds-Averaged Navier-Stokes
RSM	Response Surface Modelling
SA	Spalart-Allmaras
SACCON	Stability and Control Configuration
SIMPLE	Semi-Implicit Method for Pressure Linked Equations
SST	Shear Stress Transport
STEP	Standard for the Exchange of Product Data
UCAV	Unmanned Combat Air Vehicles
VLM	Vortex Lattice Method

Symbols

Symbol	Definition	Unit
$\bar{c}$	Mean aerodynamic chord	m
C_L	Lift coefficient	-
C_D	Drag coefficient	-
C_y	Sideforce coefficient	-
C_m	Pitching moment coefficient	-
C_n	Yawing moment coefficient	-
K	Body shape factor	-
V	Volume of component	m^3
C	Cross sectional area of wind tunnel	m^2
b	Geometric span	m
b_e	Effective span	m
b_v	Effective vortex span	m
Re	Reynolds number	-
Ma	Mach number	-
ρ	Density	kg/m^3
ϵ	Blockage factor	-
τ	Tunnel factor	-
α	Angle of attack	deg
β	Angle of sideslip	deg
δ	Boundary correction factor	-
Λ_{LE}	Leading edge sweep	deg
ϕ	Roll angle	deg
δ_e	Elevon deflection	deg

Part I

Scientific article

Quantifying Wind Tunnel Effects on the Flying V

Antonio M. Jorge*
Delft University of Technology, Delft, 2629 HS, The Netherlands

This article presents an advanced wind tunnel correction method to be used on the Flying V in its experimental campaign in the Low Turbulence Wind Tunnel at TU Delft. Due to strong vortices formed over the leading edge of the Flying V, the classical method of images typically employed is not expected to accurately correct for wall and strut effects, potentially hampering the development of the aircraft. The proposed method involves comparing the Flying V's aerodynamic performance in wind tunnel; 1.8%-scale, free-air; and full-scale, free-air conditions using RANS CFD. Simulations are conducted under sea-level conditions at an airspeed of 50 m/s. The wind tunnel model, mounted on a turntable, incorporates pivotal main struts and a circular aft strut. Sixteen equispaced combinations of angle of attack and sideslip are investigated between $[0°, 32°]$, and $[0°, 25°]$, respectively. Thin-plate splines are provided for data interpolation. The current procedure is validated using external experimental and numerical data from the F19 aircraft. The method was found to match the external data to an acceptable level of accuracy, with an RMSE in the lift coefficient of 0.111 relative to the experiment and 0.073 relative to the CFD data. Through integral force and moment polars, total pressure loss contours, surface pressure coefficients and surface streamlines, the investigation reveals a significant influence of walls on leading-edge vortices, causing premature vortex breakdown and lower stall angles in confined conditions compared to free-air scenarios. The full-scale model exhibits resilience against stall up to extreme angles of attack, emphasising the effect of the Reynolds number. The angle of sideslip profoundly affects the overall flow field, particularly the strength, coherence, and symmetry of leading-edge vortices. Classical corrections are identified as insufficient in capturing this nuanced behaviour. An improved thin-plate spline-based surrogate model for the corrections is presented using the current results.

Nomenclature

α	=	Angle of attack
$\bar{c}$	=	Mean aerodynamic chord
β	=	Angle of sideslip
$\mathbf{a}$	=	Vector of interpolation coefficients
$\mathbf{c}$	=	Vector of interpolation centres
$\mathbf{x}$	=	Attitude vector
μ_∞	=	Freestream dynamic viscosity
Ψ	=	Radial basis function
ρ_∞	=	Freestream density
b	=	Aircraft span
C_p	=	Pressure coefficient
$C_{[]}$	=	Aerodynamic coefficient
D	=	Integral drag force
f	=	Thin-plate spline
L	=	Integral lift force
l	=	Integral rolling moment
m	=	Integral pitching moment
n	=	Integral yawing moment
p	=	Static pressure
S	=	Wing area
V_∞	=	Freestream airspeed
Y	=	Integral sideforce
y^+	=	Dimensionless wall distance

*MSc Student, Flight Performance and Propulsion Section, Faculty of Aerospace Engineering

I. Introduction

The Flying V is a novel aircraft configuration conceived at Airbus Future Projcts and actively being developed by TU Delft. By completely changing the aircraft architecture, the Flying V aims to provide a platform for significant efficiency gains, in contrast to conventional designs which have only seen improvements in the order of 3% a year over the past decade and a half[1]. Unlike traditional aircraft designs with a fuselage and separate wings, this effort integrates the wing and fuselage into a single structure. The Flying V also incorporates a crescent wing shape, seen in Fig. 1. By reducing fuel consumption and emissions, this innovative design could help to mitigate the impact of aviation on the environment, while also providing a more comfortable and efficient passenger experience [1]. As research on the Flying V progresses, the Faculty of Aerospace Engineering at TU Delft is preparing for an experimental campaign at the Low Turbulence Wind Tunnel (LTT). The data from this experiment will help refine the understanding of the aerodynamic performance of the aircraft, and elucidate the complex flow phenomena around the Flying V.

The presence of the wind tunnel walls and support struts may heavily influence the flow around the test article, leading to altered data measurements. The difference in results can vary greatly depending on the geometry of the test article and wind tunnel, as well as the testing conditions. To overcome this interference, comprehensive wind tunnel corrections have been developed which are successful in accounting for these effects over a large range of scenarios. Typically, the LTT employs the method of images for its corrections, which is not valid for the flow around the Flying V since it does not account for the influence of the dominant flow phenomenon at high angles of attack: leading edge vortices. In an effort to advance the accuracy of the corrections and simultaneously gain insights into the Flying V's aerodynamic behaviour, this investigation uses computational fluid dynamics (CFD) to identify the wind tunnel effects on the Flying V. Unlike the method of images, this approach should resolve the leading edge vortices which are formed over the suction side of the aircraft and account for their influence on the flow field.

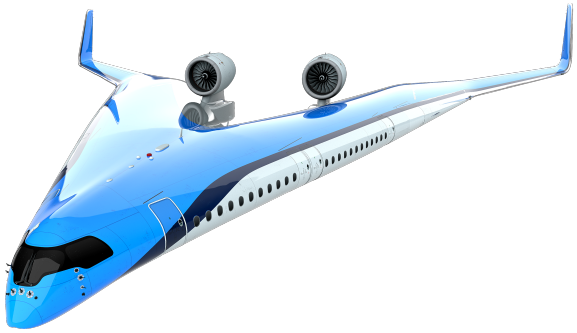

Figure 1. Artistic rendition of the Flying V

The article is structured as follows: in Section II, the numerical methodology is reported along with a description of both the test article and wind tunnel. In Section III, the overarching method is validated using experimental and numerical data from external investigations of the F19. In Section IV, the corrections are shown, alongside an interpretation which makes use of the integral forces, moments, and predicted flow field around the Flying V. These are compared against the classical method. Subsequently, the quality of the thin-plate spline interpolation is evaluated, and the surrogate correction model is introduced. Finally, in Section V, the conclusions are drawn, including limitations, recommendations, and future work. Supporting work can be found in Appendices A to K.

[1] http://bit.ly/3MwSquO, accessed on 7 Nov. 2023

II. Methodology

To identify the wind tunnel effects, three scenarios are compared, namely: the wind tunnel scenario, including walls and struts; the sub-scale, free-air scenario, where the aircraft features the same 1.8%-scale as the wind tunnel model; and finally the full-scale, free-air scenario. This arrangement allows for an independent comparison of the effect of the walls and struts, and the effect of increasing the Reynolds number by a factor of 54. Reynolds-Averaged Navier-Stokes (RANS) simulations are used to calculate the flow field around the Flying V. Integral forces and moments are presented for a range of angles of attack, α, between 0° and 32° in increments of 10.66°, and a range of angles of sideslip, β, between 0° and 25° in increments of 8.33°, both at a chord-based Reynolds number of 1.16×10^6 and 62.7×10^6. Due to the limited number of runs, thin-plate spline interpolation is applied to increase the resolution of the force and moment data.

A. Model Description

The current iteration of the Flying V geometry stands as the most recent update, aggregating developments in aerodynamics, structures, flight dynamics and even interior design. Changes at this step of the design process are expected but should not lead to any large changes in the performance of the aircraft - it can be assumed that analyses of this iteration will capture the effects of the walls, struts and Reynolds number accurately, even for future design revisions. Thus, the full-scale geometry illustrated in Fig. 2, should be representative of the final test article. In Fig. 2b, the main and aft struts are visible. The mean aerodynamic chord ($\bar{c}$) of the Flying V is referenced from previous investigations and measures 18.3 m [2]. All moments are calculated about the model's centre of volume, indicated as the moment reference point (MRP) in Fig. 2a.

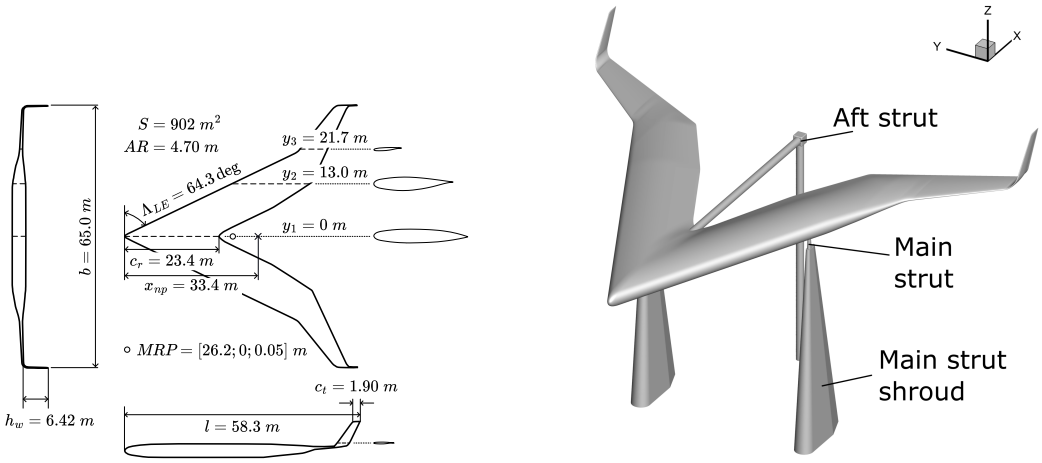

(a) Schematic view including dimensions **(b) Isometric view including support struts**

Figure 2. Geometry of the Flying V

The main struts are reused from previous LTT experiments, with the tapered shroud extended upwards such that there is a clearance of around 5 cm between them and the aircraft to minimise interference on the balance measurements. These are fixed on the aircraft 23.2 cm outboard of the root, and 58.5 cm aft of the nose - slightly ahead of the aircraft's neutral point (x_{np}), calculated by Laar [3], to ensure that the assembly is stable. Two cylindrical rods of 2 cm diameter comprise the aft rod which serve to pitch the aircraft. Their circular cross-section is intended to minimise the frontal area, and hence sideforce under the sideslip, at the cost of increased vortex-shedding. The fork joint between the vertical and horizontal members of the aft strut is modelled as a cube with rounded corners of 2.5 cm radius. The horizontal member of the aft strut is rigidly connected to the aircraft at the trailing edge of the root. Future developments of the Flying V geometry are expected to feature

a small tail at this location which forms a natural connection point for a strut. While it may not be ideal for this iteration of the Flying V, the struts are configured for the most likely design at the time of the experiment.

Lastly, the LTT geometry is taken from existing sources [4] and is summarised in Fig. 3a. This atmospheric, closed-throat, single-return type tunnel features an octagonal test section measuring 1.80 m wide, 1.25 m tall, and 2.60 m long. For RANS simulations, it is known that both the inlet and outlet should be placed at a significant distance from the aerodynamic body, typically at least ten body lengths from the outlet, and slightly less from the inlet [5]. Using the test section as the domain breaks this convention and would very likely introduce inaccuracies or artefacts into the solution. In order to obtain a sufficiently long domain, both the contraction chamber and diffuser are included, as seen in Fig. 3b. The LTT's test section is slightly diverging, such that the area in the throat excluding the boundary layer is constant along its length. This taper is carefully designed to ensure that no buoyancy corrections are needed. In the numerical simulations, the walls are treated as inviscid and the test section walls can be made parallel to emulate this behaviour [6].

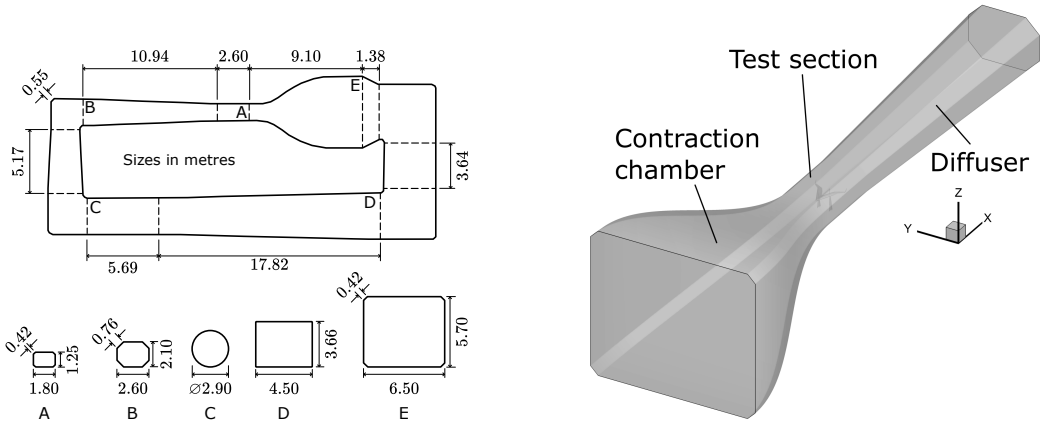

(a) Schematic view including dimensions **(b) Isometric view including support struts**

Figure 3. Geometry of the LTT

B. Computational Setup and Strategy

ANSYS Fluent® 2021R2, an unstructured finite-volume cell-centred solver, is used to perform the simulations. Across all simulations, the flow is prescribed to be fully turbulent; while it may be laminar in the wind tunnel in certain cases, it is assumed that the flow will be adequately tripped over the surfaces since this more closely mimics the boundary layer behaviour at larger Reynolds numbers. The *curvature correction* option is enabled to prevent the erroneous build-up of turbulence viscosity in the vortex cores [7, 8]. Due to a limitation in the meshing software, the y^+ value is maintained under 10, rather than the ideal limit of 1. The effectiveness of this method's y^+ insensitive wall treatment is evaluated in Section III. First-order spatial discretisation schemes are used for density, momentum, turbulence kinetic energy, specific rate of dissipation, and temperature over the first 2 000 iterations, or until the solution stabilises, after which point all spatial discretisation schemes are changed to second-order. These are paired with the PRESTO! pressure interpolation scheme due to its higher stability under the presence of highly rotating flows, such as those in vortex cores[2]. For the equation of state, the fluid is assumed to be an ideal gas using Sutherland's three-coefficient method to calculate the dynamic viscosity as a function of temperature. Gradients are calculated using the Least Squares Cell-Based method. Lastly, Fluent's hybrid initialisation is used for the free-air simulations, while full multigrid (FMG)

[2] www.afs.enea.it/project/neptunius/docs/fluent/html/ug/node331.htm, accessed on 28 Sept. 2023

initialisation is used for the wind tunnel tests. These settings enable the simulations to be run on the available hardware at a reasonable compromise of speed, robustness and accuracy. A data-driven approach is taken towards choosing the turbulence model and pressure-velocity coupling which is detailed in Section III.

The domains and boundary conditions for the confined and free-air simulations differ substantially. The free-air simulations feature a cubical domain which extends ten times the largest dimension of the Flying V in all directions. A velocity inlet is defined on five faces, with a pressure outlet on the rear face. The velocity is set to 50 m/s at sea-level conditions. On the other hand, the wind tunnel domain features a pressure inlet, slip walls, a pressure outlet and no-slip aircraft and strut walls. The total pressure and temperature at the inlet are set to 102 856 Pa and 289.94 K respectively, while the static pressure at the outlet is set to 102 623 Pa. Assuming constant mass flow, an empty tunnel and standard sea-level conditions at the throat yields an airspeed of 2.8 m/s, 50 m/s and 19.5 m/s at the inlet, throat and outlet, respectively. Both domains are shown in Fig. 4. The turbulence level is taken as 0.06% in the wind tunnel, slightly below its maximum level of 0.07% at 75 m/s. The free-air scenarios, on the other hand, assume a turbulence level of 0.1% [5]. Across all simulations, a non-zero operating pressure of 101 325 Pa is used to avoid round-off errors since at these Mach numbers ($M \approx 0.15$), the changes in pressure induced by the model are small relative to the freestream static pressure[3].

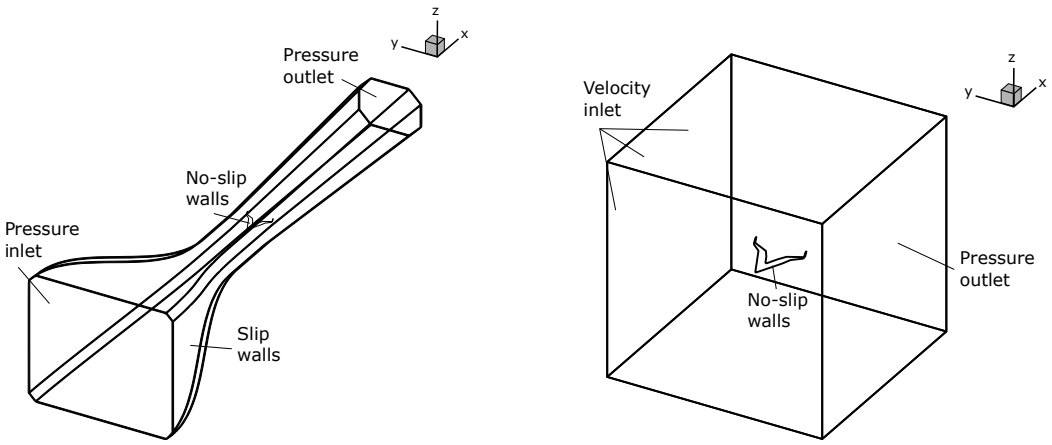

(a) Wind tunnel **(b) Free-air**

Figure 4. Schematic view of simulation domains

C. Classical Corrections

The high-fidelity wind tunnel corrections in this article are benchmarked against the classical corrections currently in place at the LTT, which are calculated using the method of images. This method involves emulating the true conditions inside the wind tunnel using the Laplace equation for irrotational flow. This is done through the rigorous use of singularities (e.g., sources, sinks, doublets), with their exact distribution in the domain being a function of the model geometry, wind tunnel geometry, and flow conditions. It is then assumed that the solution to this system is a sufficiently close approximation of an equivalent solution to the Navier-Stokes equations. The direct solution of the Navier-Stokes equations is not used because it is often too expensive to obtain. Barlow et al. summarised the results from several sources using the data to present various correction models that take as inputs the aircraft performance and geometry as well as the

[3] www.afs.enea.it/project/neptunius/docs/fluent/html/ug/node331.htm, accessed on 2 Oct. 2023

test section shape and output the changes in forces and moments [9]. This allows for the corrections to be calculated without having to model the wind tunnel numerically with the method of images. The accuracy of the aforementioned models pivots on two fundamental assumptions:

1) There is a large volume of irrotational flow between the rotational flows at the test article and the walls for which the Laplace equation is a satisfactory model.
2) The boundary conditions are imposed in such a way that the solution is indeed representative of the equivalent Navier-Stokes solution.

It is not immediately clear that both assumptions are satisfied in these wind tunnel tests. Foremost, at certain conditions, the Flying V generates strong vortices over its leading edge, which flow downstream. This implies there is a large volume of rotational flow in the domain, in between the rotational flows past the walls and the aircraft. While it can be argued that this phenomenon can be modelled with vortex singularities, Barlow et al.'s implementation of the method of images does not account for this additional vorticity. Secondly, the Flying V features a very complex geometry, which similarly is not accounted for in Barlow et al's implementation. Examples include the kink between the inboard and outboard sections of the wing, the large sweep angle, and the curved winglets. Only panel methods can take into account such complex geometries but these do not offer superior accuracy to Navier-Stokes codes while still requiring a significant time and skill investment, albeit at a lower computational cost [9]. RANS has the advantage of not only providing high-fidelity insights into wind tunnel effects but, in doing so, also offering insights into the test article's performance and surrounding flow field. The effectiveness of the classical corrections is evaluated in Section IV.

D. Data Extraction

In Eqs. (1) to (6), the equations for the force and moment coefficients are shown. They are defined as positive in the forward direction relative to the airspeed axes - these are obtained by rotating the aircraft body reference axes seen in Fig. 2b around the z axis by β, followed by a rotation around the y axis by α. The moments follow the same convention using the right-hand rule.

$$D = C_D \frac{1}{2}\rho_\infty V_\infty^2 S \quad (1) \qquad Y = C_Y \frac{1}{2}\rho_\infty V_\infty^2 S \quad (2) \qquad L = C_L \frac{1}{2}\rho_\infty V_\infty^2 S \quad (3)$$

$$l = C_l \frac{1}{2}\rho_\infty V_\infty^2 b S \quad (4) \qquad m = C_m \frac{1}{2}\rho_\infty V_\infty^2 \bar{c} S \quad (5) \qquad n = C_n \frac{1}{2}\rho_\infty V_\infty^2 b S \quad (6)$$

In Eqs. (1) to (6), ρ and V, relate to the density and airspeed, respectively, with the '∞' subscript denoting freestream conditions. The integral drag, sideforce, lift, rolling moment, pitching moment and yawing moment are denoted by D, Y, L, l, m, n, respectively. In addition to this, the pressure coefficient is also presented over the aircraft using the relation given in Eq. (7). The Reynolds number is calculated with respect to the mean aerodynamic chord - its formula is shown in Eq. (8), where μ_∞ is the freestream dynamic viscosity of air. The aircraft parameters used for non-dimensionalisation are summarised in Table 1. Standard sea-level conditions are used for the density, pressure, temperature and viscosity. At an airspeed of 50 m/s, this yields a freestream Mach number of 0.147.

$$C_p = \frac{p - p_\infty}{\frac{1}{2}\rho_\infty V_\infty^2} \quad (7) \qquad Re = \frac{\rho_\infty V_\infty \bar{c}}{\mu_\infty} \quad (8)$$

Table 1. Sub- and full-scale Flying V parameters

Parameter	Symbol	Scaled value	Full-scale value	Units
Mean aerodynamic chord	$\bar{c}$	0.338	18.3	m
Aircraft span	b	1.20	65.0	m
Wing area	S	0.307	902	m^2
Reynolds number	Re	1.16×10^6	62.7×10^6	-

E. Interpolation Method

The test matrix for this investigation is relatively coarse; it features four points in both α and β, including every combination of the two for a total of 16 points. Across all 16 combinations, 6 different coefficients are calculated. Interpolation is used to obtain refinements in the coefficients within the equispaced intervals. *Thin-plate splines* can accommodate the non-linearity of the results in a portable format, with minimal artefacting.

A thin-plate spline is constructed by placing radial basis functions (RBFs) at various combinations of the input variables. For instance, every combination of β and α. A bilinear polynomial may be superimposed with these basis functions to improve the quality of the interpolation. The surface is mathematically described by the sum of these basis functions with the polynomial, each multiplied by a coefficient which can be tuned. The coefficients are obtained by forcing the surface to lie on an arbitrary set of input data. In the case of interpolating a coefficient of the Flying V, using as input the predicted values at the 16 combinations of α and β, it takes 16 coefficients to describe the basis functions, with another three coefficients being used for a bilinear polynomial component. With these coefficients, the model can easily be rebuilt retroactively. MATLAB®, for instance, features a built-in function which takes as input these coefficients and the basis function centres and outputs the interpolation function (see `stmak`)[4].

The equation of a surface, f, obtained with thin-plate spline interpolation with 19 coefficients is shown in Eq. (9), where $\mathbf{x}$ is the attitude vector, $[\beta, \alpha]$; $|\mathbf{x}|$ is the Euclidean norm of a vector $\mathbf{x}$; $\Psi(r)$ is the radial basis function, $\Psi(r) = r \log r$; $\mathbf{a}$ is the vector of interpolation coefficients; and $\mathbf{c}$ is the vector of interpolation centres, taken as the combinations of β and α. The coefficients are calculated using MATLAB®'s `tpaps`[5].

$$f(\mathbf{x}) = \underbrace{\sum_{j=1}^{n=16} \mathbf{a}_j \cdot \Psi\left(|\mathbf{x} - \mathbf{c}_j|^2\right)}_{\textit{Scaled radial basis functions}} + \overbrace{\mathbf{a}_{17} \cdot \beta + \mathbf{a}_{18} \cdot \alpha + \mathbf{a}_{19}}^{\textit{Bilinear polynomial}} \tag{9}$$

[4] https://nl.mathworks.com/help/curvefit/stmak.html, accessed on 23 Oct. 2023
[5] https://nl.mathworks.com/help/curvefit/tpaps.html, accessed on 17 Nov 2023

III. Validation

To establish the accuracy of the current method, and to gain confidence in the quality of the results, the current procedure is validated using external experimental and numerical data from the DLR F-19, also known as the Stability and Control Configuration (SACCON). This particular aircraft was chosen for its geometrical similarities with the Flying V, namely, its large leading edge sweep angle. This entails that both form strong vortices over the leading edge at moderate to high angles of attack. This validation is intended to provide a data-based approach towards tuning the mesh refinement and solver settings while also quantifying the current method's ability to predict highly vortical flows.

A. Meshing Strategy

Due to the complexity of the flow around the Flying V, the meshing strategy must be carefully considered. RANS's ability to predict nuanced flow structures, such as vortices, is highly dependent on the mesh resolution and quality [10]. The DLR F19, whose geometry is shown in Fig. 5, is used as a test bench to identify the most appropriate meshing strategy in terms of accuracy and performance.

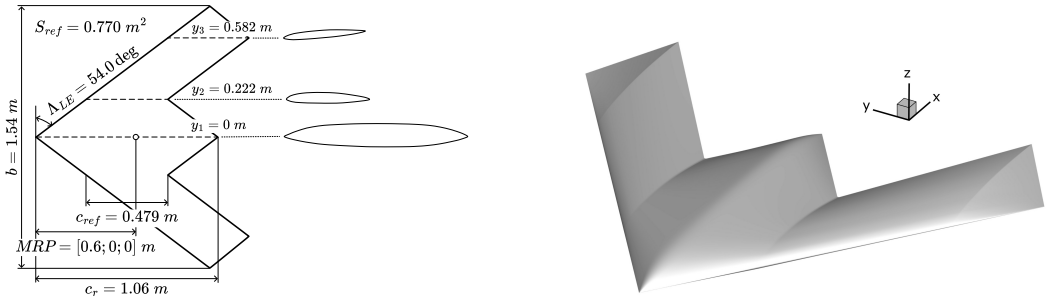

(a) Schematic view including dimensions **(b) Isometric view**

Figure 5. Geometry of the DLR F19

The current version of the F19 features a truncated trailing edge which was discretised into four cells along its width for the baseline mesh. This avoids the formation of poor-quality elements around this region, such as highly skewed cells, or excessive volume ratios. A local sizing is added to the aircraft, such that the maximum curvature allowed is 5°, with a maximum size of 1.5 mm and a minimum size of 0.2 mm. A body of influence (BOI) with a local cell size of 20 mm encases the aircraft to enhance the prediction of off-body phenomena such as flow separation or vortices. The cell size at the inlet and outlet of the domain is fixed at 5 m. The aircraft features 30 inflation layers with a first-layer height of 7 μm. For the mesh refinement study, the surface grid is coarsened by a factor of 2 for the coarse mesh, and refined by a factor of 1.5 for the fine mesh. This yields a coarse mesh with 16.3×10^6 elements, a baseline mesh with 41.0×10^6 elements, and a fine mesh with 94.9×10^6 elements. The lift, drag and pitching moment polars for each variation are compared against the baseline alongside experimental and numerical data from Frink et al. [11] in Fig. 6. The latter employs EDGE's[6] implementation of Detached Eddy Simulations (DES) with the Spalart-Allmaras turbulence model and a static mesh. The inclusion of external numerical data allows for an evaluation of the method's implementation (verification), while the experimental data allows for an evaluation of the method's accuracy (validation). The exact simulation conditions for the validation study can be found in Table 5.

[6] https://www.foi.se/rest-api/report/FOI-R--0298--SE, accessed on 7 Dec. 2023

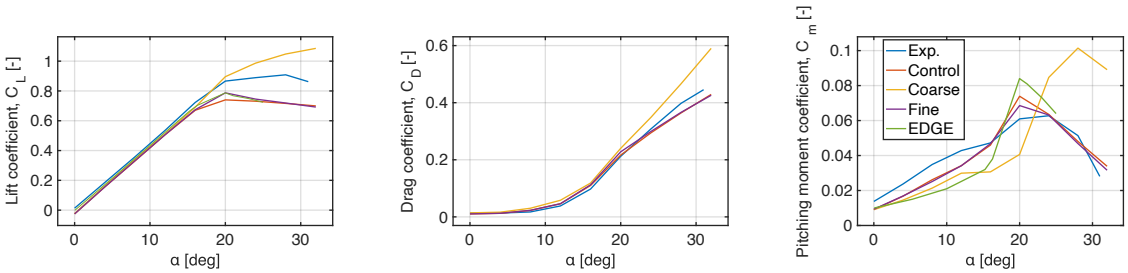

(a) Lift **(b) Drag** **(c) Pitching moment**

Figure 6. F19 polars for different mesh refinement levels

B. Solver Tuning

In addition to the mesh refinement study, the influence of the turbulence model, pressure-velocity coupling scheme, and y^+ value are also investigated. For the latter, the baseline mesh is adapted to feature a y^+ value no greater than ten versus the default value of one. This comparison is necessary due to the meshing software's inability to produce elements of sufficient quality at very low first-layer heights over highly curved surfaces, which is the case for the Flying V at high Reynolds numbers. The turbulence model and pressure-velocity coupling scheme are investigated to identify a compromise between speed and accuracy. The baseline case consists of a mesh with 41.0×10^6 elements, the $k-\omega$ turbulence model, the SIMPLE pressure-velocity coupling scheme, and a y^+ value no greater than one across the surface of the aircraft. The comparisons to the experimental and numerical results are shown in Figs. 7 to 9.

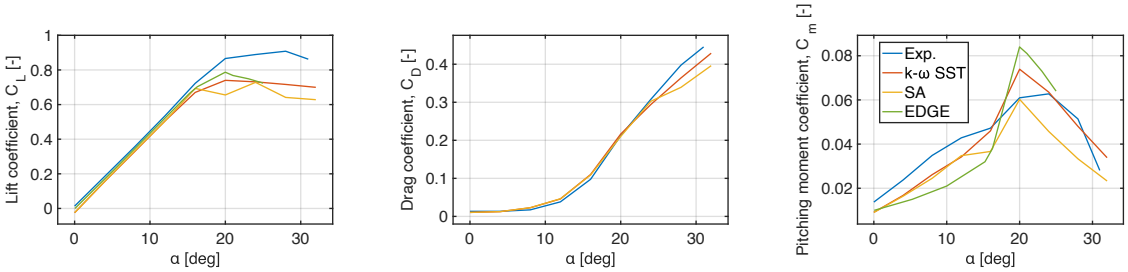

(a) Lift **(b) Drag** **(c) Pitching moment**

Figure 7. F19 polars for different turbulence models

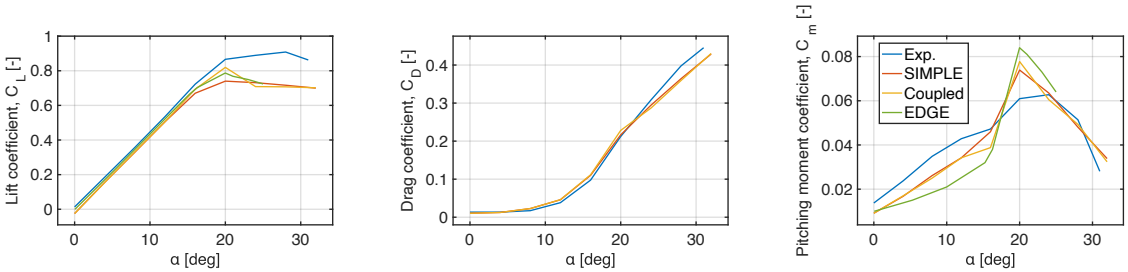

(a) Lift **(b) Drag** **(c) Pitching moment**

Figure 8. F19 polars for different pressure-velocity coupling schemes

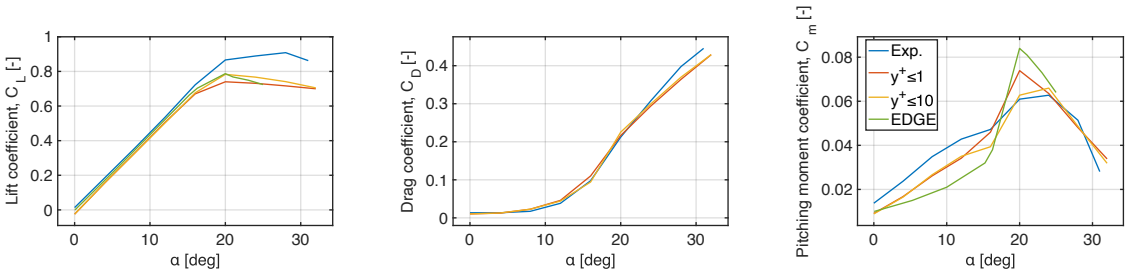

(a) Lift **(b) Drag** **(c) Pitching moment**

Figure 9. F19 polars for varying levels of maximum y^+

C. Chosen Settings

The solver settings must strike a balance between performance, accuracy and robustness. The CPU time is calculated for the entire angle of attack sweep, with each variant being benchmarked against the control configuration. Both the CPU time and the root-mean-square error (RMSE) relative to external data are shown in Table 2.

Naturally, there is a large sensitivity to the mesh refinement level. The coarse mesh, despite featuring roughly 60% fewer elements, takes only a staggering 6% of the time to run. Similarly, the fine mesh features 131% more elements yet takes 193% longer to run. The coarse mesh does not yield sufficiently accurate results, while the fine mesh almost perfectly matches the numerical work of Frink et al. Yet it still does not perfectly replicate the experimental data despite the enormous cost. Given that the flow over the Flying V should not be as challenging to simulate, the baseline mesh emerges as the strongest choice. Furthermore, the Spalart-Allmaras turbulence model does not offer either a convincing performance increase or improved data agreement with the experiment. The coupled pressure-velocity scheme yields virtually identical results to the SIMPLE algorithm at a significantly higher cost, while the lower y^+ value offers comparable results with a reduction of over a third in computational cost. Given the meshing software's limited ability to generate thin elements at the wall, the latter is considered an acceptable compromise taking into account the scope and hardware availability of the current work. Taking all of the above in mind, the baseline configuration appears as the best choice in terms of speed, accuracy and robustness - concerning the latter, none of the simulations show significant differences in convergence stability.

Table 2. Summary of F19 simulation performance and accuracy

Variant	Nodes	CPU hours	Difference	RMSE in lift coefficient	
				wrt. exp. [11]	wrt. EDGE [11]
Control	384	326	-	0.111	0.0730
Spalart–Allmaras	384	347	+6.40%	0.149	0.0949
Coarse mesh	384	19.0	-94.2%	0.0963	0.188
Fine mesh	384	955	+193%	0.104	0.0704
Coupled scheme	576	610	+87.1%	0.108	0.0733
$y^+ \leq 10$	384	209	-35.9%	0.0949	0.0701

D. Method Evaluation

In general, the results show reasonable agreement with the experimental data, with the drag predictions being particularly accurate. The moment predictions are the least accurate as to be expected, since it is well known that RANS approaches tend to struggle in this regard [11, 12]. These conclusions practically mirror those presented by Frink et al. In fact, their numerical results show excellent agreement with the current work, particularly the results from the finest mesh. Frink et al. found that it was 'extremely difficult' to model the vortical flow over the round leading edge of the F19 [11], with the methodologies of the time (2011). Even the same discrepancies were found in the moment coefficient predictions. Upon closer inspection of the flow field, it seems as though the same vortical structures are present in both the experimental and numerical results, although the dynamics of the numerical system show a very high sensitivity to changes in turbulence model, and grid refinement. This is particularly true at high angles of attack, where the correlation between the models is the weakest. Figure 10 shows the surface streamlines, or friction lines, over the F19's upper surface overlaid with the local pressure coefficient. The comparison is made between the current work, which uses ANSYS Fluent® with the $k-\omega$ turbulence model, and NASA's USM3D[7] which in this case, implements the Spalart-Allmaras turbulence model. The figure illustrates how even the numerical methods can feature significant discrepancies in the triple vortex system, despite the agreement in forces and moments. It then follows that the triple vortex system should be examined in more detail.

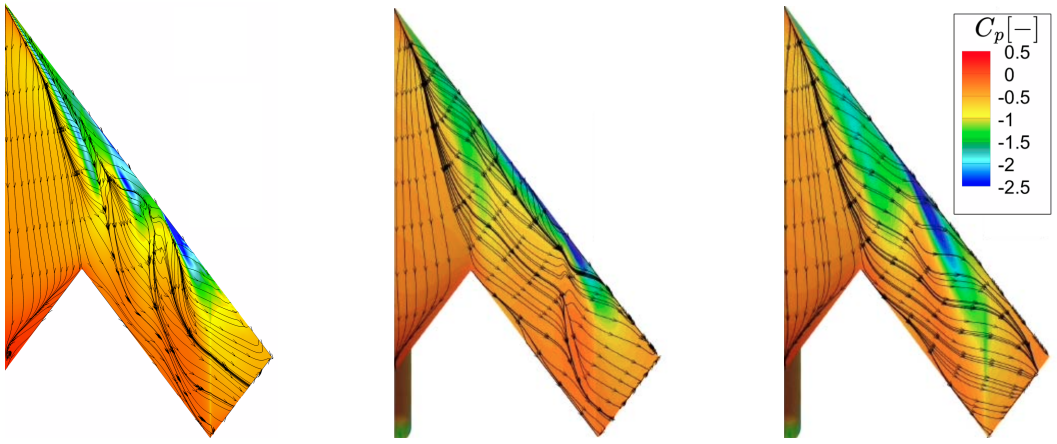

(a) Current work (α = 16.0°) **(b) USM3D-SA** (α = 16.83°) **[11]** **(c) USM3D-SA** (α = 17.89°) **[11]**

Figure 10. F19 pressure coefficient contours and surface streamlines

Figure 11 shows the vorticity contours at various slices of constant x along the aircraft's length. Particle image velocimetry (PIV) data is available from Loeser et al. [13], while reference RANS CFD data is available from Frink et al. [11]. Two important conclusions can be drawn. The first of which is that both CFD approaches overestimate the vorticity at the vortex cores. While the work of Frink et al. overestimates the values at the cores and further off-body, the current work seems to overestimate at the vortex cores and within the boundary layer. The current work features a higher flow resolution, which presumably leads to the clear development of the triple vortex system, albeit to an exaggerated degree compared to the PIV data. The vortex system consists of an 'apex vortex', formed at the apex due to the local sharpness of the leading edge; a 'thickness vortex' formed further outboard due to the separation over the wing which forms near the transition from a sharp to a round leading edge; and a 'tip vortex' slightly inboard of the wingtip. The challenge of predicting these vortical flows correctly lies in accurately predicting the location of these vortices as their interaction will largely dictate the pressure field over the leeside of the wing [14].

[7] https://software.nasa.gov/software/LAR-16670-GS, accessed on 11 Oct. 2023

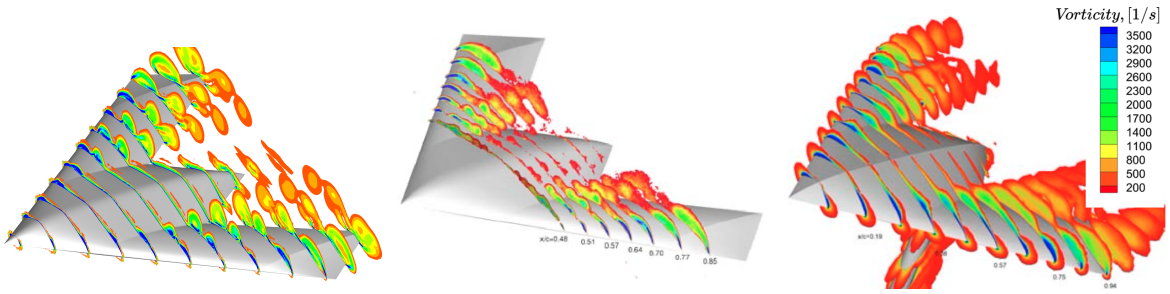

(a) Current work (α = 16.0°) **(b) PIV** (α = 16.9°) **[13]** **(c) USM3D-SA** (α = 16.83°) **[11]**

Figure 11. F19 off-body vorticity at slices of constant x

To conclude, this section should elucidate the difficulty of predicting highly vortical flows. Despite the underwhelming agreement with the experiment, the results show that the method is correctly implemented, with the data in line with that of Frink et al. This should inspire confidence in the quality of the data since the reference work coalesces efforts from the National Aeronautics and Space Administration (NASA), the Swedish Defence Research Agency (FOI) and the Defence Science and Technology Group (DSTO). While the flow over the Flying V is also highly vortical, the same challenges should not arise, at least not to the same degree, in simulating its flow field. In part, this is due to the simpler geometry of the Flying V - the vortex locations are fixed at the apex and at the wing kink. The F19 features a nuanced leading edge and upper surface which make for a more complicated flow field. With this in mind, the results from the current work should still be considered with some reservations, as it has been proven that RANS approaches with static meshes are not always able to exactly model highly vortical flows. For a higher degree of confidence in the results, it is recommended that DES are considered since they apply more detailed physics fundamentally, and also yield a time-dependent solution, which may capture vortex breakdown more accurately. It is also suggested that this is paired with a dynamically refining mesh - with this approach the mesh at the vortex cores can be automatically refined based on the local solution gradients. This ensures better resolution of the vortices at a non-prohibitive cost. Neither of these recommendations was possible to implement due to the scale of the investigation, hardware availability and software restrictions.

IV. Results

In this section, the meshing process for the Flying V is described, followed by a discussion on the convergence and performance of the simulations. Once the quality of the simulations is assured, the wall and strut corrections are introduced - these are defined as the delta between the confined and free-air, sub-scale simulations. These results are followed by the Reynolds number corrections, which similarly are defined as the delta between the full- and sub-scale simulations, both in free-air. Following this, the classical corrections are introduced and their accuracy is evaluated. Subsequently, the thin-plate spline interpolation applied to the Flying V polars is discussed, including how these are used to build surrogate models for the wall and strut, and Reynolds number corrections, respectively. Finally, the interpolation is validated with additional scaled Flying V runs.

A. Mesh Description

The meshing process incorporates the insights from Section III. Similarly to the F19, the CAD model of the scaled Flying V used for simulations features a truncated trailing edge. It measures 0.2 mm or approximately 0.059% of the mean aerodynamic chord. The trailing edge of the scaled aircraft is meshed such that there are always four elements along its width. A local sizing is added to the aircraft, such that the maximum curvature

allowed is 5°, with a maximum size of 1.5 mm and a minimum size of 0.05 mm. A body of influence (BOI) with a local cell size of 15 mm encases the aircraft to enhance the prediction of off-body phenomena such as flow separation or vortices. The cell size at the walls, inlet and outlet of the LTT is fixed at 1 000 times the smallest cell size, i.e., 50 mm. Another local sizing condition is applied to the struts such that the maximum curvature is 5° and the smallest and largest sizes allowed are 0.1 mm and 1.5 mm, respectively. The surface mesh of the scaled Flying V is shown in Fig. 12a - the grid for the full-scale aircraft is identical but refined by a factor of 2.5. The struts and aircraft are modelled as no-slip walls. Therefore, 30 inflation layers are added with a first-layer height of 70 μm for the scaled scenarios, and 100 μm for the full-scale scenario. Due to the larger domain of the free-air simulations, these feature a cell size at the domain walls of 10^4 times the smallest element, i.e., 5 m and 150 m for the scaled and full-scale scenarios, respectively. The volume mesh is then populated with poly-hex cells for all scenarios, producing a scaled mesh with 35.3×10^6 cells, wind tunnel meshes with 54.5×10^6 cells on average, and a full-scale mesh with 144×10^6 cells. For a visual inspection of the meshes, refer to Appendix B. Each configuration in the wind tunnel required a separate mesh meaning that, in total, 18 meshes were used. All 18 meshes used feature an average inverse orthogonality greater than 0.8 and a minimum value no smaller than 0.05.

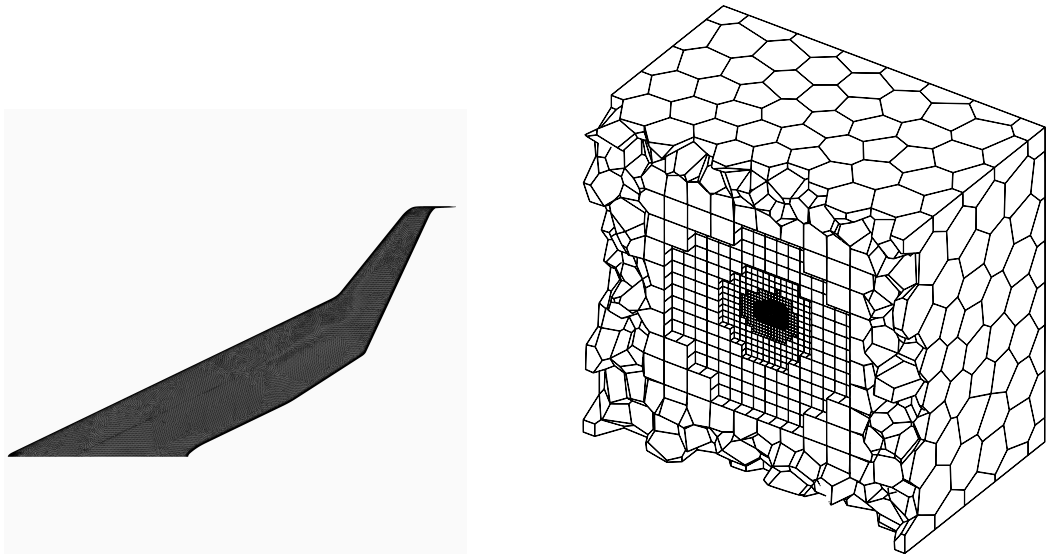

(a) Surface mesh **(b) Cut volume mesh**

Figure 12. Scaled Flying V mesh showcase

B. Simulation Convergence

The forces at each iteration are shown in Fig. 96. The total forces are included in Figs. 96a to 96c, with their normalised counterparts in Figs. 96d to 96f. The normalisation is done with respect to the final, or *converged* value. As a result of vortex shedding on the circular struts, oscillations are present in the normalised solution of the wind tunnel simulations. Their amplitude is never concerning, reaching a maximum of 6% of the converged value at an angle of attack of 0°, where the absolute value is small, and around 0.1% of the solution for the remaining simulations. Across all simulations, the amplitudes are too small to be considered relevant and therefore are not shown in the data.

The effect of changing the order of the discretisation scheme is very apparent. This change can be seen when the solution jumps violently within the first 2 000 iterations. Upon inspection of the last 100 iterations using the first- and second-order discretisation, it is clear that the solution stabilises at significantly different values - the difference at times is in the order of 20%. Not only is there a large delta in the forces between the discretisation schemes, but the first-order schemes often do not appear to predict any vortex shedding, which is a major phenomenon of the flow field. This dual-scheme method successfully accelerates convergence without compromising accuracy.

With the above information, it can be concluded with a high degree of confidence that the simulations are indeed converged. The residuals - see Fig. 95 - and solution variables are all stable during at least the last 100 iterations, with any changes remaining below 0.1% of the converged value and the flow field exhibiting no non-physical artefacts.

C. Simulation Performance

All simulations were run on AMD EPYC™ 7643 processors featuring 48 cores and DDR4 memory, which was allocated proportionally to the total number of nodes used. For each scenario, Table 3 shows the total CPU hours taken for each full test matrix, as well as the average time taken per iteration and per run in seconds. Naturally, the full-scale simulations are the most expensive due to the large grid size, followed by the wind tunnel and scaled scenarios.

Table 3. Simulation performance for Flying V runs

Scenario	CPU hours	Seconds/iteration	Seconds/run	Nodes
Scaled	4 860	2.98	5 690	192
Wind tunnel	18 600	2.17	8 700	480
Full-scale	36 000	5.48	14 100	576

D. Wall and Strut Effects

The walls and struts act to confine the flow, artificially increasing the airspeed the test article encounters relative to the free-air condition. This in effect means the model appears to produce more lift and drag than expected as evidenced by the corrections in Fig. 13: both the lift and drag corrections at low to moderate angles of attack are negative. At high angles of attack, the leading edge vortices dominate the flow field. The walls confine their vorticity and increase their suction. As these flow downstream and their pressure normalises back to the freestream pressure, they encounter a higher adverse pressure gradient than the free-air scenario. Under the current conditions, this higher adverse pressure gradient causes the vortices to break down. Since these vortices tend to stabilise the flow over the leeside of the wing, their absence causes most of the outboard wing to stall, advancing the onset of separation and stall to a lower angle of attack. From Fig. 13, it can be seen that the highest angles of attack generally do not follow the same trend as the rest of the data points. Furthermore, this change to the vortex system has a vast impact on the moments felt by the model. Since the vortices have a strong stabilising effect on the pressure over the leeside, any disturbance to them will change the pressure distribution over the aircraft. Small changes in the distribution may not affect the forces greatly, but they may shift the location of the resultant aerodynamic force, thus greatly affecting the moments experienced by the aircraft. This is clearly visible in Fig. 13e, where the difference in pitching moment between the confined and free-air simulations is highly irregular, with no clear pattern emerging presumably due to unstable vortices.

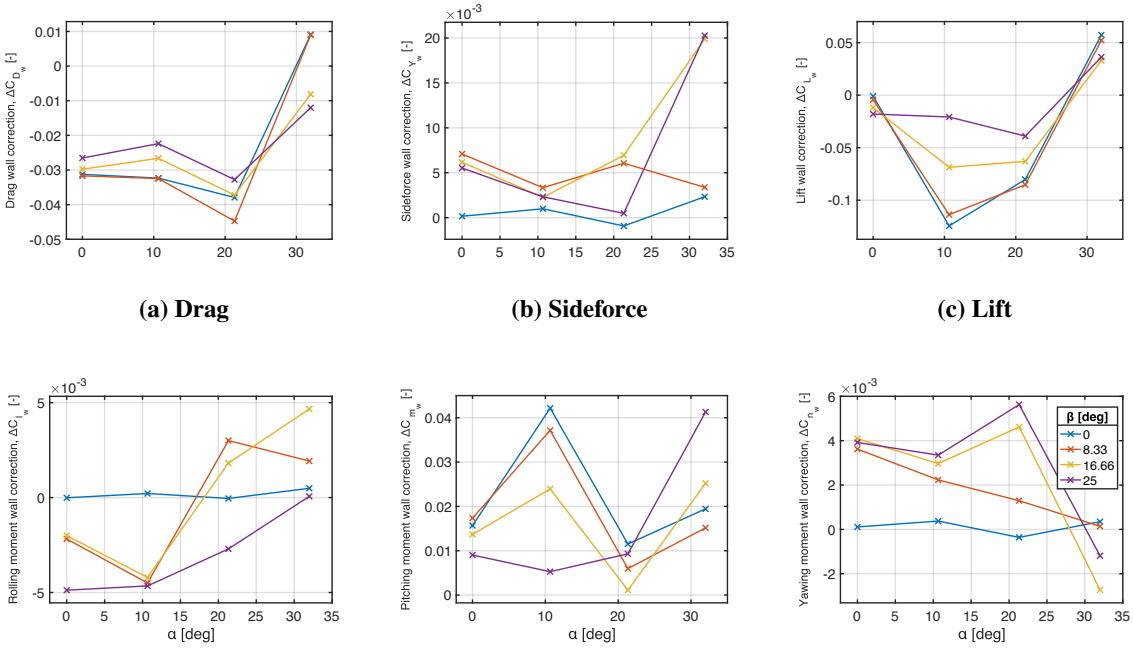

(a) Drag **(b) Sideforce** **(c) Lift**

(d) Rolling moment **(e) Pitching moment** **(f) Yawing moment**

Figure 13. Corrections for wall and strut effects

Consider the leading edge vortices over the Flying V in symmetric conditions. In free-air, these travel downstream over the aircraft, creating a 'streak' of low pressure on the upper surface, e.g. in Fig. 46. In the wind tunnel, the presence of the walls decreases the pressure at their cores and promotes premature breakdown, thereby generating higher pressures near the aft of the aircraft. One may not expect this new distribution to yield a substantially different magnitude of the resultant force, but its location would very likely shift. This is the underlying mechanism that is dominating the moments, despite relatively small changes to the forces.

The angle of sideslip has a profound impact on the performance of the Flying V. It appears as though sideslip inversely affects the strength and coherence of the left and right leading edge vortices. With the flow reaching the wing from the right, the right wing effectively features less sweep, with the opposite being true for the left wing. This, in turn, reduces the strength of the right vortex. Without this stabilising factor, the flow over this section of the wing is more susceptible to stall, as evidenced by the pressure loss contours in Appendix G. The right wing at times is completely stalled, while the left wing features mostly attached flow. Under high angles of sideslip, the left vortex appears stronger and to flow further downstream often showing few signs of breakdown. The data shows a small separation region just aft of the left leading edge which is subsequently controlled by the left vortex. This is true across all three conditions, which contributes to a significant reduction in drag coefficient at high angles of attack. Due to the severe stall on the right wing across all conditions, the lift generation at high angles of sideslip is moderately hampered. For the full-scale aircraft, the stall is concentrated towards the outboard wing only. Due to the higher Reynolds number, this is also the only condition which does not show signs of stall in the sideforce polars. Due to the asymmetric stall, the moments are all greatly affected by the angle of sideslip, although to different degrees between the three conditions. While the scaled and full-scale predictions suggest that the pitching and yawing moments are still increasing beyond an angle of attack of 32°, the wind tunnel moment predictions appear to reach a maximum at 21.33°. The exact mechanism behind this discrepancy is unclear.

E. Reynolds Number Effects

At the full-scale Reynolds number, there is a large discrepancy in the data sets at high angles of attack and sideslip. The mechanism behind the discrepancy is relatively simple, but its effect is profound. The full-scale aircraft features a proportionally thinner boundary layer, with an increased level of turbulence and higher resistance to adverse pressure gradients. As evidenced by the pressure loss contours such as Fig. 62, the onset of separation is significantly delayed in the full-scale aircraft. This is clearly visible in Fig. 14, where the corrections suggest that the aircraft should, in fact, reach substantially higher maximum forces and moments at a lower drag penalty.

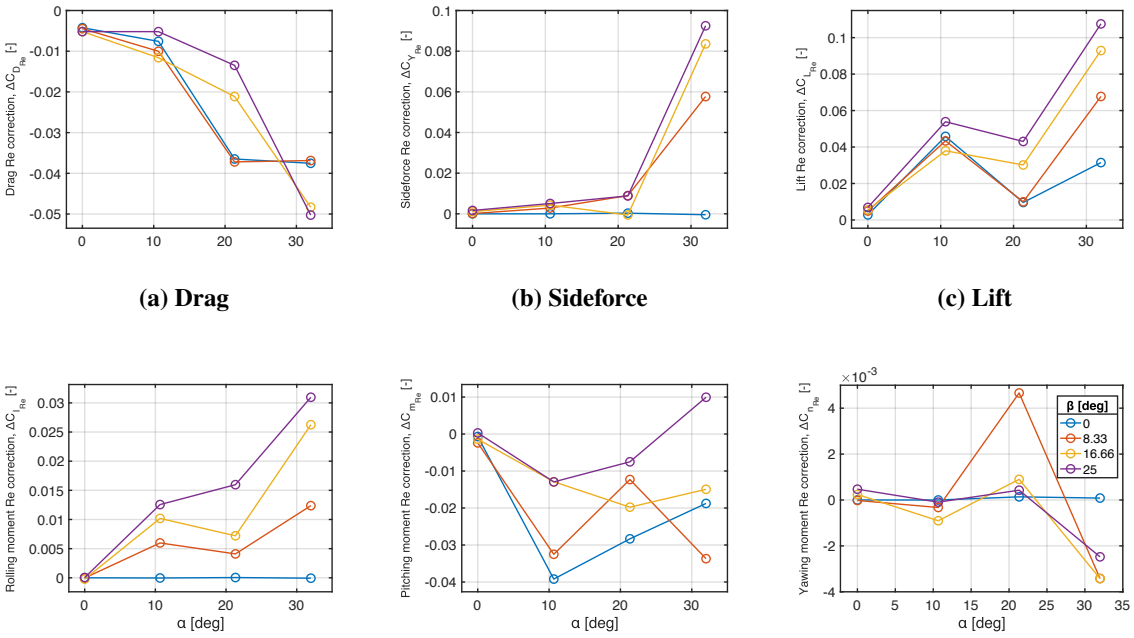

(a) Drag **(b) Sideforce** **(c) Lift**

(d) Rolling moment **(e) Pitching moment** **(f) Yawing moment**

Figure 14. Corrections for Reynolds number effects

A consequence of the higher turbulence levels within the boundary layer is higher pressure loss under attached conditions. Take for instance Fig. 62: there is a visible wake over most of the wing in both of the sub-scale scenarios, while this is only true for the outboard wing of the full-scale aircraft. The pressure loss over the leading edge of the full-scale aircraft is also noticeably higher. The same logic applies to the vertical tail, hence the delayed stall in sideforce in Fig. 37. This is also confirmed by the pressure coefficient contours and the surface streamlines in Fig. 45. The full-scale aircraft maintains a strong pressure peak along its right leading edge, while in both sub-scale models, the pressure is close to ambient - an indication of stall. The conclusion that can be drawn from the data is unsurprising - the full-scale aircraft is more resistant to stall.

F. Comparison with Classical Corrections

The classical corrections shown in Fig. 15 do not reflect the findings of the numerical results from Fig. 13 to an acceptable level of accuracy. Foremost, the classical corrections are not able to account for the non-linearities arising at extreme attitudes. Since the corrections are a function of the lift generated by the confined aircraft, among other variables, they assume that the same phenomena are taking place in the wind tunnel as in free-air. As a result, both the general shape of the correction curves and the magnitudes are remarkably

incorrect. The results are only comparable in trivial scenarios, such as the rolling moment, yawing moment and sideforce coefficients at symmetric conditions. It can therefore be deduced that the classical corrections cannot accurately account for the complex flow phenomena over the Flying V to a sufficient degree of accuracy, likely because the underlying assumptions are not valid.

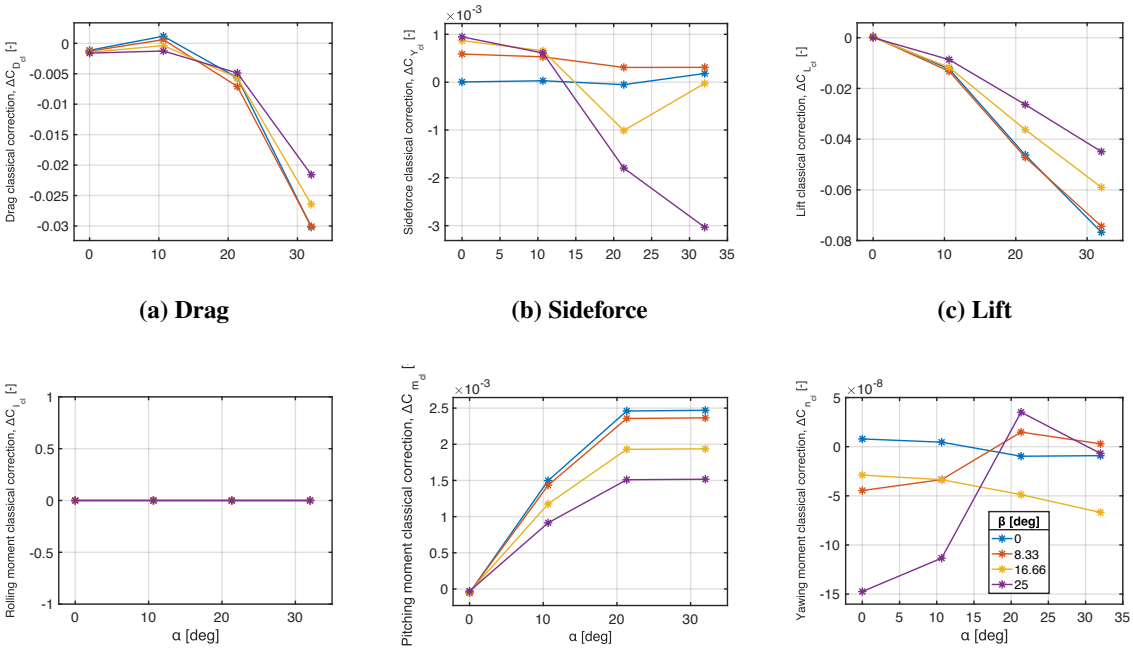

(a) Drag **(b) Sideforce** **(c) Lift**

(d) Rolling moment **(e) Pitching moment** **(f) Yawing moment**

Figure 15. Classical corrections

G. Data Interpolation

As discussed in Section II, thin-plate spline interpolation is applied to the results in order to overcome the relative sparsity of the test matrix. This method is applied to the forces and moments rather than to the correction factors because the latter is highly scattered, meaning that any interpolation attempts would likely return invalid results. Across the three scenarios, for each of the six force and moment coefficient polars, all 19 interpolation coefficients, **a**, are documented in Appendix D, for parties interested in reproducing the results retroactively. An example of the interpolation is shown for the sub-scale drag coefficient in Fig. 16.

Take, as an example, the free-air, sub-scale and wind tunnel drag coefficients. Subtracting the latter from the former yields the correction factors in terms of α and β for the effect of the walls and struts. Applying the same logic to the full- and sub-scale coefficients would yield a correction contribution for the influence of the Reynolds number.

$$C_{D_{free\text{-}air,\,full\text{-}scale}} = \underbrace{C_{D_{wind\ tunnel}} + \Delta C_{D_{walls}}}_{C_{D_{free\text{-}air,sub\text{-}scale}}} + \Delta C_{D_{Re}} \tag{10}$$

By using the splines for the coefficients, this approach effectively provides a surrogate model for the wind tunnel corrections for any combination of β and α, requiring only three inputs: the angle of attack, the angle

of sideslip and the measured coefficient of interest. Both correction contributions - for the effect of the walls and struts and for the effect of the Reynolds number - can be accounted for independently. The interpolation centres, **c**, are the same as for the coefficient interpolations, while the interpolation coefficients, **a**, are shown in Appendix E.

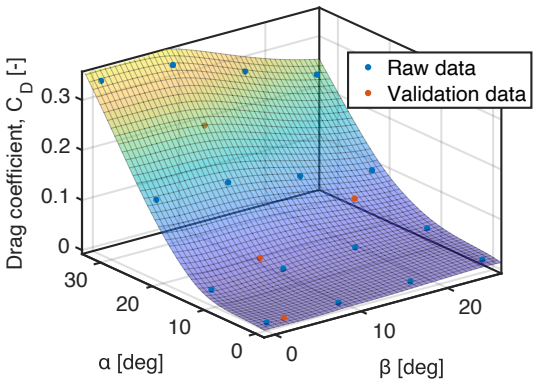

Figure 16. Thin-plate spline surface for sub-scale drag coefficient including validation points

To evaluate the accuracy of the interpolation, four additional runs are carried out on the scaled aircraft. The four attitudes are randomly distributed while avoiding proximity to existing data points. The validation attitudes are shown in Table 4a. The thin-plate splines for the scaled conditions are evaluated at these attitudes and are compared to the RANS simulations. The RMSE across all four simulations is documented in Table 4b for each coefficient. The interpolation errors can also be visualised in Appendix I.

While the interpolation shows excellent agreement at low angles of attack and sideslip, the non-linearities at high angles become hard to predict with such coarse data and consequently, the accuracy of the data fitting suffers. The surfaces for the full-scale aircraft, for instance, feature a much simpler topology with less curvature, since there are no signs of stall. This makes them much better candidates for interpolation. Generally speaking, the interpolation yielded the best results for the drag, lift and yawing moment. Their splines may be used with a high degree of confidence across the entire test matrix. Since the remaining coefficients are much more sensitive to stall, their interpolation should be considered with caution, particularly close to extreme attitudes.

Table 4. Summary of interpolation validation

(a) Attitude combinations for validation

Run	Angle of sideslip	Angle of attack
1	9°	27°
2	2°	0°
3	21°	18°
4	7°	13°

(b) Interpolation error

Coefficient	RMSE
Drag	0.00549
Sideforce	0.00400
Lift	0.00897
Rolling moment	9.22×10^{-4}
Pitching moment	0.00862
Yawing moment	4.37×10^{-4}

V. Conclusion

The current work presents high-fidelity corrections for wind tunnel effects over the Flying V through the use of state-of-the-art RANS codes. The analyses elucidate the complex vortical flow structures around the aircraft at high angles of attack and provide insights into their sensitivities to the presence of the walls and struts, as well as Reynolds number. Namely, the presence of the walls confines the vorticity at the vortex cores, creating stronger suction and a consequently more abrupt adverse pressure gradient near the aft of the aircraft. This, in turn, is reflected in the force polars to a moderate degree: the onset of stall is advanced under confined conditions. The moments are significantly and chaotically affected, with the corrections featuring large magnitudes with no clear trend. The increase in Reynolds number has the opposite effect: it stabilises the boundary layer over the aircraft, making it more resilient to stall. The flow remains attached over most of the aircraft across the entire attitude range in full-scale conditions, with the vortices being more concentrated. Presumably due to higher levels of turbulence in the boundary layer, higher pressure loss is also observed over the surface. Lastly, the angle of sideslip acts to increase the severity of stall, when present, on the right wing (for positive angles), while greatly stabilising the flow on the left wing. The left vortex becomes smaller in diameter but extends further downstream to cover more of the wing. As a result, even at extreme attitudes the flow over the left wing has a strong tendency to remain attached, leading to decreased drag and lift at high angles of attack relative to the low sideslip conditions. The moments show a high sensitivity to the sideslip due to the significant changes to the pressure distribution. The free-air predictions suggest that the moments have not reached a maximum value at 32° of angle of attack, unlike the confined simulations. The classical corrections cannot, to any capacity, predict any of the complex interactions described above. These corrections did not match either the sign or the order of magnitude of the CFD corrections across most of the test matrix, thereby motivating such an involved procedure for the prediction of corrections for wind tunnel effects. As an alternative to the classical method, a thin-plate spline-based surrogate model of the corrections is presented which returns corrections within the equispaced points provided by the simulations.

The main limitations of the current work are primarily concerned with hardware and software constraints. Foremost, the software suite available strongly restricted the maximum aspect ratio at the walls, thereby constraining the dimensionless wall distance. This parameter has been proven to have a significant impact on the prediction of separated flows. While the validation suggests that this effect is minimal, it is strongly recommended that future RANS analyses of the Flying V revise the meshing procedure. On a hardware-related note, the accuracy of the results would have benefited from both finer discretisation and more accurate physics modelling. More specifically, DES and dynamic mesh refinement appear as strong candidates to improve the fidelity of the data. The former uses a different approach towards solving turbulence which should capture more subtleties in the flow field, and its unsteady approach should more accurately predict vortex breakdown and its effect on the rest of the flow. The latter ensures that the mesh is refined and coarsened locally, based on solution gradients such that the resources can be allocated more efficiently, making the most out of the available hardware. In both cases, more hardware power is required, and dynamic mesh refinement was not available at the time of writing. Finally, the thin-plate spline interpolation showed good agreement with the validation data, however, the highly non-linear nature of the flow over the Flying V at high angles calls for more data points to be collected. No interpolation method is suggested to improve the quality of the interpolation.

This article puts forth convincing evidence that RANS not only gives a better understanding of a test article's aerodynamic performance, both in confined and free-air conditions, but also gives higher confidence in the understanding of wall, strut and Reynolds number effects at a significant, yet reasonable computational cost. Such an approach is strongly recommended for similar investigations provided that similar or more powerful hardware is available.

References

[1] Benad, J., and Vos, R., "Design of a Flying V Subsonic Transport," *33rd Congress of the International Council of the Aeronautical Sciences*, 2022.

[2] Siemonsma, K., "Aerodynamic model identification of the Flying-V using flight data," , 2022. Unpublished TU Delft MSc thesis.

[3] Laar, Y., "Aerodynamic Design of a Flying V Aircraft in Transonic Conditions," , 2023. Unpublished TU Delft MSc thesis.

[4] Timmer, W., "Two-dimensional low-Reynolds number wind tunnel results for airfoil NACA 0018," *Wind Engineering*, 2008.

[5] Goetten, F., Finger, D. F., Marino, M., Bil, C., Havermann, M., and Braun, C., "A review of guidelines and best practices for subsonic aerodynamic simulations using RANS CFD," *Asia-Pacific International Symposium on Aerospace Technology-APSIAT 2019*, 2019.

[6] van Arnhem, N., de Vries, R., Vos, R., and Veldhuis, L. L., "Aerodynamic performance of an aircraft equipped with Horizontal Tail mounted propellers," *AIAA Aviation 2019 Forum*, 2019, p. 3036.

[7] Stokkermans, T. C., Van Arnhem, N., Sinnige, T., and Veldhuis, L. L., "Validation and comparison of RANS propeller modelling methods for tip-mounted applications," *AIAA journal*, 2019.

[8] Dacles-Mariani, J., Zilliac, G. G., Chow, J. S., and Bradshaw, P., "Numerical/experimental study of a wingtip vortex in the near field," *AIAA journal*, 1995.

[9] Barlow, J. B., Rae, W. H., and Pope, A., *Low-speed wind tunnel testing*, John Wiley & sons, 1999, Chap. 10.

[10] Mozaffari, S., Guilmineau, E., Visonneau, M., and Wackers, J., "Average-based mesh adaptation for hybrid RANS/LES simulation of complex flows," *Computers & Fluids*, 2022.

[11] Frink, N. T., Tormalm, M., and Schmidt, S., "Unstructured CFD Aerodynamic Analysis of a Generic UCAV Configuration," *NATO RTO AVT-189 Specialist Meeting*, 2011, p. 38.

[12] Konishi, K., Kojima, Y., Hashimoto, A., and Kameda, M., "Prediction Accuracy of RANS-based Analysis for Aerodynamic Forces and Moments of a Civil Aircraft Model," *AIAA SCITECH 2023 Forum*, 2023, p. 1758.

[13] Loeser, T., Vicroy, D., and Schuette, A., "SACCON static wind tunnel tests at DNW-NWB and 14 x22 NASA LaRC," *28th AIAA applied aerodynamics conference*, 2010, p. 4393.

[14] Schütte, A., Hummel, D., and Hitzel, S. M., "Flow physics analyses of a generic unmanned combat aerial vehicle configuration," *Journal of Aircraft*, 2012.

Part II

Literature study

*This part has been assessed for the course AE4020 Literature Study.

1

Introduction

Climate change is an ever-increasing threat to our planet, and its impact on the environment and human life has become a pressing issue. The Intergovernmental Panel on Climate Change (IPCC) predicts that if immediate and decisive action is not taken to curb greenhouse gas emissions, the consequences could be catastrophic[1]. One of the major contributors to this problem is the aerospace industry, which is responsible for a significant amount of global carbon emissions. Despite only around 5% of the global population flying[2], aviation accounts for around 3.5% of global climate effects[3]. Efforts to reduce emissions from aircraft have largely focused on incremental improvements in engine and aerodynamic efficiency. However, these small gains are not enough to solve the problem, and a more radical approach is needed. Novel aircraft designs have the potential to make a significant impact, and one such design is TU Delft's Flying V.

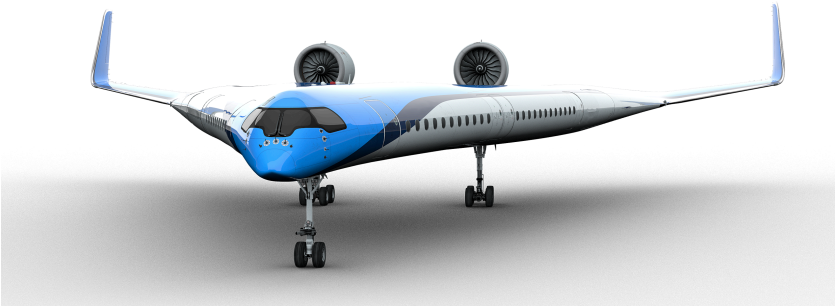

Figure 1.1: Conceptual design of the Flying V [51]

Due to its innovative design, this novel flying wing concept, which integrates the passenger cabin, cargo hold, and fuel tanks into its V-shaped wings, promises up to a 20% fuel burn reduction when compared to a modern twin-aisle aircraft with the same top-level aircraft requirements, the same technology assumptions, and the same propulsion system [10].

As advancements are made on the Flying V's design, researchers are preparing to build a scale model for aerodynamic testing at TU Delft's Low Turbulence Wind Tunnel (LTT). The testing is projected to start around January 2024. One crucial element of wind tunnel testing is the concept of *wall corrections*. The physical conditions that a test article experiences during testing are altered by the presence of wind tunnel test section boundaries. Therefore, whenever data from one tunnel is compared to another or is compared to a free-air condition, wall interference corrections must be applied to the test results [50].

[1] https://on.nrdc.org/3ZVYCkp, accessed on 10 March 2023
[2] https://bit.ly/3HwctHS, accessed on 23 January 2023
[3] https://bit.ly/3ZZZy89, accessed on 23 January 2023

As of the time of writing, LTT-derived data typically makes use of classical corrections, while forgoing numerical corrections with potential flow codes. In an effort to advance the fidelity of the classical corrections employed, the use computational fluid dynamics (CFD) is proposed. This way, analytical and numerically linear corrections can be replaced with high-fidelity CFD corrections which can be applied to non-linear flow regimes, such as separated, highly vortical or high-Mach number flows. Such work was employed at the Onera lab in France where researchers concluded that advanced numerical corrections are comparable to the present approach in the linear aerodynamic domain albeit incurring a higher CPU cost. The report claims that the true advantage of high-fidelity CFD is visible in non-linear regimes [25] which accounts for much of the Flying V's flight envelope. The suggested work will aim to find subsonic corrections for the aerodynamic performance as well as stability properties of the Flying V, by comparing free-flight and wind tunnel CFD simulations. Furthermore, scaled simulations will be compared with their full scale counterparts to quantify the Reynolds number effects. A simplified view of this process is illustrated in Figure 1.2. Response surfaces will be built for each variable of interest in an attempt to make the data more suitable for future experimental investigations, while also saving computational resources.

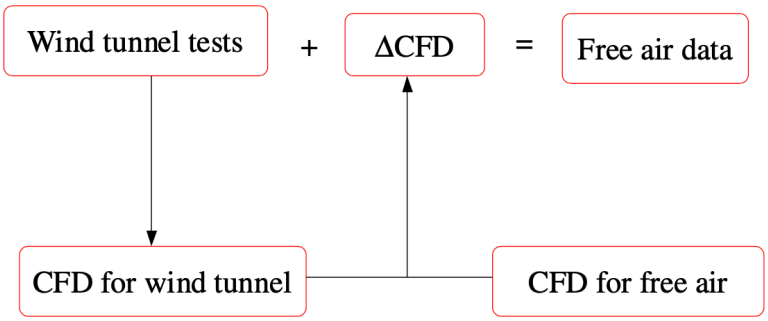

Figure 1.2: Overview of CFD corrections of wind tunnel data [42]

Formally, the overarching research question of the proposed work can be phrased as follows:

> *"To what extent will wind tunnel wall interference and Reynolds number effects influence future performance measurements of the Flying V in the Low Turbulence Wind Tunnel?"*

The aim is to find the influence of the wind tunnel and Reynolds number effects by numerically modelling the Flying V in the wind tunnel and in free-air to determine the difference in performance. These deltas can be used to check the currently existing corrections and determine their accuracy in non-linear flow regimes. The goal of this research is formally expressed as follows:

> *"To understand and quantify the influence of wind tunnel testing and Reynolds number effects on the Flying V's performance using a CFD approach."*

This report is intended as a prelude for the proposed work which requires comprehensive knowledge of experimental simulations ranging from the concept of Modern Design of Experiments (MDOE) and wind tunnel corrections, to high-fidelity CFD solvers and techniques. In addition, a deep insight of the flow around highly swept wings is required in order to assess the limitations of the proposed work. All of the above will be covered extensively in this report, starting with an introduction to the current and future development on the Flying V in chapter 2, followed by TU Delft's facility of choice for the experimental campaign on the Flying V - the LTT - in chapter 3. Next, wall interference corrections for wind tunnel testing are comprehensively discussed in chapter 4, with an introduction to Reynolds number effects being presented shortly after in chapter 5. Subsequently, relevant CFD codes are briefly described in chapter 6, alongside limitations and best practices. To conclude, the approach towards designing the numerical experiment is detailed in chapter 7. Naturally, the findings of the report are summarised in a conclusion in chapter 8.

2

The Flying V

In this chapter, the Flying V is introduced alongside its current development; future steps are also proposed and the detailed working geometry of the Flying V is given.

2.1. Development

The Flying V is an innovative aircraft concept that has been developed by a team of researchers at the Delft University of Technology in the Netherlands. Unlike traditional aircraft designs, which have a fuselage and separate wings, this flying wing design integrates the wing and fuselage into a single, wing-shaped structure. The design also incorporates a crescent wing shape, which can be seen in Figure 2.1, for enhanced stability properties.

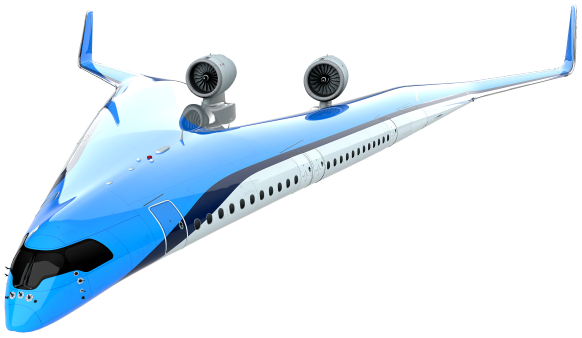

Figure 2.1: Artistic rendition of the Flying V

Over the past ten years, extensive research has been conducted on the Flying V configuration, indicating that it is a practical and energy-efficient alternative to traditional tube-and-wing aircraft. The research has focused on various aspects of the Flying V design, including aerodynamics, structural design, weight, handling qualities, and interior design. Despite some challenges in each of these areas, none of them have been deemed as major impediments to the viability of the concept.

Currently, there are several ongoing research projects on the Flying V in various fields such as aerodynamics, structures and manufacturing, flight dynamics and control, aeroelasticity, environmental impact, and airport operation. These projects include investigations of optimisation of the outer-mold line for better aerodynamic efficiency, analysis of spoilers, preliminary design of engine and landing gear integration, bird strike investigation for the leading-edge windows, cockpit design and flight deck integration, testing of take-off and landing handling qualities in the simulator, assessment of the noise signature, flight performance investigation, and simulation of ground handling processes.

The Flying V concept has the potential to revolutionise the aviation industry, offering a promising solution to the pressing problem of climate change. By reducing fuel consumption and emissions, this innovative design could help to mitigate the impact of aviation on the environment, while also providing a more comfortable and efficient passenger experience [10].

2.2. Previous studies

This section briefly covers relevant studies previously conducted on the Flying V. These include various experimental campaigns conducted on a 4.6% scale half-model and a high-fidelity numerical analysis.

2.2.1. Aerodynamic performance of half-model

A previous experimental campaign investigated the aerodynamic performance of a half-span wind tunnel model of the Flying V [41]. The paper in question outlines an experimental investigation into the aerodynamic characteristics of a 4.6% scale half-model of a flying-wing transport aircraft. The study was conducted in an open-jet wind tunnel, with forces and moments being measured using a 6-axis balance. Specifically, two control surfaces located in the outboard wing were deflected to determine their impact on lift, drag, and pitching moment up to a Reynolds number of 1.0×10^6. Subsequently, the outcomes were combined with an estimated thrust force obtained from a flight mechanics model of the aircraft to predict the most forward and aft centre-of-gravity positions for which the aircraft could be balanced with the control surfaces, while still maintaining static stability.

It was found that the aircraft could achieve an untrimmed maximum lift coefficient of 1.02 at an angle of attack of 35 degrees. Additionally, the pitching moment around the leading edge of the mean geometric chord was found to be negatively correlated with the angle of attack up to 19 degrees. Beyond this, a strong pitch-break occurred, rendering the aircraft statically unstable. This was associated with a forward shift of the aerodynamic centre to a longitudinal position 35% of the mean aerodynamic chord (%$\bar{c}$) ahead of the moment reference point, which was caused by the formation of strong vortices over the wing surface. The study demonstrated that the effectiveness of the control surfaces did not significantly deteriorate with angle of attack, and all three control surfaces remained effective up to the maximum lift coefficient. Analysis showed that in power-off conditions, the centre-of-gravity location should be between -7.5%$\bar{c}$ and 0.5%$\bar{c}$, and in power-on conditions, it should be between -6%$\bar{c}$ and 1%$\bar{c}$, both measured from the leading edge of the mean geometric chord. These ranges ensured an ultimate static stability margin of 4.4%, as well as a minimum landing speed of 20 m/s. Within these parameters, trimmed maximum lift coefficient values of 0.68 and 0.66 could be achieved in power-off and power-on conditions, respectively.

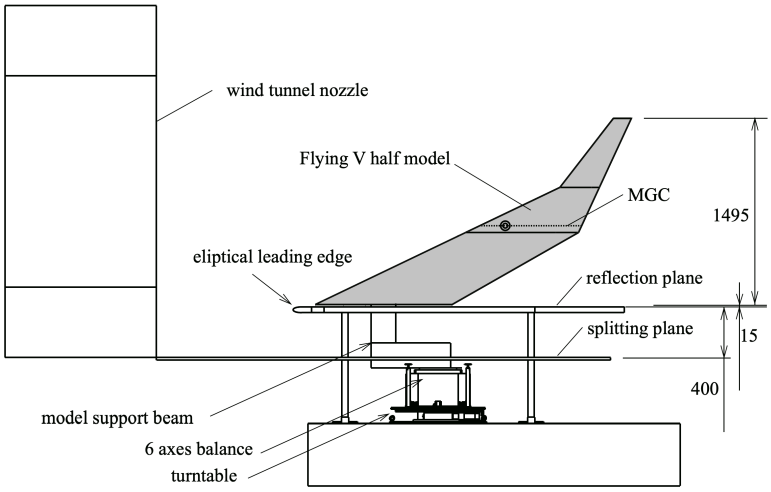

Figure 2.2: Experimental setup of half model. Dimensions are in millimetres [41]

The proposed investigation will forgo the effect of control surfaces for simplicity. Numerically simulating

the complex flow over and through control surfaces can be very demanding, with most turbulence codes failing to predict the relevant phenomena to a sufficient level of accuracy. Wake bursting, interference effects and pressure gradients over the boundary layer combined make this type of flow very dependent on the mesh quality and turbulence model settings, yielding a low level of confidence without validation. Furthermore, the proposed investigation is focused on a full model of the Flying V, as this is the planned geometry for the experimental campaign in 2024. This will allow for sideslip, meaning that stability coefficients and derivatives will be measured in the wind tunnel. This also eliminates the horseshoe vortex that forms at the junction between the aircraft and the wall which should yield more representative results [34].

2.2.2. Large eddy simulations

On the same geometry, a different investigation aimed to find the aerodynamic performance, and stability coefficients of the Flying V using Large Eddy Simulations (LES) [16]. The simulations were commissioned by the Aerospace Faculty at TU Delft. The calculations were done for a number of different configurations and an airspeed of 20 m/s. Sweeps were performed for angle of attack ($0^\circ \leq \alpha \leq 30^\circ$) and elevon deflection ($0^\circ \leq \delta_e \leq -20^\circ$) separately. One simulation investigated to the performance at an angle of sideslip of 20 degrees and finally, results were also compared between simulations at a Reynolds number of 1.0×10^6 and 7.0×10^7, *ceteris paribus*. The results of this investigation reveal the clear development of leading edge vortices, and owing to their high-fidelity, can serve as a means of verifying the proposed RANS simulations, especially since the relations of lift, drag and moment against angle of attack are all given explicitly. In addition, the Flying V shows only mild signs of stall at an angle of attack of 30°.

2.2.3. Winglet and rudder performance of half-model

In this experimental campaign, a scaled Flying V model was tested in a wind tunnel to investigate the effect of tip-mounted winglets/rudders. The research aimed to determine the aerodynamic effects of installing the winglet/rudder combination and deflecting the rudder. They also quantified the change in rudder effectiveness for various aileron deflections and airspeeds [29].

The wind tunnel model was the left half of the Flying V and was mounted vertically in the Open Jet Facility (OJF) wind tunnel at TU Delft. A reflection plane with an elliptical leading edge was placed at the root of the half-model to split the flow and act as a symmetry plane. The researchers corrected the data obtained and found that the sample standard deviations of all aerodynamic coefficients were below 0.004 for the dual-wing results and below 0.0029 for the half-wing results.

The winglet integration was been found to slightly increase the lift coefficient by a maximum of about 0.0035 for angles of attack below 10° but slightly decrease the lift coefficient by a maximum of about 0.016 for higher angles. The winglet has also been found to increase the drag of the model by a maximum of about 0.004 until around 28° angle of attack. Furthermore, the winglet has reduced the maximum untrimmed lift-to-drag ratio from around 14.4 to 12.3 at 10° angle of attack. Rudder deflections have been found to reduce the lift coefficient at all angles of attack, with only a few conditions where deflecting the rudder marginally increases the lift. Rudder deflections have also been found to increase the drag coefficient at all positive angles of attack. Positive and negative rudder deflections oppositely affect the side force of the left wing until higher angles of attack. Beyond about 25° angle of attack, the smaller three of the four negative rudder deflections have the opposite effect on the half-wing side force coefficient than desired. Positive and negative rudder deflections oppositely affect the rolling moment of the left wing until higher angles of attack. Negative rudder deflections provide larger increases in pitching moment than positive ones. With the wing control surfaces at null deflection, the side force, yawing moment, and rolling moment rudder control derivatives have been extracted from the data and linearised. Increases to the angle of attack significantly reduce the slopes of these control derivatives in a non-linear fashion.

2.2.4. Effect of engine integration on half-model

This study presents the findings of subsonic wind tunnel tests conducted at the OJF on a 4.6%-scale half model of the Flying V [51]. The tests investigate the installation and interference effects of an engine and nacelle, with balance measurements taken to record lift, drag, and pitching moment at a

velocity of 20 m/s. Results demonstrate significant interference effects between the wing and engine, with interference drag observed over the entire range of angles of attack above 5°. The interference effect during engine operation reduces the drag by approximately 20 counts at incidence angles lower than 5°. The interference effects of thrust and nacelle on lift and pitching moment are similar to the effect of superimposing the contributions of the isolated engine and the wing, indicating they cannot be neglected. However, further research is required to study the interaction effects on the local pressure distribution, which could not be determined from the measurements presented in this study.

2.2.5. Main takeaways

All of the previous experimental campaigns were conducted on a half-model, meaning that information on lateral stability is non-existent. Further, it is well understood that half-models suffer large alterations to their flow relative to full span models as a result of the the strong influence of the tunnel wall boundary layer on the flow [38]. In order to further refine the aerodynamic design of the Flying V, full model testing is a necessity. The proposed investigation will play an important role in the data processing of the full model Flying V experimental campaign in 2024, by estimating the wall interference and Reynolds number effects in a quantitative, numerical approach, which has not been possible with the aforementioned investigations. Furthermore, it will make use of the most recent iteration of the Flying V's design, on which there are few investigations.

2.3. Current geometry

As of the time of writing, a refined geometry of the Flying V has been released internally, aggregating much of the recent research and development into a centralised source. This most up-to-date geometry is expected to be used in the experimental campaign in 2024. Previous experimental studies in the Low Turbulence Tunnel have used scaled models with a total wing span of around 1 400 mm [54, 5] or a span-to-tunnel-width ratio of around 0.78. As a result, this is the expected scale of the wind tunnel model; around 2.2% scale. It has been confirmed that this size fits within the test section even at the most extreme configurations with an angle of attack of 40° and angle of sideslip of 20°.

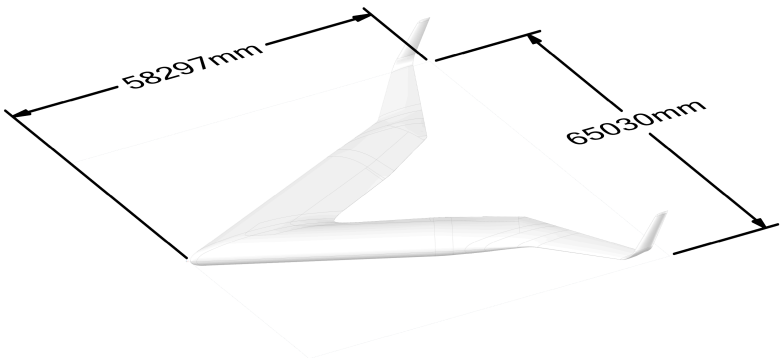

Figure 2.3: Dimensions of current Flying V geometry

This version of the aircraft is 58.3 metres long, 65.0 metres wide, and 8.9 metres tall - the full technical drawing can be found in Figure A.1. Unlike previous versions of the Flying V, such as the experimental model in [41, 51, 29] or more recent digital models such as in [33], this version has no kinks at the root, nor at the transition from the inboard to outboard wing. Additionally, the chord-wise cross-sections are free of kinks. The trailing edge of the model is also truncated such that its height is constant along the span. This is highly preferable in the gird generation step as it enables high quality cells to be formed at the trailing edge, ensuring good convergence and speed later in the solving process.

3

TU Delft's Low Turbulence Tunnel

In this chapter, the Low Turbulence Tunnel (LTT) located at Delft University of Technology is introduced. Its geometry and specifications are detailed and to finalise, its digital counterpart is explored with all major modelling decisions being described.

3.1. Geometry

TU Delft's LTT is a state-of-the-art wind tunnel facility designed and built in the early 2000s to provide researchers with a controlled environment to study the aerodynamics of objects in a wind tunnel with extremely low turbulence levels. The LTT is an atmospheric, closed-throat, single-return type tunnel. The tunnel's dimensions are substantial, as the fan and engine are situated on the ground level, while the settling chamber and the test section are located on the second floor. The six-bladed fan is powered by a 525 kW DC motor, producing a maximum test section velocity of approximately 120 m/s. The maximum Reynolds number for two-dimensional testing is approximately 3.5 million. Due to the tunnel's large contraction ratio of 17.8, the free-stream turbulence level in the test section ranges from just 0.015% at 20 m/s to 0.07% at 75 m/s. The corner vanes, which rotate the flow in the corners of the tunnel, are equipped with a cooling system to regulate the flow's properties. This wind tunnel boasts of ten interchangeable octagonal test sections measuring 1.80 m wide, 1.25 m high, and 2.60 meters long. For a schematic overview of the wind tunnel, refer to Figure 3.1.

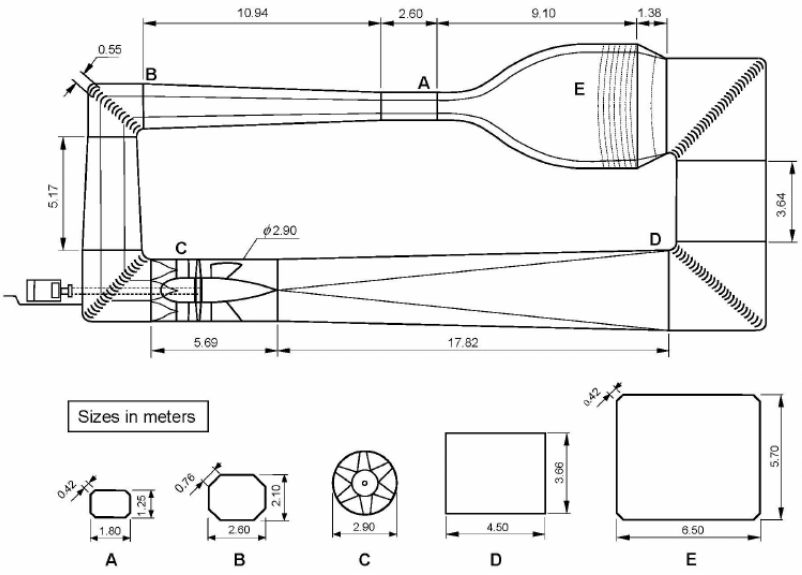

Figure 3.1: Schematic overview of the LTT [49]

The low turbulence levels in the LTT make it an ideal facility for studying the aerodynamics of objects with high precision, such as aircraft wings, or wind turbine blades. The facility has been used for a wide range of research projects, including studies on flow control of separation on wing-flap systems, boundary layer suction, and propeller-wing interaction.

3.2. Numerical approach

The domain shape and size in a RANS simulation can have a dramatic effect on the results as shown by Goetten et al. [23]. For free-air simulations, the shape plays a lesser role than the size of the domain - the body should be placed “significantly further” than ten body lengths from the outlet, while the domain may take a cuboid, spherical or bullet shape. For simulations within a wind tunnel, this choice becomes more complicated, since there are obvious geometrical limitations to the shape of the domain.

It is expected that the Flying V model will have a width of 1.4 metres and a length of around 1.2 metres. Since the test section of the LTT is 2.6 metres long, this places the Flying V model only 0.7 metres from either the inlet or outlet, if only the test section were to be used as the domain. Such a short domain would surely cause problems for the solver and the results would very likely be non-physical. As a result, the domain must be enlarged. Naturally, simulating the entire wind tunnel is not feasible. So the question becomes, how should the wind tunnel be modelled? The alternatives are to either extend the constant cross-section of the test section or to include part of the contraction chamber and diffuser alongside the test section.

To answer this question, consider a similar investigation by the National Aeronautics and Space Administration (NASA) for the American Institute of Aeronautics and Astronautics (AIAA)[1]. Researchers attempted to validate their in-house CFD solver by comparing its numerical results with a full-fledged experimental campaign of a half-span model of a wing in high-lift configuration, equipped with slats and flaps [44]. For the numerical approach, the researchers considered two different wind tunnel geometries: one with part of the bell intake, part of the diffuser and with viscous walls, and another with a constant cross-section and inviscid walls. They found that the results were almost identical between the two configurations, although the viscous model required an adjustment to the diffuser to prevent an unsteady flow region from forming, diverging the solution. The viscous simulations were also significantly more expensive to run. From this, it can be inferred that the boundary layer along the wind tunnel does not have a significant impact on the accuracy of the solution while drastically increasing the computational resources required. With this in mind, it is still unclear what effect the domain shape has on the accuracy of the simulation since the investigation did not detail the exact geometry of the two simulations.

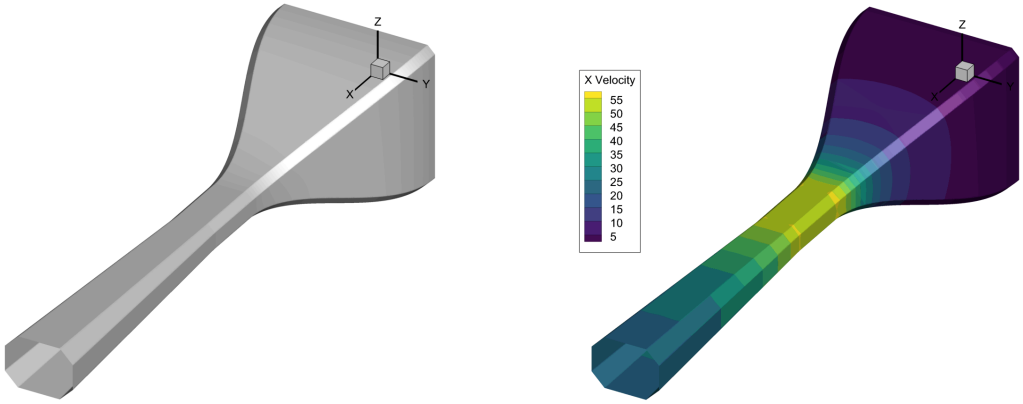

(a) Geometry including contraction tube, test section and diffuser

(b) RANS solution of x velocity over surface in m/s

Figure 3.2: Numerical model of the LTT

Since the presence of the Flying V in the test section will have a great up and downstream influence, it follows that the contraction tube and diffuser should be fully simulated. This is in response to the lack

[1] https://bit.ly/3xWusle, accessed on 27 February 2023

of certainty concerning the effect of the domain shape on the final solution - by including these wind tunnel elements in the solution, it can be concluded that the relevant interaction effects within the wind tunnel are being accurately simulated. This is opposed to a constant cross-section domain, where the length of the domain itself may have unwanted, and possibly non-physical effects on the solution.

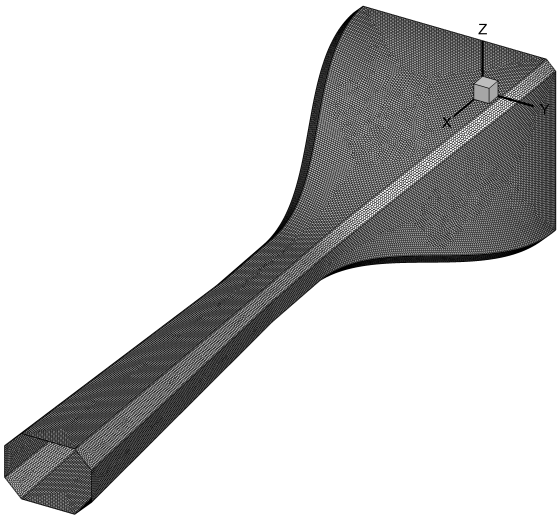

Figure 3.3: View of the polyhedral discretisation of the LTT walls

Using Figure 3.1 for reference, a CAD model of the LTT was built spanning the contraction tube, test section and diffuser. The anti-turbulence screens were omitted since the challenge of accurately predicting its behaviour using CFD is outside the scope of the proposed investigation. This model can be seen in Figure 3.2a, and its mesh in Figure 3.3. A viscous, compressible RANS simulation was set up where the walls were modelled as inviscid, since this effect can be considered negligible [44]. A hybrid poly/hexahedral mesh with around 0.5×10^6 elements was used, with second-order accurate differencing schemes and the Semi-Implicit Method for Pressure Linked Equations (SIMPLE) algorithm. With a velocity inlet set at 3 m/s and a pressure outlet set at 0 Pa, a test section speed of around 55 m/s is achieved - see Figure 3.2b. Applying the incompressible continuity equation for an inviscid fluid and assuming a contraction ratio of 17.8, an analytical velocity of 53.4 m/s is obtained - in good agreement with the numerical solution. Ultimately, this geometry with some similar combination of solver settings will be used for the simulations, with a model of the Flying V at its centre, rotated for any given configuration.

4

Corrections for wall interference

In this chapter, the concept of wall interference in wind tunnel testing is introduced and solutions to mitigate their effects are described. First, the classical corrections are shown which adapt the wind tunnel measurements, then flexible walls are discussed which aim to fully mitigate the physical effects of the walls. This is followed by advanced numerical corrections featuring CFD, where their applicability to this investigation is explored. Finally, the effectiveness of the corrections is evaluated for straight and highly swept wings.

4.1. Wall interference

The physical conditions that a test article encounters during the test are altered by the presence of wind tunnel test section boundaries. Therefore, anytime data from one tunnel is compared to another or is related to a free-air condition, wall interference corrections must be applied to the test results. Ulbrich summarised wind tunnel wall interference in [50] while the full corrections and their derivations can be found in [20, 17] which are generally considered the definitive sources for this material. The test article's physical environment during a wind tunnel test is essentially described by (a) the dynamic pressure, (b) the Mach number, and (c) the angle of attack at the test article's location. These figures are corrected for wall interference in order to properly present the test findings.

First order corrections refer to the simplest wall interference corrections for dynamic pressure, Mach number, and angle of attack. They make bulk adjustments to the test data's most significant alterations brought on by the existence of test section boundaries. Within the test section volume, wall interference adjustments vary. They depend on the coordinates of the selected reference point. The first-order corrections are therefore calculated at a preset place on the model or as a weighted average of data that were calculated at various reference point locations on the test article. Using three distinct numerical values, this method enables the correction of dynamic pressure, Mach number, and angle of attack. The term *blockage corrections* is another name for the dynamic pressure and the Mach number adjustment. When the streamlines are compared to those in free-air, the difference reveals how the test section borders affect the flow-field. The *blockage factor* serves as the direct source of both blockage corrections. This number represents the ratio of the flow's reference velocity to the axial interference velocity brought on by the test section borders. The stream angle at the site of the test article is likewise changed by the test section borders. In order to accurately represent the flow angle observed by the test article, an angle of attack adjustment must be added to the test data. The ratio between the upwash velocity caused by wall interference and the reference velocity of the tunnel at the reference positions for the test piece is used to calculate the angle of attack adjustment. It is often a negative value for positive lift in an open jet, slotted wall, or perforated wall test segment and a positive value for lift in a closed wall test section.

4.2. Classical corrections

In this section, the most relevant classical corrections will be explored in the detail. These include the effect of the support structure, referred to as the *model-off* corrections; the effect of the longitudinal

pressure gradient referred to as the *buoyancy* corrections; the effect of the reduced cross-sectional area in the wind tunnel at the location of the model referred to as the *solid* and *wake blockage* corrections; and finally, the influence of the model on the local angle of attack referred to as *lift interference*.

4.2.1. Model-off corrections

To remove the loads exerted on the support structure from the data, wind tunnel model-off data must be used. Given the focus of the experiment, the coefficients of lift, drag and pitching moment, C_L, C_D and C_m, respectively, are deemed relevant. With the model off in the wind tunnel, each coefficient is measured by the balance with this later being subtracted from the uncorrected measurements. In Equation 4.1, C_D is considered for illustrative purposes, with the subscript unc denoting the uncorrected measurements, and mo the model-off measurements. Naturally, both are a function of wind tunnel and model settings.

$$C_D = C_{D,unc} - C_{D,mo} \tag{4.1}$$

4.2.2. Buoyancy

As can be seen in Figure 3.2a, the diffuser of the wind tunnel is slightly divergent, which reduces the longitudinal pressure gradient. Hence, buoyancy can be neglected in the corrections.

4.2.3. Solid blockage

To correct the measurements for solid blockage, a *blockage factor* ϵ_{sb} is computed for each model component with Equation 4.2, in this case only the wing, since there are no tail surfaces or fuselage. The body shape factor, K and tunnel factor, τ_1 can be obtained from the relations developed by Barlow et al. [9] which correlate the geometry and/or wind tunnel dimensions to a respective value. V and C describe the volume of the component and cross-sectional area of the tunnel, respectively. The blockage effect of the struts can similarly be obtained with Equation 4.3, where AF is the frontal area of the strut. Below, the subscript sb relates to the solid blockage, while st relates to the struts.

$$\epsilon_{sb} = \frac{K \cdot \tau_1 \cdot V}{C^{1.5}} \tag{4.2}$$

$$\epsilon_{st} = \frac{1}{2}\frac{AF_{st}}{C} \tag{4.3}$$

4.2.4. Wake blockage

The wake blockage corrections are broken down into two contributions: the separated and attached wake corrections. This procedure involves some method to identify flow separation, which is not trivial for the flow over the Flying V. Assuming this is done correctly, each contribution can be calculated with the relations given in Equations 4.4 and 4.5, where $C_{D,0}$ and $C_{D,s}$ are the attached and separated drag contributions in coefficient form, respectively. Their sum forms the total wake blockage correction factor.

$$\epsilon_{wb,0} = \frac{S}{4C} \cdot C_{D,0} \tag{4.4}$$

$$\epsilon_{wb,s} = \frac{5S}{4C} \cdot C_{D,s} \tag{4.5}$$

4.2.5. Lift interference

To correct the angle of attack, Equation 4.6 and Equation 4.7 are used. Here, $\Delta\alpha_{uw}$ represents the change in angle of attack due to the upwash of the wing, while $\Delta\alpha_{sc}$ is the change in angle of attack due to the upwash gradient. By adding these two contributions together, the total change in angle of attack is obtained. Furthermore, the lift coefficient does not need to be corrected this way [17]. On the other hand, the drag coefficient must be corrected by applying Equation 4.8, where $\Delta C_{D,w}$ is a function of the lift generated by the wing.

$$\Delta\alpha_{uw} = \delta\frac{S}{\bar{c}}C_L \tag{4.6}$$

$$\Delta\alpha_{sc} = \Delta\alpha_{uw}\tau_2 \tag{4.7}$$

$$\Delta C_D = \delta\frac{S}{\bar{c}}C_L^2 \tag{4.8}$$

The boundary correction factor, δ and the tunnel factor, τ_2 are once again calculated from the relations in the literature of Barlow et al. The former is a function of effective span, wind tunnel width, and wind tunnel height, and the latter is a function of tail length. The effective span is given in Equation 4.9. The tail arm of the Flying V can be assumed to be a function of its mean aerodynamic chord.

$$b_e = b \cdot \frac{1 + \frac{b_v}{b}}{2} \tag{4.9}$$

A similar procedure can be used to obtain the sideforce correction of the vertical fins. In the case of the Flying V, the unusually tall winglets act as the vertical fin.

$$\Delta\beta_{uw} = \delta_{vt} \cdot \frac{S_{vt}}{c_{vt}} \cdot C_{y,vt} \tag{4.10}$$

$$\Delta\beta_{sc} = \Delta\beta_{uw} \cdot \tau_{2,vt} \tag{4.11}$$

$$\Delta C_{D,vt} = \delta_{vt} \cdot \frac{S_{vt}}{c_{vt}} \cdot C_{y,vt}^2 \tag{4.12}$$

$$\Delta C_{n,vt} = \frac{1}{8} \cdot \Delta\beta_{sc} \cdot \frac{dC_y}{d\beta} \tag{4.13}$$

4.2.6. Total corrections

Once all the correction factors are known, the data can be corrected. To correct the freestream velocity, dynamic pressure and lift coefficient, Equations 4.14 through 4.16 can be used, respectively.

$$q = q_{unc}(1 + \epsilon_{tot}) \tag{4.14}$$

$$C_L = \frac{C_{L,unc}}{(1 + \epsilon_{tot})^2} \tag{4.15}$$

$$V = V_{unc}(1 + \epsilon_{tot}) \tag{4.16}$$

The total correction factor ϵ_{tot} is the total sum of all blockage factors computed previously. Correcting the coefficients of drag, and moment as well as the angles of attack, and sideslip, is a straightforward procedure shown in Equations 4.17 through 4.20.

$$C_D = \frac{C_{D,unc}}{(1 + \epsilon_{tot})^2} + \Delta C_{D,w} + \Delta C_{D,vt} \tag{4.17}$$

$$C_m = C_{m,unc} + \Delta C_{m,vt} \tag{4.18}$$

$$\alpha = \alpha_{unc} + \Delta\alpha_{uw} + \Delta\alpha_{sc} \tag{4.19}$$

$$\beta = \beta_{unc} + \Delta\beta_{uw} + \Delta\beta_{sc} \tag{4.20}$$

4.3. Flexible walls

Flexible wind tunnel walls can remove the problem of wall interference corrections in experimental simulations by allowing the wall of the tunnel to move as a function of the local pressure differences generated by the test model. This eliminates the pressure discrepancies caused by wall interference. Flexible walls are typically made from a thin, lightweight material that can deform subject to attached actuators, allowing the wall to conform to the changing flow conditions in the tunnel. The ability to adjust the shape of the wall in real-time helps to mitigate the effects of wall interference, providing more reliable and accurate results for experiments [55].

While providing a solution to the problem of wall interference correction, flexible walls also have some limitations, namely cost, complexity, maintenance, reliability and response time. Consider a wind tunnel with a circular cross-section, whose wall(s) is completely flexible. Such a system would require a dense array of actuators to achieve a smooth, sufficiently accurate deformed surface. It is also necessary to route the mounting system of the test article and the measurement equipment through this array of actuators. On top of this, the wall material must be able to withstand the pressures of the wind tunnel as well as the fatigue associated with the constant geometry changes. The actuators must also be easily accessible for a maintenance operator and naturally, this must all fit within an acceptable budget. Even if a given laboratory had access to such a budget that could address all of the above, the experiments would still be mainly limited to steady flows given that the wall would be unable, in most cases, to deform rapidly and reliably enough to accommodate transient effects.

4.4. Numerical approach

Numerical corrections rely on simulations of the test article in both free-air and wind tunnel conditions. The results are then compared and the effect of the wind tunnel is inferred. Special care must be taken when simulating and/or modelling the test article and its conditions. It is important that relevant phenomena are not overlooked such that the results are accurate and sufficiently representative of the true flow conditions. In the proposed work, the most relevant phenomenon is that of leading-edge vortices.

As a result, RANS is proposed as the most cost-efficient solution that is sufficiently accurate. Modifications to the turbulence model are strongly recommended, if not required. The boundary layer at the inlet of the numerical wind tunnel will not be simulated as it is understood from [44] that its effect on the flow-field around the body of interest is negligible and can save substantial computational resources.

Due to the nature of the Flying V's design, numerical corrections are the most reliable approach towards obtaining accurate corrections. This is due to the crescent wing of the aircraft and the proposed flow angles for the experimental campaign in 2024. The corrections developed by Barlow et al. for streamline curvature [9, 41] are only valid under the assumption of two-dimensional flow over non-crescent aerodynamic surfaces. Further, the highly swept wings create leading vortices at considerably low angles of attack for which the classical corrections are typically not well suited [17]. Finally, the model is expected to be large in comparison to the wind tunnel ($b/b_w = 1.4/1.8 = 0.\dot{7}$) and the flow angles quite high ($\alpha \geq 40$, $\beta \geq 20$), and as such the blockage effects will be strong. In other words, the streamline curvature will be strongly affected by the walls. In this situation, the use of advanced methods is recommended since simpler methods fail to account for these effects with sufficient accuracy.

4.5. Effects on a straight wing

The work of Haque et al. [26] investigates the effectiveness of numerical corrections, obtained through solving the RANS equations, by comparing them to two analytical methods, one of which can be found in section 4.2. The researchers used a straight wing with the NACA-65(3)-218 airfoil as its profile. Results for lift, drag and pitching moment were collected for angles of attack between -10° and 15°, roughly at increments of 1°. The conclusion drawn was that both analytical methods performed equally, with their effects being most noticeable at high angles of attack. The discrepancies with the CFD results are negligible. The changes to the flow-field due to the presence of the walls are minimal with their effect (i.e.: $\Delta\alpha$) being accounted for by the corrections; the lift, drag and moment coefficients were also accurately adjusted. This paper thus validates the relations given in section 4.2 and further proves, to a certain extent, that RANS calculations are not strictly necessary for the corrections of straight wings in rectangular wind tunnels. In conjunction with the work of Barlow et al. [9], these sources make it clear that the analytical approach offers a similar level of accuracy at virtually no computational cost in this situation.

4.6. Effects on a swept wing

Experimental and numerical investigations have been carried out on lambda and delta wings, akin to the Flying V, and attempts have even been made to identify the effects of wind tunnel interference on their performance. This section will cover the complex flow dynamics that are present over highly swept lambda wings and previous attempts at identifying said interference on delta wings.

4.6.1. Flow characteristics

This section uses as its reference the work of Rein and Gartner [43] and Ruetten et al. [45]. In the former, the flow over the lee (upper) side of a generic lambda wing is investigated in detail, while in the latter, the effect of morphing leading edges on the manoeuvrability of Unmanned Combat Air Vehicles (UCAVs) is explored. The vortical flows over the leeside of both delta and lambda wings are "significantly governed" by the sweep angle and the shape of the leading edge. In such literature, swept wings are categorised as *slender* ($\Lambda_{LE} \leq 65°$) or *non-slender* ($\Lambda_{LE} < 65°$) [37]. Round leading edges, such as those found on the Flying V, make the location of the leading edge vortices more susceptible to changes in flow conditions and local geometry. Consider Figure 4.1 - here both the streamlines and streamsurfaces are shown over a generic lambda wing. The dual vortex system, well illustrated by Gursul et al. [24], which forms near the apex and mid-wing is hard to miss. Simulating this viscous behaviour is paramount and necessitates at least a RANS CFD simulation for acceptable accuracy. Lower fidelity methods, such as Vortex Lattice Methods (VLMs) are not suitable. Further, in an extensive literature review, Jobe proved the inadequacy of empirical methods for predicting the behaviour of these vortices, including the location of their breakdown [28]. In the same report, the author claims that numerically solving the Navier-Stokes can accurately simulate this behaviour for laminar flow, with some uncertainty for turbulent flow due the difficulties involved with validation. The details of the empirical methods detailed in [28] are not considered to be within the scope of this report.

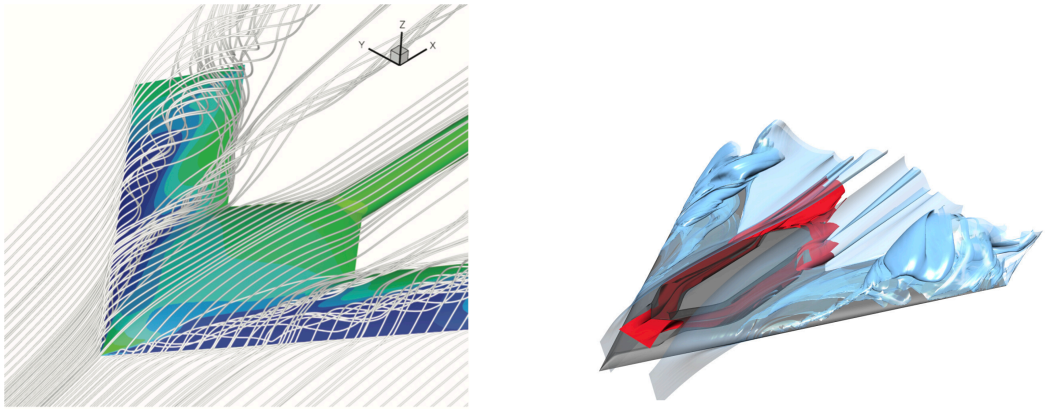

(a) Streamlines over leeside [43]

(b) Streamsurfaces over leeside [45]

Figure 4.1: Vortical structures over a generic lambda wing

Figure 4.1b illustrates the vortex *breakdown* phenomenon which is the abrupt expansion and subsequent disorderly evolution of the typically well-organised, spiralling, leading-edge vortex flow over the upper surface [28]. Current turbulence models have difficulties accurately predicting these free shear layers, so caution must be taken during the setup of the simulation and analysis of the results. When the Flying V scale model is eventually tested in the LTT, the results of the proposed investigation should be thoroughly validated with this newly collected data. As of the time of writing, the Flying V features a leading edge sweep of 64°; higher than the 54° of the generic lambda wing used in the reference papers. A similar flow structure is expected since the leading edge around the middle of the Flying V's wing is fairly round, much like part of the generic lambda wing. In fact, the sharper sweep should only intensify the strength of the vortex. The development of the vortices and the location of their breakdown will largely determine the stall characteristics of the Flying V, and therefore, understanding their behaviour is crucial for the stability and control analysis of the Flying V in the future. The proposed investigation will deepen the understanding of interference effects on the results collected in the experimental campaign in 2024.

4.6.2. Wall interference

This section will focus on the investigation of Allan et al. [2] on the effect of wind tunnel interference on the aerodynamics of delta wings. The work involved various RANS simulations on a delta wing with a 65° leading edge sweep angle - compared to the Flying V's 64.3°. The geometry is shown in Figure 4.2. To determine the various effects of the walls on the vortical flow, these simulations were compared to equivalent conditions in free-air. The study confirmed that RANS can adequately model the leeward surface flow over delta wings and account for the nuanced effects of the walls. A previous literature study by Verhaagen summarised how various empirical correction methods could not account for vortex breakdown at high AoAs [52]. Combined, these sources provide a strong argument for the use of high-fidelity CFD for the proposed investigation. Moreover, prior to the investigation, the authors found sources to suggest that the blockage ratio strongly affects the breakdown of vortices while wall effects in general can be neglected for a ratio smaller than 0.08.

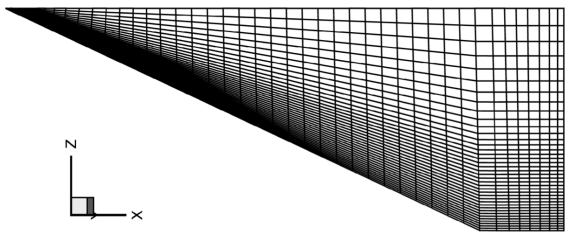

Figure 4.2: Discretised geometry of the delta wing in [2]

The study conducted RANS simulations on a delta wing in three wind tunnels, both in static and pitching configurations. One wind tunnel featured a square cross-section, with the other two having rectangular cross-sections, with either the sides closer to the model (2x3 configuration) or roof/floor (3x2 configuration) closer to the model. The findings indicated that the presence of tunnel walls promoted vortex breakdown, with proximity to side walls being the most influential factor. In contrast, proximity to the roof and floor had a minimal impact on vortex breakdown. It was inferred from Figure 4.3b that by placing the side walls closer to the wing more strongly concentrated the circulation within the vortices, increasing the suction and by extension velocity at their core, and decreasing the pressure at the surface of the wing. As the vortex travels downstream towards a higher pressure region, it then sees a stronger adverse pressure gradient towards the trailing edge, as compared to the free-air scenario, and ultimately, this gradient is responsible for advancing the onset of vortex breakdown. This is evidenced in Figure 4.3a. The increased vorticity makes pitching moment corrections more complicated, as the effect of the walls can lead to stronger vortices and subsequent pitch-breaks which are not present in free-air conditions - another argument against linear corrections.

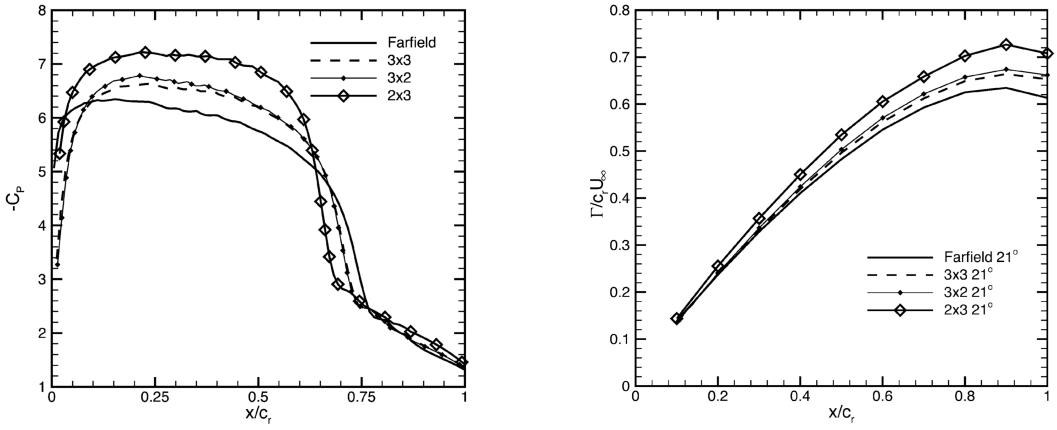

(a) Pressure coefficient along vortex core

(b) Circulation distribution

Figure 4.3: Comparison of vortex variables for different wind tunnel configurations [2]

The authors also focused on the effect of wall interference on the vortices during pitching motion. This extends slightly beyond the scope of the proposed investigation, but the key takeaways is that the extent of variation in vortex breakdown was a function of the wing's position in the pitching cycle. This may warrant a future investigation on the vortex behaviour over the Flying V in a dynamic environment.

Of special interest to the proposed investigation, is the fact that the authors claim the report's findings are consistent with a previous investigation that applied the Euler equations, which as will be mentioned in chapter 6, neglect viscous effects. As a matter of fact, the tunnel interference trends identified in this study were identical to a previous Euler investigation by the same authors [1]. It must be noted that while this investigation focused on a configuration with a similar leading edge sweep to that of the Flying V (65° for the delta wing vs. 64.3°), the delta wing in question features a sharp leading edge, and for the Euler investigation, the authors placed fences strategically on the wing where secondary vortices/separation was expected. This meant that the Euler investigation required *a priori* knowledge of the flow-field, and moreover, sharp leading edges have a far higher propensity to generate vortices than blunt ones for the same sweep. That is to say that the ability to predict leading edge vortices with an Euler method is not the same for this delta wing as for the Flying V, although this calls for further exploration.

5

Reynolds number effects

The Reynolds number (Re) is a dimensionless parameter that characterises the viscous flow regime around an object, and it plays an important role in external aircraft aerodynamics. The Reynolds number is defined as the ratio of inertial forces to viscous forces and is given by Equation 5.1:

$$Re = \frac{\rho u L}{\mu} \tag{5.1}$$

where ρ is the density of the fluid, u is the velocity of the flow, L is a characteristic length scale of the object, and μ is the dynamic viscosity of the fluid. At low Reynolds numbers, the flow is laminar, and the boundary layer around the object is relatively thicker (higher relative momentum thickness) yet more stable - the stream-wise velocity varies uniformly within its confines. As the Reynolds number increases, the flow transitions to a turbulent regime, and the boundary layer becomes thinner and more prone to instabilites, possibly with swirling flows within it. For highly swept wings, the effect of Reynolds number is particularly significant due to the strong coupling between the sweep angle and the boundary layer. In this chapter, the Reynolds number effects will be investigated for the case of 2D airfoils, full wings, and finally, the special case of highly swept wings.

5.1. Two dimensional effects

The study in question examined the impact of Reynolds number on the aerodynamics of the NACA 0021 airfoil with moderate thickness through surface-pressure measurements [12]. The aspect ratio of the wing was limited to 1.5 to allow for full rotation within the wind tunnel, with elliptical end-plates installed at either end of the wing as seen in Figure 5.1. The authors acknowledge that they still expect the flow-field to remain largely three-dimensional, and that the applicability of such a method to 2D "remains to be verified". A high-pressure wind tunnel was used to vary the chord Reynolds number between 5.0×10^5 and 7.9×10^6. The angle of attack was incrementally increased from 0° to 40°, covering both attached and stalled conditions across all Reynolds numbers. The study investigated attached and separated conditions, static stall, and reattachment processes. A significant change in flow behaviour was observed around $Re = 2.0 \times 10^6$, where the stall type shifted gradually from trailing-edge stall to leading-edge stall. With increasing Reynolds number, both the stall angle and the maximum lift coefficient increased. When the flow was separated, the separation point moved upstream, and the suction peak decreased in magnitude. Two types of hysteresis in reattachment were identified. Corrections for wind tunnel wall interference effects were implemented and the findings were compared against third party data from [4]. A data excerpt comparing the lift coefficient at various Reynolds numbers is shown in Figure 5.2.

5.2. Three dimensional effects

The study by Yan et al. involved an investigation into a NACA 0012 wing model with a moderate sweep-back angle of 38° [56]. The finite wing possessed an aspect ratio of 10. Surface-flow fields were examined by employing both smoke wire and surface oil-flow schemes. The smoke-streak flow

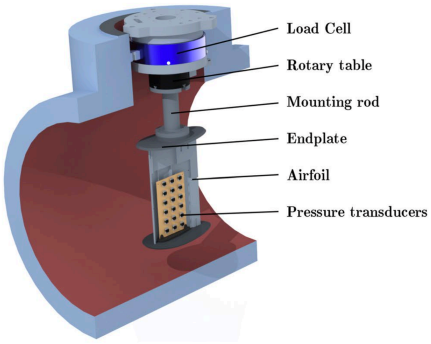

Figure 5.1: Cutaway CAD rendering of the test section from [12]

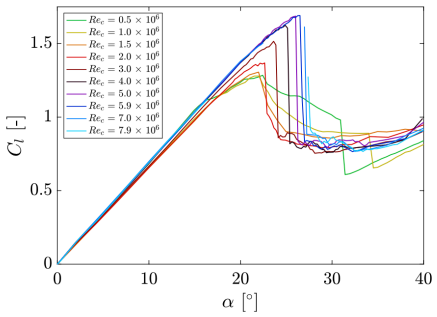

Figure 5.2: Effect of increasing Reynolds number on lift coefficient [12]

patterns at low Reynolds numbers ($Re < 1.5 \times 10^4$), revealed the existence of five characteristic flow modes: attached surface flow, trailing edge separation, separation vortex, leading edge separation, and bluff-body wake. On the other hand, at high Reynolds numbers ($Re > 3.0 \times 10^4$), the surface oil-flow patterns indicated the presence of six characteristic flow modes: laminar separation, separation bubble, leading edge bubble, bubble extension, bubble burst, and turbulent boundary layer. This should elucidate the profound effect Re has on the flow-field. To determine the velocity field around the wing, particle image velocimetry (PIV) was utilised. The aerodynamic loadings were measured using a six-component balance.

Changing the Reynolds number changes the fundamental behaviour of the boundary layer and its separation, and as a result, the aerodynamic performance at any given angle of attack can see a strong sensitivity to the Reynolds number. Under more general terms, increasing the Re decreases the relative thickness of the boundary layer while making it more turbulent. This can, in turn, make it more resistant to adverse pressure gradients, postponing stall, reducing the severity of stall, and therefore possibly reducing form drag. As a result of the increased turbulence, however, skin drag increases. This complexity precludes any conclusion as to the effect of Re on total drag at any given angle of attack for any given configuration, since the flow will be largely determined by the local conditions, and subtle differences in geometry.

5.3. Highly swept wings

While the former study focused on a moderately swept wing, it is important to recall the complex flows over highly swept wings, covered in subsection 4.6.1. These highly vortical flows naturally are strongly dominated by viscous effects and as such, are more susceptible to Reynolds number effects.

The numerical simulations realised by Lin et al. [31] investigate the effect of Reynolds number on the SACCON configuration which features a 65° leading edge sweep angle and an aspect ratio of roughly 1.5. The Langtry-Menter turbulence model is employed incorporating a helicity cross-flow correction to improve the accuracy of transition prediction. The helicity parameters were calibrated to improve the accuracy of the numerical model with test results of the DLR-F5 wing being used for verification. The numerical method was then validated by comparing its results with existing aerodynamic force and moment data of the SACCON model. Following this validation, the Reynolds number effects on the aerodynamic and flow-field characteristics of the flying wing were analysed. The simulation primarily investigated the high subsonic regime ($Ma = 0.9$), with the chord Reynolds number ranging from 2.0×10^6 to 80×10^6 - which includes the test and flight Reynolds number. The influence of turbulence on the surface flow pattern and drag characteristics was also studied. The results showed that the separation behaviour is strongly dependent on the Re, as evidenced by the discrepancies in the skin friction contours in Figure 5.3. The calculation results show that turbulence over 0.4% significantly affects the surface laminar flow range and total drag coefficient.

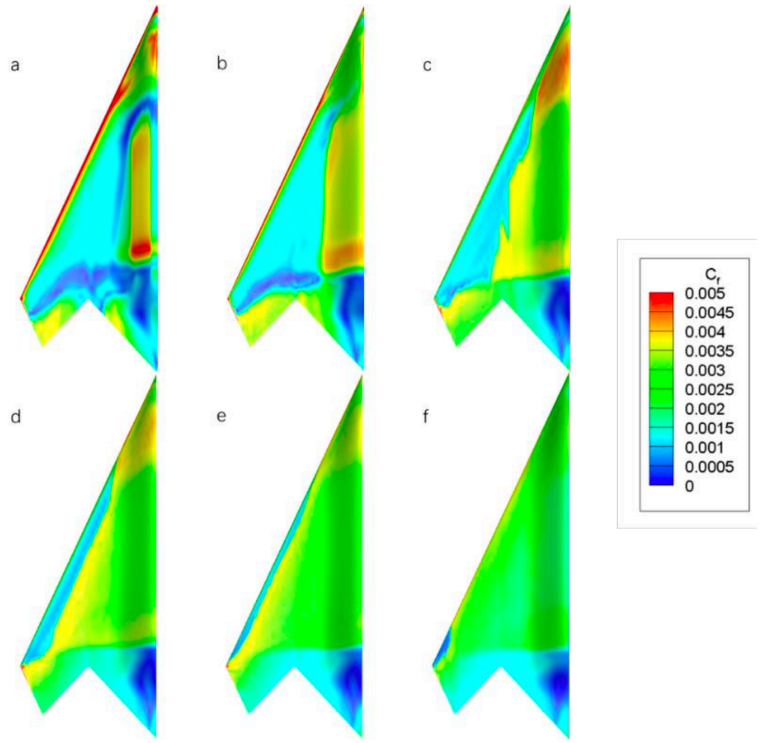

Figure 5.3: Skin friction coefficient (C_f) distributions on the upper surface of the flying wing model at different Reynolds numbers ($Ma = 0.9, \alpha = 2°, Tu = 0.1\%$): (a) $Re = 1.0 \times 10^6$; (b) $Re = 2.0 \times 10^6$; (c) $Re = 5.0 \times 10^6$; (d) $Re = 10 \times 10^6$; (e) $Re = 20 \times 10^6$; (f) Re = 80×10^6 [31]

From Figure 5.3, it can be seen that at a lower Re, there is strong separation near the trailing edge along most of the span and also near the centrebody, illustrated by the dark blue regions. At the highest value of Re, the skin friction coefficient is moderate and homogeneous, indicating nicely attached flow across the surface, only separating after the centrebody near the root where there is a shock wave and strong curvature. At $Re = 10 \times 10^6$ a clear separation bubble is formed along the leading edge. While it is hard to tell how or if the leading edge vortices are affected, the effect on the boundary layer is clear - the higher Re flow is much less prone to separation with potential non-linear phenomena at moderate values.

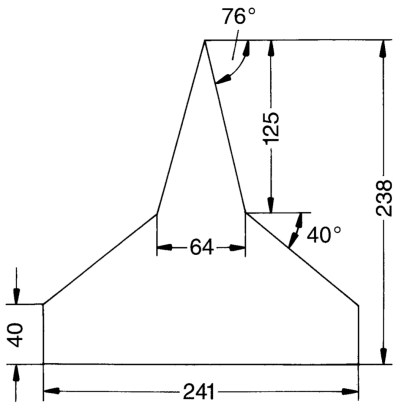

(a) Geometry of the double delta wing

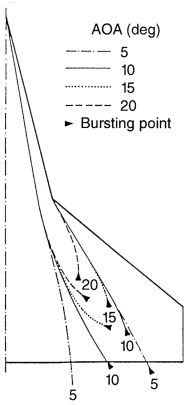

(b) Vortex trajectory and breakdown over double delta for various angles of attack

Figure 5.4: Results from the investigation of Re on vortex breakdown [27]

A separate study by Hebbar et al. further explored the effect of Re on vortex breakdown over a double delta wing [27]. This experimental study was conducted at the Naval Postgraduate School water tunnel facility to investigate the high-incidence vortical flow-field over a 76/40° double-delta wing model with sharp leading edges. The study was carried out at three nominal flow Reynolds numbers of 15 000, 45 000, and 75 000 (based on centerline chord), and included flow visualisation studies with a dye-injection technique, followed by laser Doppler velocimetry (LDV) measurements. The main aim of the study was to determine the influence of Reynolds number on vortex interactions/trajectories, and breakdown. The results showed that, unsurprisingly, there is a significant influence of Reynolds number. With an increase in Reynolds number, the strake and wing vortex trajectories tended to move outwards and closer to the model surface, and the vortex breakdown location moved forwards towards the apex of the model. The vortex interaction phenomenon's intertwining or coiling-up feature became less dominant and disappeared altogether at high Reynolds numbers. These trends in the vortex interaction and bursting data were found to be consistent with previous wind tunnel data. The geometry is shown in Figure 5.4a, with the effect of α on vortex core trajectory illustrated in Figure 5.4b. The authors thoroughly documented the vortex formation and breakdown over various Re, whose figures clearly show the trajectory of both the wing and strake vortex, as well as their breakdown. The results are summarised in Table 5.1, with the measurements being taken relative to the apex.

Table 5.1: Vortex breakdown location from LDV measurements at an angle of attack of 15° [27]

Reynolds number	Strake vortex breakdown location			Wing vortex breakdown location		
	x (mm)	y (mm)	z (mm)	x (mm)	y (mm)	z (mm)
15 000	227	40.6	13.5	200	20.0	7.30
45 000	215	42.0	11.4	178	45.7	10.8
75 000	200	38.0	12.1	168	49.9	6.3

6

Computational fluid dynamics methods

Given the project's heavy dependence on high-fidelity, subsonic CFD, it is crucial to understand its inner workings alongside the benefits, limitations and best practices. First, it should be mentioned that for this flow regime, there are two major techniques that can be employed. Either the steady-state Reynolds-Averaged Navier-Stokes (RANS) equations are numerically solved or the transient Lattice Boltzmann Method (LBM) is employed. In both cases, the phenomenon of turbulence cannot be solved directly and must be modelled instead. A simplified form of the RANS equations, known as the Euler equations are also covered, including its disadvantages. In this chapter, all of the above will be considered although mathematical equations and derivations will be mostly omitted since they are not considered to be within the scope of the report.

6.1. Reynolds-Averaged Navier-Stokes equations

RANS CFD simulations are the most conventional approach for full aircraft aerodynamic analysis since it offers the best compromise between accuracy and computational cost [11, 21]. Here, only the basic foundations (including benefits and limitations) and the standard practices/techniques will be discussed.

The RANS equations are a reduced form of the general Navier-Stokes (NS) equations, where the steady-state solution to these equations is decoupled from the system's time-varying fluctuations. These fluctuations account for the phenomenon of turbulence[1]. By eliminating the time variable in part or whole, time averaging is frequently employed to simplify complex systems of differential equations. When RANS equations are used, the solution is divided into a mean flow velocity that is independent of time and time-varying fluctuations around the mean. In Equation 6.1, the instantaneous velocity (left-hand side), is broken down into its mean and fluctuating terms (right-hand side), respectively:

$$u(\boldsymbol{x}, t) = \bar{u}(\boldsymbol{x}) + u'(\boldsymbol{x}, t) \tag{6.1}$$

Applying this *Reynolds decomposition* to the conservation of momentum yields Equation 6.2, shown in tensor notation after applying temporal averaging:

$$\rho \bar{u}_j \frac{\partial \bar{u}_i}{\partial x_j} = \rho \bar{f}_i + \frac{\partial}{\partial x_j} \left[-\bar{p}\delta_{ij} + 2\mu_t \bar{S}_{ij} - \rho \overline{u_i' u_j'} \right] \tag{6.2}$$

Where ρ is the fluid density; $\bar{u}$ is the mean velocity, with the subscript denoting an arbitrary direction; $\bar{f}$ are the averaged body forces, if present; $\bar{p}$ is the averaged pressure; δ_{ij} is the Kronecker delta, a function with a similar purpose to the identity matrix; μ_t is the eddy viscosity, and $\bar{S}_{ij}$ is the mean strain rate tensor. When solving this equation, a problem arises when obtaining $\rho \overline{u_i' u_j'}$, referred to as the *Reynolds stress tensor* [7]. This particular term can account for anisotropic turbulence. The averages

[1] https://bit.ly/3XUcPOf, accessed on 25 January 2023

of a group of non-linear derivative terms are typically included in this term's temporal dependency. Although this model has the potential to be extremely complex, it also allows for some flexibility in application, given the omission of some variables in the strain and/or stress tensors. In order to account for these non-linear elements in the stress tensor, an extra turbulence model is necessary. Instead of being developed from first principles, the majority of turbulence models employed in the RANS equations are established from empirical evidence.

Menter's Shear Stress Transport $k-\omega$ (SST $k-\omega$) turbulence model [35] is a two-equation eddy-viscosity model which has become very popular and is an appropriate choice in the majority of cases for external aerodynamics [23]. The SST $k-\omega$ model uses two transport equations, one for the turbulent kinetic energy (k) and one for the specific turbulence dissipation rate (ω), to predict the turbulence in the flow. The equation for k is similar to that of the standard $k-\omega$ model, but with a term added to account for the effects of the shear stress on the turbulence. The equation for ω includes a term for the production of turbulence, as well as a term for its dissipation. The SST model also includes a *shear stress transport* closure, which is used to model the turbulent viscosity. This closure is based on the concept of *eddy viscosity*, which represents the turbulent motions in the fluid as a *virtual* viscosity. The SST closure allows the model to predict the transition from laminar to turbulent flow in boundary layers more accurately than traditional turbulence models.

The Spalart-Allmaras (SA) model, by contrast, is a one-equation model. It uses a transport equation for kinematic eddy turbulence viscosity and was designed specifically for aerospace applications with wall-bounded flows in mind. It has been proven to show good agreement for boundary layers subjected to adverse pressure gradients [46]. Originally, it was more suited for low-Reynolds numbers, requiring the viscosity-affected region of the boundary layer to be properly resolved ($y+ \approx 1$ meshes), although more modern implementations have attempted to add more sophisticated wall treatment [6]. The model is not well suited for some free shear flows, and in addition, cannot be relied on to predict the decay of homogeneous, isotropic turbulence [47].

6.1.1. Limitations

The limitations of RANS are comprehensively detailed in a NASA report by Bush et al. [13] and are a highly contended topic. Due to the nature of turbulence models, there are inherent inaccuracies in predicting viscous effects, however, small changes can be made to their calibration parameters to improve their accuracy *in specific scenarios*. Spalart et al., for instance, have developed a correction for the SA model which improves skin friction predictions at low Reynolds numbers, although as a result, the prediction of channel flows sees a small penalty [48]. In this section, only the limitations relevant to the proposed investigations are considered, with potential enhancements being discussed in subsection 6.1.2 when available.

Consider the flow over the Flying V in subsonic conditions at a moderate angle of attack. The aircraft features a crescent wing with highly swept leading edge. Despite the relatively blunt leading edge, vortices are expected to be formed at the leading edge which travel downstream over the body in the chord- and span-wise direction until they eventually break down. Bush et al. observed that while RANS-based CFD can predict the locations where vortices form over sharp leading edges accurately, this is not necessarily the case over blunt leading edges. Further inaccuracies are observed with regard to vortex breakdowns. This is unfortunate given that the behaviour of vortices over the Flying V is expected to have a very significant impact on its performance. Care must be taken with the discretisation and turbulence model settings to maximise the accuracy, and hence applicability, of the results. Various RANS validation papers, such as the work of Nelson et al. [40], reveal RANS's limitations in accurately predicting pitching and various other moment coefficients. While the cause is not completely understood, it is expected that the discrepancy follows from small errors in the pressure distribution predictions that are amplified when calculating the moments but aren't as pronounced in the lift and drag calculations. Any interpretation of the moment coefficient data must bear this limitation in mind.

6.1.2. Best practices

Following from above, formal literature has been published advising the best methods for achieving high-accuracy, reliable results when applying this type of tool. Goetten et al. released a review of

guidelines [23] for the APISAT[2] in 2019. This specific document focuses on subsonic simulations of external aerodynamics, which is aligned with the proposed investigation. Recommendations for geometry preparation, turbulence model modifications, as well as surface and volume mesh refinements, are given.

Starting with the geometry, it should be watertight without sharp edges. This involves truncating or rounding any sharp trailing edges as this ensures high-quality elements form at these locations. The authors recommend importing the geometry in STEP or IGES format. As for the cell types, polyhedral cells generally offer better accuracy with fewer cells compared to tetrahedral elements. Ultimately, it is up to the user to choose between hexahedral and polyhedral cells; a compromise between fast meshing or simulation time, respectively. The use of tetrahedral cells is discouraged, unless the geometry is highly complex. The domain should be larger than 50 body lengths, with the outlet being placed at least 10 body lengths away for the model. The authors loosely suggest the use of a bullet-shaped domain such that one surface can be used as a velocity inlet, with the other surface being a pressure outlet. Furthermore, for subsonic simulations, a pressure-based solver is presented as the superior option, paired with a second-order discretisation scheme.

The SST $k-\omega$ model is a robust model for simulating boundary layers under adverse pressure gradients, although small modifications can be made to drastically improve its accuracy. First, a production limiter can be imposed on the turbulent kinetic energy which alleviates the model's tendency to over-predict the eddy viscosity [2]. With this change, small vortices which would otherwise artificially dissipate, are more accurately predicted. Further, non-linear constitutive relations, which should be readily available in most popular commercial RANS codes, can greatly improve the prediction accuracy of near-wall turbulence anisotropy as well as the boundary layer behaviour in separated flows, such as free vortices [18]. Finally, it is strongly recommended to always model the full boundary layer rather than using wall functions. This implies that the $y+$ value, a proxy for the wall-normal height of the first cell, should be smaller than unity. The importance of this condition is very well understood and is documented thoroughly in existing literature [3, 8, 53]. Ideally, adaptive mesh refinement should be implemented which dynamically refines and coarsens the mesh depending on certain gradient-based criteria. This can ensure sufficient resolution at the vortex locations at a minimal computational cost.

6.1.3. Mesh quality criteria

The quality of the surface and volume mesh is crucial for the accuracy and convergence of steady-state RANS calculations. There are several criteria used to evaluate the quality of a mesh[3]:

1. **Aspect ratio**
   Aspect ratio is the ratio of the longest edge to the shortest edge of an element in the mesh. A high aspect ratio indicates that the element is elongated.

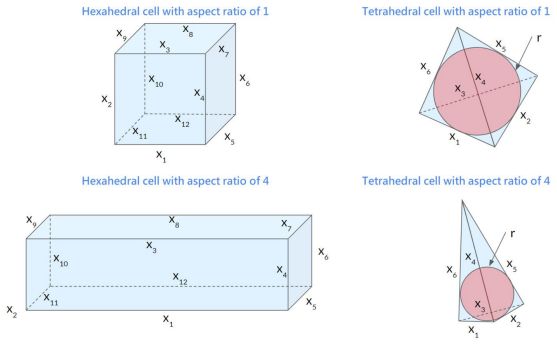

Figure 6.1: Illustration of cell aspect ratio[3]

[2] https://bit.ly/3wxD7d9, accessed on 27 January 2023
[3] https://bit.ly/3ZKy6ut, accessed on 14 March 2023

2. **Skewness**
   Skewness is a measure of how the interior angles of a cell compare to those of an ideal cell.

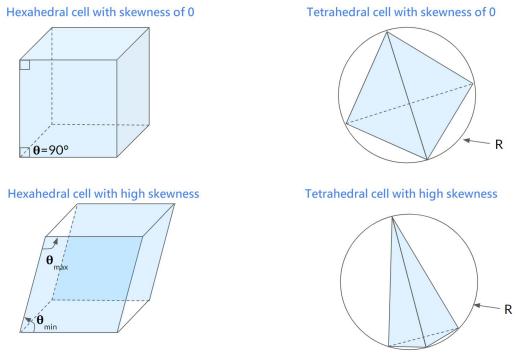

Figure 6.2: Illustration of cell skewness[3]

3. **Non-orthogonality**
   Non-orthogonality measures the deviation between the normal connecting the cell centroid to that of its neighbour, and the normal of their shared face. This is calculated for all the faces of a cell.

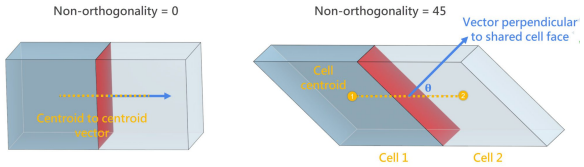

Figure 6.3: Illustration of non-orthogonality mesh quality metric[3]

4. **Volume ratio**
   Volume ratio is the ratio of the cell volume to that of its adjacent cells. A smooth mesh has gradual transitions in volume, area and length (for cells, faces and edges, respectively).

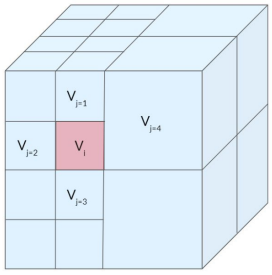

Figure 6.4: Illustration of cell volume ratio[3]

Overall, a high-quality mesh should have low aspect ratios, skewness, and non-orthogonality; be smooth; have appropriate cell distributions such that areas with high gradients are more densely discretised and vice versa; converge as the mesh is refined; and have appropriate grid resolution for the desired level of accuracy.

6.2. Lattice Boltzmann Method

The Lattice Boltzmann Method (LBM) is a numerical method for simulating fluid dynamics that is based on the Boltzmann equation, which describes the behaviour of a gas or fluid in terms of the motion of its individual particles. The LBM is a relatively new approach to CFD that has gained popularity in recent years due to its ability to handle complex geometries and boundary conditions, but mainly due to its parallelisability and efficiency [36].

In LBMs, a fluid is represented as a collection of discrete particles, or *pseudo-particles*, that move and interact with each other according to a set of rules. The fluid is discretised as a lattice, which is a regular, discrete grid in space and time. The pseudo-particles are moved on the lattice according to a set of discrete velocity vectors, which are chosen to represent the fluid flow. The LBM is a collision-streaming method, which means that the particles undergo two steps: a collision step, where the interactions between the particles are calculated, and a streaming step, where the particles are moved according to their velocities. The collision step is used to update the distribution of the particles on the lattice and to calculate the macroscopic properties of the fluid, such as density and velocity. The streaming step is used to move the particles on the lattice, and the new positions are used to calculate the distribution of the particles at the next time step [30].

One of the advantages of the LBM is that it can handle complex geometries by using a *bounce-back* boundary condition. This condition allows the pseudo-particles to interact with solid walls as if they were real particles. LBMs are also able to handle multi-phase and multi-component flows, and are easy to parallelise, which makes them a good choice for large-scale simulations. However, LBMs are not well suited for high Reynolds number nor high Mach number flows and have relatively low accuracy compared to other methods, such as solving the RANS equations with a finite volume method. Due to the use of a regular Cartesian lattice or mesh, LBMs usually lack the required resolution in the boundary layer, which paired with unsophisticated turbulence modelling, means that popular LBM-based solvers such as PowerFLOW[4], can introduce significant errors to the solution, especially with regards to drag [32]. With this in mind, fast advancements in this topic are quickly broadening the range of applications of LBMs. A development by Yuan et al. has allowed for accurate predictions for the drag coefficient of a sphere immersed in a low Mach number flow over a range of moderate Reynolds numbers [57].

6.3. Euler equations

This section uses the work of Anderson et al. [3] as its main reference. The Euler equations, which are also a reduced form of the general NS equations, are a set of partial differential equations derived from the conservation laws of mass, momentum, and energy, and they describe the behaviour of inviscid, compressible fluids. These equations are expressed in terms of the fluid's density, velocity, pressure, and temperature and they govern the behaviour of the fluid in both space and time. By applying the finite volume method, the fluid domain can be discretised into a set of control volumes over which the governing equations can be solved. Much like the RANS approach, the Euler equations must be approximated using a discretisation scheme, and the resulting linearised system can be solved with linear algebra techniques. The resulting discretised equations are solved iteratively to simulate the fluid's behaviour. At each iteration, the numerical solution is updated based on the values of the fluid properties at the control volumes. This method can be either transient or steady-state depending on the assumptions, and naturally can make use of both structured and unstructured grid methods, however, the choice of grid type and other numerical parameters depends on the specific problem being simulated and the computational resources available.

While the Euler equations are a useful tool for simulating fluid flows and can provide accurate results for certain applications, they do have limitations in the context of external aircraft aerodynamics. Namely, viscosity, and consequently turbulence, are completely neglected in this approach. While shock waves can be accurately solved, in the context of subsonic external aerodynamics, this means that this method can only yield information about lift, and lift-induced drag since the free vortices that are formed at the wingtips can still be simulated. With this in mind, since viscosity can be neglected, the boundary layer region of the mesh can be forgone. This region typically requires special treatment in the discretisation phase to ensure accurate results. This allows for simpler meshes, with fewer elements, and fewer calculations per finite element requiring significantly fewer computational resources. Therefore, the faster turnaround times of the Euler method can be worthwhile provided there is a clear understanding of the effects of inviscid flow on the results. It may prove to be a powerful tool for attached flows, for instance at low angles of attack, where the viscous/inviscid interactions are less pronounced.

[4] https://bit.ly/3yJtDML, accessed on 17 March 2023

7

Design of experiments

Given the time and resource constraints imposed on any project, experimental campaigns and high-fidelity numerical investigations must be carried out carefully to ensure a minimum level of quality given the available budget, resources and schedule. This chapter will cover traditional approaches towards obtaining measurements, whether experimental or numerical, as well as the concept of Modern Design of Experiments (MDOE), which aims to reduce the cost of experiments while maintaining a given level of quality.

7.1. One-factor-at-a-time approach

The one factor at a time (OFAT) approach is a widely-used experimental design strategy for investigating the effect of individual factors on a response variable. OFAT involves varying one independent variable at a time while keeping all other variables constant, and as a result, is relatively straightforward and simple to implement [39]. One of its main limitations is that it does not account for possible interactions between factors. In many real-world scenarios, the effect of one variable on the response may depend on the value of another variable, and in aircraft aerodynamics, these effects can be strongly coupled. Therefore, if there are interactions between variables, the OFAT approach may miss these effects. Additionally, the OFAT approach is less efficient than other experimental designs when there are many factors that need to be tested - running separate experiments for each factor can be time-consuming, and in most cases, expensive.

7.2. Modern design of experiments

A major aspect of MDOE is that it prioritises the development of accurate prediction models over the collection of large amounts of data [15]. Compared to OFAT approach, MDOE is a more comprehensive and sophisticated experimental design strategy that can account for complex interactions between multiple factors [22]. It uses a systematic approach to experimental design where researchers vary multiple factors simultaneously at different levels and evaluate the effect of each combination on the response variable, in turn capturing interaction effects. Through the use of advanced statistical techniques, such as response surface modelling (RSM) and optimisation algorithms, MDOE provides a framework for researchers to determine the optimal combination of variables to be tested for their required level of accuracy.

To keep this chapter concise, the focus will be kept on RSM. RSM comprises a set of mathematical and statistical tools that are valuable for the modelling and analysis of problems in which multiple variables influence a response of interest. The fundamental aim of RSM is to optimise this response, such that it is representative of the true results. This requires *a priori* knowledge of the expected results - once the expected response surface is known, combinations of design variables can be probed to build the surface.

7.3. Expected aerodynamic behaviour of the Flying V

In this section, the expected mathematical shape of the response function is discussed. The proposed investigation aims to obtain a separate response surface for the aerodynamic performance (L/D), pitching moment (C_m), and yawing moment (C_n) of the Flying V for any given combination of angle of attack (α) and sideslip (β), within the specified bounds. Each of these three surfaces will be constructed for three distinct cases: full-scale in free-air; ≈2% scale in free-air; and finally ≈2% scale inside the wind tunnel. To build the response surfaces for these variables, their topology must be identified. To do so, previous investigations into the Flying V will be used as a guide when possible. The topology of each response surface is different, and requires careful consideration to avoid misfitting the data.

The aerodynamic performance of the Flying V is well understood from previous investigations and features a similar topology to other slender wings. Namely, the lift is expected to increase linearly with angle of attack up until a given stall angle of attack, after which it will decrease. The exact shape of the stall in the lift curve will determine the required function for the response surface, since this regime exhibits the strongest non-linearity. Drag is expected to increase quadratically with angle of attack, and pitching moment should be negatively correlated with angle of attack, until a certain stall angle at which point it becomes less negative. Consider the LES simulations carried out on the Flying V, discussed earlier in chapter 2. In this investigation, the lift, drag and pitching moment polars were constructed for various meshes and compared with experimental data. The results are shown in Figure 7.1.

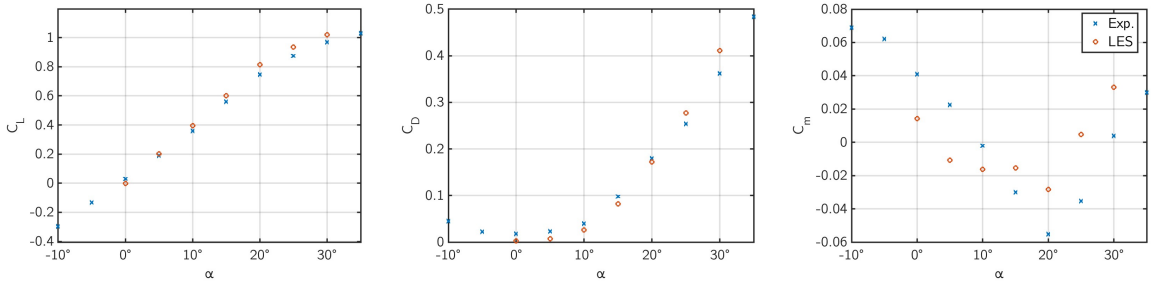

(a) Lift polar **(b)** Drag polar **(c)** Pitching moment polar

Figure 7.1: Comparison of LES results with experimental data for the Flying V [16]

While the discrepancies between the experimental and numerical data can be significant at times, for data fitting this is not a problem since both sets feature the same topology. Figure 7.1a clearly confirms the expected behaviour - the lift coefficient increases linearly until around 20°, at which point a very gentle stall can be observed, with the lift still increasing albeit at a slower rate. Full stall is expected at higher angles of attack, and it is not expected to be abrupt. The drag also follows the expected quadratic behaviour. While the pitching moment cannot be nicely fitted with a polynomial, it is similar enough to motivate the use of a cubic or quadratic curve for an approximate fit. This is a key compromise that is common in RSM - there must be a trade-off between accuracy (how well the surface represents real data) and cost (the number of data points used to build the surface).

7.4. Data-fitting model

From Figure 7.1, it can be seen that the challenge of fitting the numerical data of the Flying V lies with accurately capturing the stall behaviour in the response surfaces, since this introduces strong non-linearities, potentially after very linear behaviour. The lowest order polynomials that can capture the curvature in the response surface caused by stall, are cubic curves. This ensures that the shape of the polars can be modelled to an acceptable level of accuracy. Naturally, higher order polynomials can be used but these require more points, making the experiment more expensive, and they can exhibit Runge's phenomenon, where the fitted polynomial at the edges of an equispaced interval can oscillate wildly [19]. Another issue is that, while the polars may seem to fit a quadratic or cubic curve nicely, it is natural that they are not *exact* polynomials. To overcome this issue, rather than using pure polynomials, a least squares spline approximation can be used. This method attempts to find a spline of best fit for the data, comprised of piecewise polynomials of any given order. In Figure 7.2, a cubic

spline is approximated over the L/D curve, built from a combination of Figure 7.1a and Figure 7.1b. Please note that the data used below is obtained from LES, rather than from experiments.

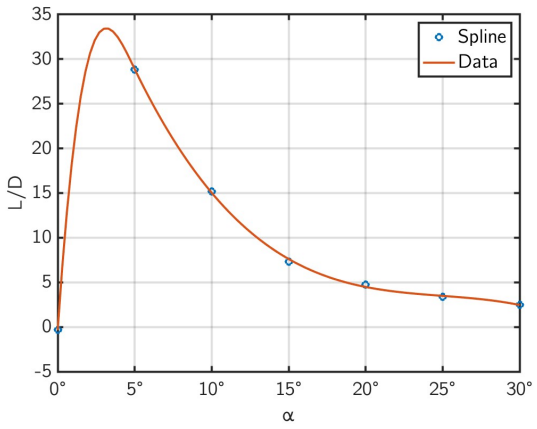

Figure 7.2: Cubic spline approximation of Flying V L/D data

It is clear that there is very good agreement between the spline and the LES data, with sufficient curvature resolution to model the peak and subsequent drop-off. While it does not perfectly fit all of the data points, it finds a best fit for the entire set. Another advantage of this method, is that it can be applied to a two-dimensional case. This 2D surface is referred to as a *least squares bi-cubic spline approximation* (LS-BICSA). To further validate the applicability of this method to the proposed investigation, an LS-BICSA is applied to `XFOIL`[1] data of the lift-to-drag ratio of the NACA 2412 at various combinations of Reynolds number and angle of attack. The results are shown in Figure 7.3.

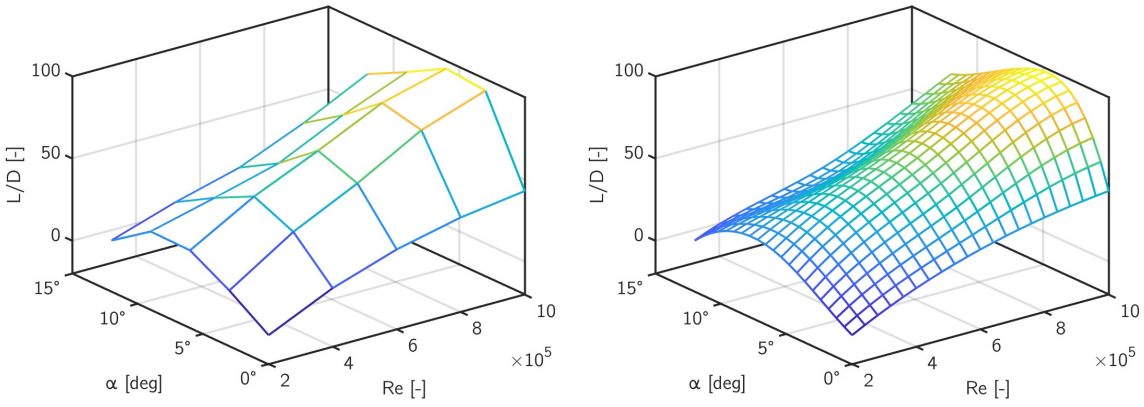

(a) Raw data

(b) Interpolated data

Figure 7.3: Showcase of a bivariate cubic spline approximation applied to the L/D of the NACA2412 at various combinations of angle of attack and Reynolds number

The response surface, shown in Figure 7.3b, nicely represents the raw data, and it is made clear from the figure that the decrease in L/D resulting from the onset of separation or stall, is nicely captured. The effect of Reynolds number, which does not affect L/D linearly, is also captured, with the subtle curvature at $\alpha \approx 10°$ and $Re \approx 5 \times 10^5$ being visible in both Figure 7.3a and Figure 7.3b. Thus, the ability of this tool to sufficiently represent the expected results for the Flying V (i.e.: L/D, C_m, C_n vs. α, β), should not be underestimated.

[1] `https://bit.ly/3JszUSc`, accessed on 20 March 2023

7.5. Previous studies

The article in question, by Cleaver et al. presents an application of MDOE in a CFD environment, with the aim of studying the forces and moments acting on a missile through various speeds and angles of attack - the geometry is shown in Figure 7.4. The researchers utilised a four-factor Latin Hypercube (LH) space-filling design and Gaussian Process (GP) to construct a surrogate model of the Delayed Detached Eddy Simulation (DDES) data. This surrogate model was then employed to characterise missile aerodynamic coefficients across the transonic flight regime. The MDOE process was found to require less computational resources compared to a traditional OFAT approach. To validate the surrogate model, specific OFAT angle of attack sweeps were conducted. This allowed for a direct comparison between the GP model and OFAT analysis. In the majority of cases, the surrogate computer model accurately captured the non-linear response variables. Furthermore, the surrogate model enabled a dynamic prediction tool that could investigate untested scenarios, which is not possible with the OFAT approach [14].

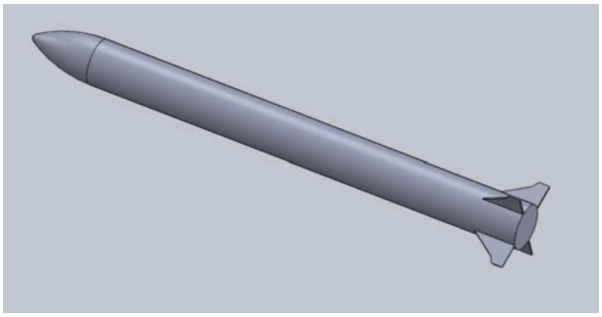

Figure 7.4: Generic air-to-air missile geometry from [14]

Figure 7.5 shows the response surfaces from the investigation for both the lift and drag coefficient. Both curves were built from 23 points. The six OFAT runs used for validation contained 79 points in total and lacked any information about interference effects between variables which, as should be made clear from Figure 7.5, are not negligible and form an important part of the flight envelope which was the target for the researchers.

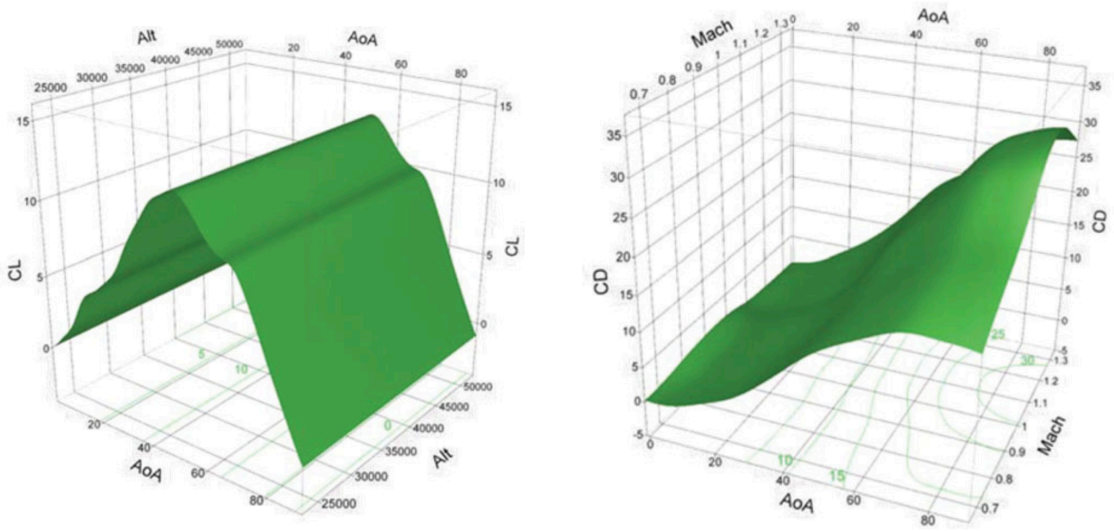

(a) Lift coefficient as a function of angle of attack (in deg) and altitude (in ft) ($Ma = 0.9, \phi = 45°$)

(b) Drag coefficient as a function of angle of attack (in deg) and Mach number ($Alt = 25000ft, \phi = 45°$)

Figure 7.5: Response surfaces for missile aerodynamic characteristics [14]

Overall, the researchers claim that in this application, i.e.: using deterministic computer models, the MDOE approach proved to be beneficial. The LH space-filling design associated with the surrogate

model shows potential for budget and time savings for multi-level, multi-variable problems. While the response surfaces capture much of the curvature associated with non-linear interference effects, they remain to be validated with computational and experimental data, especially in areas of large uncertainty, for instance high angle of attack and Mach number combinations.

In the context of the proposed investigation, the study makes a strong case for potential of response surface modelling. However, the researchers had access to significant computational resources, with the 23 MDOE runs using over 550 000 CPU-hours (vs. $\approx$ 2 000 000 for the OFAT runs). This many points allows for a very detailed response surface; the potential of RSM remains to be seen when the computational resources are significantly reduced, and the only the collection of a few points ($\mathcal{O}(10)$) is possible.

8

Conclusions

This literature review set out to provide an overview and a deeper understanding of the topics required to address the goal of the proposed investigation:

> *"To understand and quantify the influence of wind tunnel testing and Reynolds number effects on the Flying V's performance using a CFD approach."*

The most relevant topics that were identified as crucial for the investigation are listed below. First, it is necessary to understand the context for the future Flying V wind tunnel campaign, as it sets the overarching motivation for the proposed investigation. Secondly, an introduction to the wind tunnel facility is in order. Logically, the next step is to understand how the wind tunnel itself can affect the measurements, with an emphasis on the particular geometry of the Flying V, and how these effects can be corrected or at the very least how they can be anticipated. As Reynolds number effects play an equally important role, this report aims to also document the expected Reynolds number effects on the Flying V, as well as from a more generalised perspective. Since a CFD approach is necessary to predict the flows at the required accuracy, it is important to understand how different codes work, what their limitations are, and how these can be overcome. Finally, the different approaches towards the design of the experiment of the proposed investigation are compared. In this section, the most relevant findings for each of the aforementioned points is summarised to hopefully enlighten the reader on the different aspects of the proposed investigation.

Starting with the Flying V, it was established that at its current development stage, more information is needed with regards to the aerodynamic performance and stability of the aircraft's most recent geometry. This is especially true for the stall regime. An experimental campaign is planned for January 2024 in TU Delft's LTT. A key takeaway is that the wall interference effects of the LTT on a slender wing are not fully understood. Furthermore, the effect of Reynolds number on both the aerodynamic performance and stability of the Flying V is still unknown.

The geometry of the LTT was detailed, with the crucial elements for the numerical modelling also being determined. To minimise any sources of uncertainty, both the contraction tube and diffuser will be simulated alongside the test section. Preliminary RANS simulations also helped identify suitable boundary conditions: a velocity inlet with a value roughly 17 times smaller than what is expected at the test section, a pressure outlet of 0 Pa, and inviscid walls. The choice of the latter was motivated by a NASA report which found that viscous walls had a negligible effect on the solution, while drastically reducing the computational resources.

The concept of wall interference and its corrections was introduced and explored. The classical corrections were documented, and an ideal approach towards minimising these effects was discussed: a test section with flexible walls. In the context of the proposed investigation, this solution is not possible, therefore the best alternative is introduced - numerical corrections. CFD is used to obtain a confined solution and a free-air solution. A direct comparison of the results enables researchers to identify the effect of the walls. Literature is available discussing the expected effects on slender wings and these are

summarised. Namely, the presence of wind tunnel walls leads to a higher concentration of circulation within the vortices, which in turn leads to higher suction and velocities in their core. As these vortices travel downstream they face an adverse pressure gradient, which for the more concentrated vortices is higher, leading them to breakdown. In other words, they abruptly expand and become increasingly chaotic and disorganised. Moreover, with $apriori$ knowledge of the vortex locations and by installing fences at their expected location, the Euler method can offer the same accuracy as RANS.

Following this, the concept of Reynolds number effects was introduced and also explored. Literature was identified documenting these effects on airfoils and moderately swept wings. The most relevant findings were from an investigation on the SACCON configuration. The transonic flow over this aircraft at various Reynolds numbers was studied, spanning from the test Reynolds number of 1.0×10^6 to the full scale Reynolds number of 80×10^6. At higher Reynolds numbers, the flow had a much stronger tendency to remain attached, with separation bubbles forming at moderate values. A separate study investigated the effect of Reynolds number on vortex breakdown. In conclusion, at higher Reynolds numbers vortex breakdown moved upstream, and vortices tended to move outwards and closer to the model surface. The vortices also became less organised, with their intertwining feature becoming less prominent.

Two potential high-fidelity CFD methods were identified: solving the RANS equations with the FVM, or the more novel approach of solving the Lattice Boltzmann equations directly on a Cartesian grid. Since RANS is the more mature method, more literature was available on its limitations in predicting the flow over slender wings. Effectively, non-linear constitutive relations, high quality meshes, and turbulence production limiters should all improve the prediction accuracy of common turbulence models, such as the SST $k - \omega$ or Spalart-Allmaras models in simulating the vortex formation and breakdown over slender wings. If computational cost becomes too high, the Euler equations - an inviscid, compressible form of the full Navier-Stokes equations - may prove to be a worthy alternative, although viscous effects are completely neglected in this method.

The two main approaches for the design of the proposed experiment were identified. These are the OFAT and MDOE approach. MDOE proved to be the superior choice, as it focuses on finding a method to predict the necessary data in a sufficiently accurate fashion, rather than directly calculating or observing this data outright. For situations where obtaining data is expensive or time-consuming, such as the proposed investigation, the MDOE approach is more well suited. An LS-BICSA is suggested as the response surface for the variables of interest which are expected to be the aerodynamic performance, pitching moment and yawing moment. These will be expressed in terms of angle of attack and angle of sideslip. A numerical investigation into the aerodynamic coefficients of a missile in the transonic regime made use of a 23-point response surface. The researchers claimed that the method was able to reproduce the coefficients at an acceptable accuracy at a fraction of the computational cost - 550 000 CPU-hours vs 2 000 000 for the OFAT runs.

Ultimately, this literature report proved to be successful in elucidating the complexity of the topics required to address the proposed research question, and should provide the researchers more confidence in tackling the proposed investigation.

References

[1] Mark Allan, Ken Badcock, and Bryan Richards. “A CFD investigation of wind tunnel wall influences on pitching delta wings”. In: *20th AIAA Applied Aerodynamics Conference*. 2002, p. 2938.

[2] MR Allan et al. “Wind-tunnel interference effects on delta wing aerodynamics computational fluid dynamics investigation”. In: *Journal of aircraft* 42.1 (2005), pp. 189–198.

[3] John David Anderson and John Wendt. *Computational fluid dynamics*. Vol. 206. Springer, 1995.

[4] RK Angell et al. “Summary of the collected data for tests on the NACA 0015, NACA 0018, NACA 0021, NACA 0025 and NACA 0030 aerofoils”. In: (1990).

[5] Nando van Arnhem et al. “Aerodynamic performance of an aircraft equipped with Horizontal Tail mounted propellers”. In: *AIAA Aviation 2019 Forum*. 2019, p. 3036.

[6] Ashwani Assam et al. “An automatic wall treatment for Spalart–Allmaras turbulence model”. In: *Journal of Fluids Engineering* 140.6 (2018).

[7] Chris Baker et al. “Chapter 4 - Computational techniques”. In: *Train Aerodynamics*. Ed. by Chris Baker et al. Butterworth-Heinemann, 2019, pp. 53–71. ISBN: 978-0-12-813310-1. DOI: https://doi.org/10.1016/B978-0-12-813310-1.00004-6. URL: https://www.sciencedirect.com/science/article/pii/B9780128133101000046.

[8] BR Baliga and SV Patankar. “A control volume finite-element method for two-dimensional fluid flow and heat transfer”. In: *Numerical Heat Transfer* 6.3 (1983), pp. 245–261.

[9] Jewel B Barlow, William H Rae, and Alan Pope. *Low-speed wind tunnel testing*. John wiley & sons, 1999.

[10] J Benad and Roelof Vos. “Design of a Flying V Subsonic Transport”. In: *33rd Congress of the International Council of the Aeronautical Sciences*. 2022.

[11] Jiri Blazek. *Computational fluid dynamics: principles and applications*. Butterworth-Heinemann, 2015.

[12] Claudia E Brunner et al. “Study of Reynolds number effects on the aerodynamics of a moderately thick airfoil using a high-pressure wind tunnel”. In: *Experiments in Fluids* 62 (2021), pp. 1–17.

[13] Robert H Bush et al. “Recommendations for future efforts in RANS modeling and simulation”. In: *AIAA scitech 2019 forum*. 2019, p. 0317.

[14] Timothy A Cleaver et al. “Using design of experiments methods for applied computational fluid dynamics: A case study”. In: *Quality Engineering* 28.3 (2016), pp. 280–292.

[15] Richard DeLoach. “The modern design of experiments-A technical and marketing framework”. In: *21st Aerodynamic Measurement Technology and Ground Testing Conference*. 2000, p. 2691.

[16] Jac van Egmond. “Flying V – Half-body CFD analysis (LES)”. In: (Mar. 2019).

[17] BF Ewald. *Wind Tunnel Wall Corrections (la Correction des effets de paroi en soufflerie)*. Tech. rep. Advisory Group for Aerospace Research and Development Neuilly-sur-Seine (France), 1998.

[18] H Fadhila et al. “A new non-linear RANS model with enhanced near-wall treatment of turbulence anisotropy”. In: *Applied Mathematical Modelling* 82 (2020), pp. 293–313.

[19] Bengt Fornberg and Julia Zuev. “The Runge phenomenon and spatially variable shape parameters in RBF interpolation”. In: *Computers & Mathematics with Applications* 54.3 (2007), pp. 379–398.

[20] Henry Clifford Garner et al. *Subsonic wind tunnel wall corrections*. Tech. rep. ADVISORY GROUP FOR AEROSPACE RESEARCH and DEVELOPMENT NEUILLY-SUR-SEINE (FRANCE), 1966.

[21] MI Gerritsma. “Computational Fluid Dynamics: Incompressible Flows”. In: *Script. TU Delft* (2002).

[22] Anthony Giunta, Steven Wojtkiewicz, and Michael Eldred. “Overview of modern design of experiments methods for computational simulations”. In: *41st Aerospace Sciences Meeting and Exhibit*. 2003, p. 649.

[23] Falk Goetten et al. “A review of guidelines and best practices for subsonic aerodynamic simulations using RANS CFD”. In: *Asia-Pacific International Symposium on Aerospace Technology-APSIAT 2019*. 2019.

[24] I Gursul, R Gordnier, and M Visbal. “Unsteady aerodynamics of nonslender delta wings”. In: *Progress in Aerospace Sciences* 41.7 (2005), pp. 515–557.

[25] Jean-Luc Hantrais-Gervois, Jean-François Piat, and Jean-Luc Hantrais. “A Methodology to Derive Wind Tunnel Wall Corrections from RANS Simulations”. In: *Integration* (2012).

[26] Anwar U Haque et al. “Comparison of data correction methods for blockage effects in semispan wing model testing”. In: *EPJ Web of Conferences*. Vol. 114. EDP Sciences. 2016, p. 02129.

[27] SK Hebbar, MF Platzer, and AE Fritzelas. “Reynolds number effects on the vortical-flow structure generated by a double-delta wing”. In: *Experiments in fluids* 28.3 (2000), pp. 206–216.

[28] Charles E Jobe. “Vortex breakdown location over 65 delta wings empiricism and experiment”. In: *The Aeronautical Journal* 108.1087 (2004), pp. 475–482.

[29] Nelson Johnson. “Effect of Winglet Integration and Rudder Deflection on Flying-V Aerodynamic Characteristics”. In: (2021).

[30] Qing Li et al. “Lattice Boltzmann methods for multiphase flow and phase-change heat transfer”. In: *Progress in Energy and Combustion Science* 52 (2016), pp. 62–105.

[31] Peng Lin et al. “Investigation on the Reynolds Number Effect of a Flying Wing Model with Large Sweep Angle and Small Aspect Ratio”. In: *Aerospace* 9.9 (2022), p. 523.

[32] David P Lockard et al. “Evaluation of PowerFLOW for aerodynamic applications”. In: *Journal of statistical physics* 107 (2002), pp. 423–478.

[33] Nikki van Luijk. “Constrained Aerodynamic Shape Optimisation of the Flying V Outer Wing”. In: (2023).

[34] Abdullah Malik and Peter Render. “Use of wall suction in half model wind tunnel testing”. In: *28th AIAA Applied Aerodynamics Conference*. 2010, p. 4828.

[35] Florian R Menter. “Two-equation eddy-viscosity turbulence models for engineering applications”. In: *AIAA journal* 32.8 (1994), pp. 1598–1605.

[36] AA Mohamad. *Lattice boltzmann method*. Vol. 70. Springer, 2011.

[37] Mohamed A Mohamed et al. “Low speed aerodynamic characteristics of non-slender delta wing at low angles of attack”. In: *Alexandria Engineering Journal* 61.12 (2022), pp. 9427–9435.

[38] M Mokry, JR Digney, and RJD Poole. *Analysis of Wind Tunnel Corrections for Half-model Tests of a Transport Aircraft Using a Doublet Panel Method*. National Research Council Canada, 1986.

[39] Douglas C Montgomery. *Design and analysis of experiments*. John wiley & sons, 2017.

[40] Dane M Nelson et al. “Experimental and numerical investigation of flight dynamics of a generic lambda wing configuration”. In: *Aerospace Science and Technology* 71 (2017), pp. 706–724.

[41] Marco Palermo and Roelof Vos. “Experimental aerodynamic analysis of a 4.6%-scale flying-v subsonic transport”. In: *AIAA Scitech 2020 Forum*. 2020, p. 2228.

[42] Ning Qin. “CFD for better understanding of wind tunnel tests”. In: *Integrating CFD and Experiments*. Sheffield. 2003.

[43] Martin Rein and Anthony D Gardner. “Generic lambda wing configuration in compressible flow: effect of highly integrated intakes”. In: *Journal of Aircraft* 52.3 (2015), pp. 972–980.

[44] Stuart Rogers, Karlin Roth, and Steven Nash. “CFD validation of high-lift flows with significant wind-tunnel effects”. In: *18th Applied Aerodynamics Conference*. 2000, p. 4218.

[45] Markus Rütten et al. “Numerical flow investigation of morphing leading edges for the enhancement of maneuverability of unmanned combat air vehicles”. In: *30th AIAA Applied Aerodynamics Conference*. 2012, p. 3326.

[46] Stephane Seror et al. “Implementation and validation of the Spalart-Allmaras turbulence model in parallel environment”. In: *Journal of Aircraft* 42.1 (2005), pp. 179–188.

[47] Philippe Spalart and Steven Allmaras. “A one-equation turbulence model for aerodynamic flows”. In: *30th aerospace sciences meeting and exhibit*. 1992, p. 439.

[48] Philippe R Spalart and Andrey V Garbaruk. “Correction to the Spalart–Allmaras Turbulence Model, Providing More Accurate Skin Friction”. In: *AIAA Journal* 58.5 (2020), pp. 1903–1905.

[49] WA Timmer. “Two-dimensional low-Reynolds number wind tunnel results for airfoil NACA 0018”. In: *Wind engineering* 32.6 (2008), pp. 525–537.

[50] N Ulbrich. “Wind Tunnel Wall Interference Corrections (A Brief Overview)”. In: *Jacobs Technology Inc* (2009).

[51] Sjoerd Van Empelen and Roelof Vos. “Effect of Engine Integration on a 4.6%-Scale Flying-V Subsonic Transport”. In: *AIAA Scitech 2021 Forum*. 2021, p. 0939.

[52] Nick Verhaagen. “Tunnel wall effect on the flow around a 76/40-deg double-delta wing”. In: *36th AIAA Aerospace Sciences Meeting and Exhibit*. 1998, p. 312.

[53] HK Versteeg and W Malalasekera. “The finite volume method”. In: *An Introduction to Computational Fluid Dynamics* (1995), pp. 102–206.

[54] Stephen M Waters et al. “Control allocation performance for blended wing body aircraft and its impact on control surface design”. In: *Aerospace Science and Technology* 29.1 (2013), pp. 18–27.

[55] Stephen WD Wolf. “Adaptive wall technology for improved wind tunnel testing techniques—A review”. In: *Progress in Aerospace Sciences* 31.2 (1995), pp. 85–136.

[56] Shun C Yen and Lung-C Huang. “Reynolds number effects on flow characteristics and aerodynamic performances of a swept-back wing”. In: *Aerospace science and technology* 15.3 (2011), pp. 155–164.

[57] Xuyao Yuan et al. “Lattice Boltzmann model for the low-Mach number variable-density flow”. In: *Physics of Fluids* 34.6 (2022), p. 066112.

A

Flying V geometry

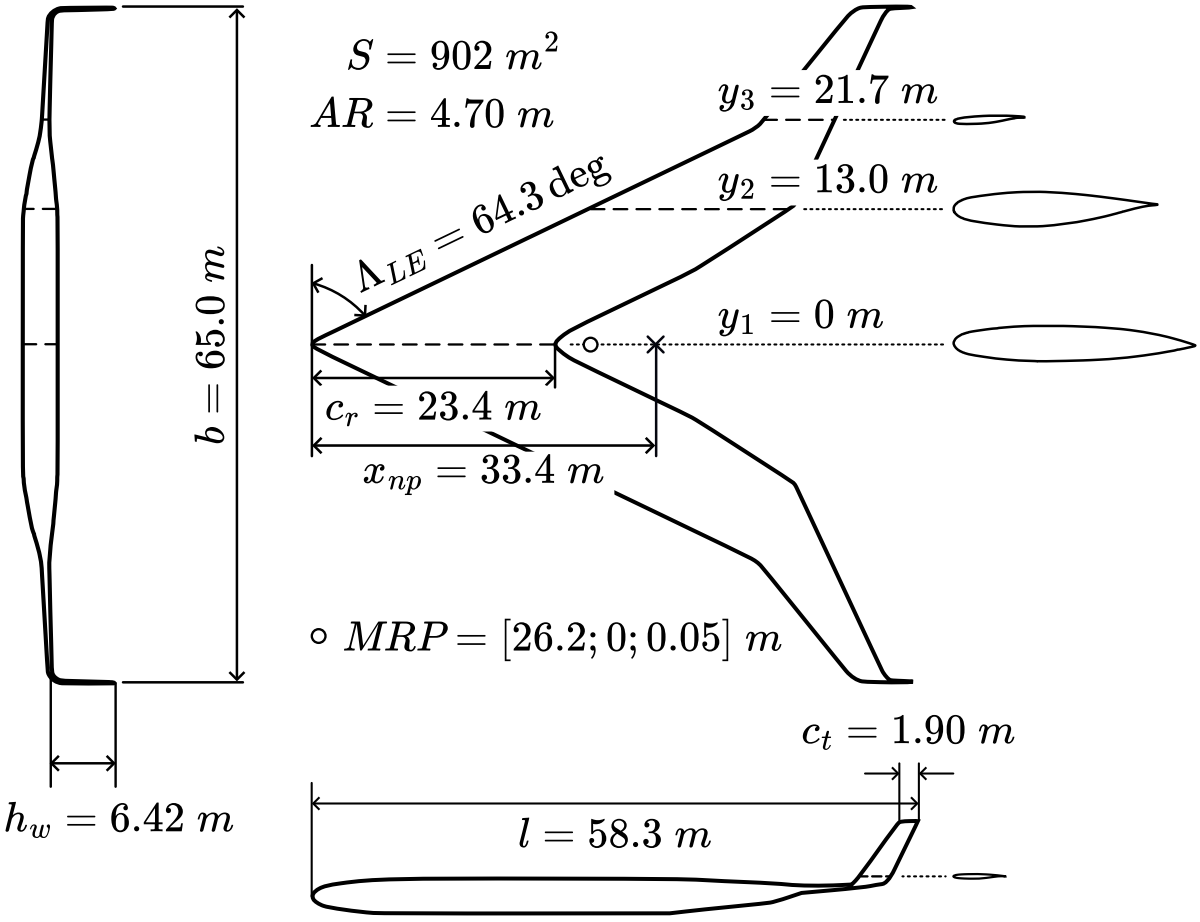

Figure A.1: Technical drawing of the FV1000

B

Supporting work for scientific article

Appendix

A. F19 Validation Data

Table 5. F19 simulation conditions

Variable	Symbol	Value	Units
Density	ρ_∞	1.1698	kg/m^3
Airspeed	V_∞	50.8	m/s
Pressure	p_∞	97 767	Pa
Temperature	T_∞	291.2	K
Dynamic viscosity	μ_∞	18.03×10^{-6}	Pa · s
Reference chord	c_{ref}	0.479	m
Reference area	S_{ref}	0.77	m^2
Reynolds number	Re	1.58×10^6	-
Mach number	M	0.149	-

B. Flying V Meshes

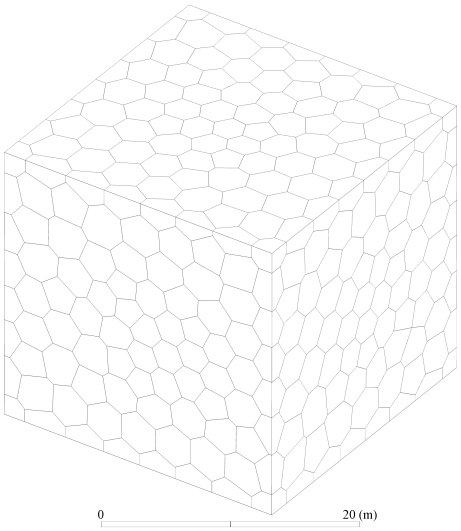

Figure 17. Overview of scaled volume mesh

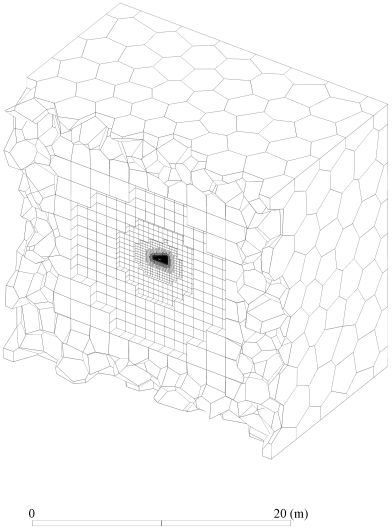

Figure 18. Overview of scaled volume mesh - cut along symmetry plane

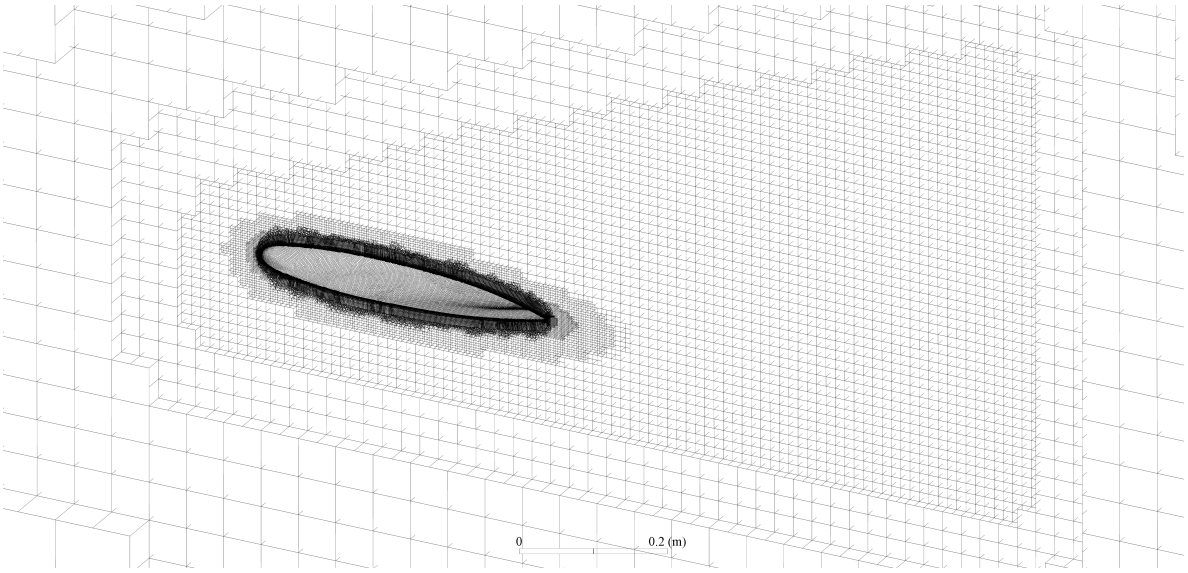

Figure 19. Overview of scaled volume mesh - zoom on body of influence

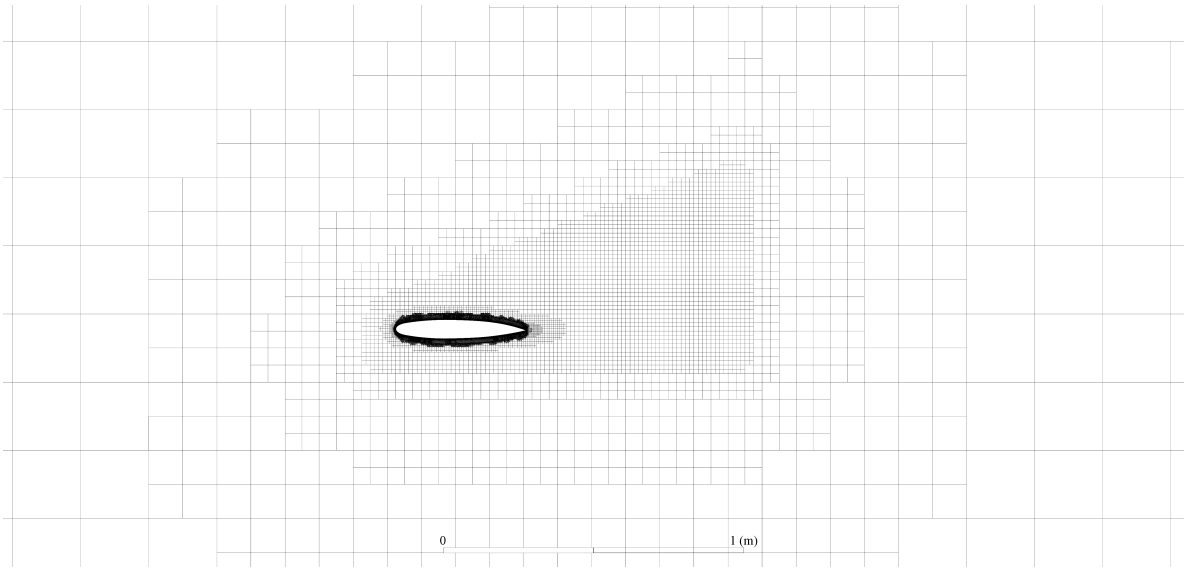

Figure 20. Perpendicular view of scaled volume mesh cut along symmetry plane - far zoom

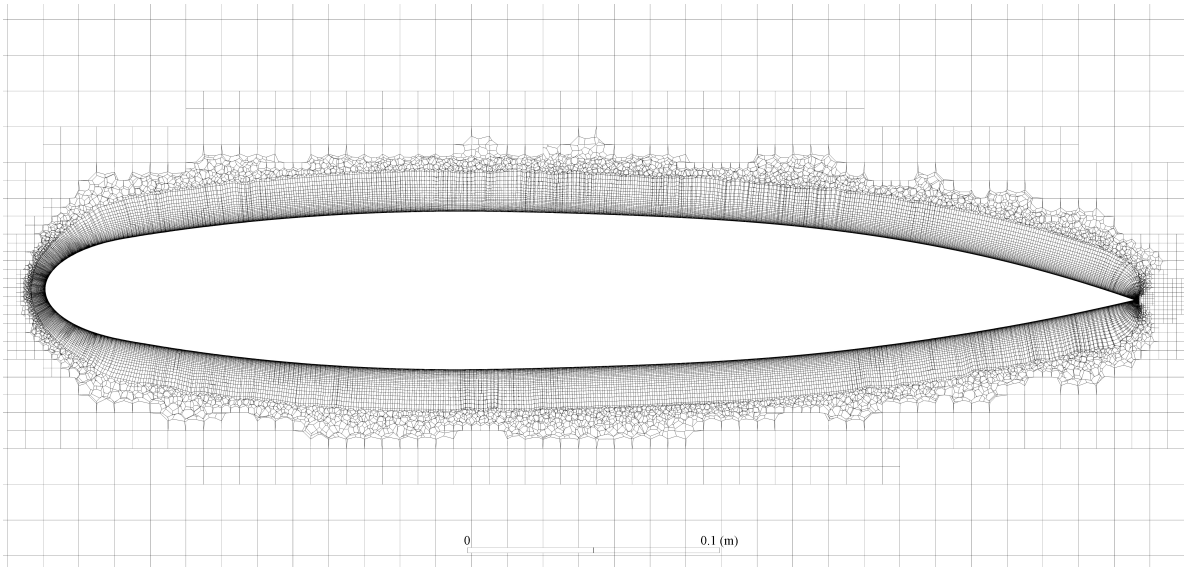

Figure 21. Perpendicular view of scaled volume mesh cut along symmetry plane - close zoom

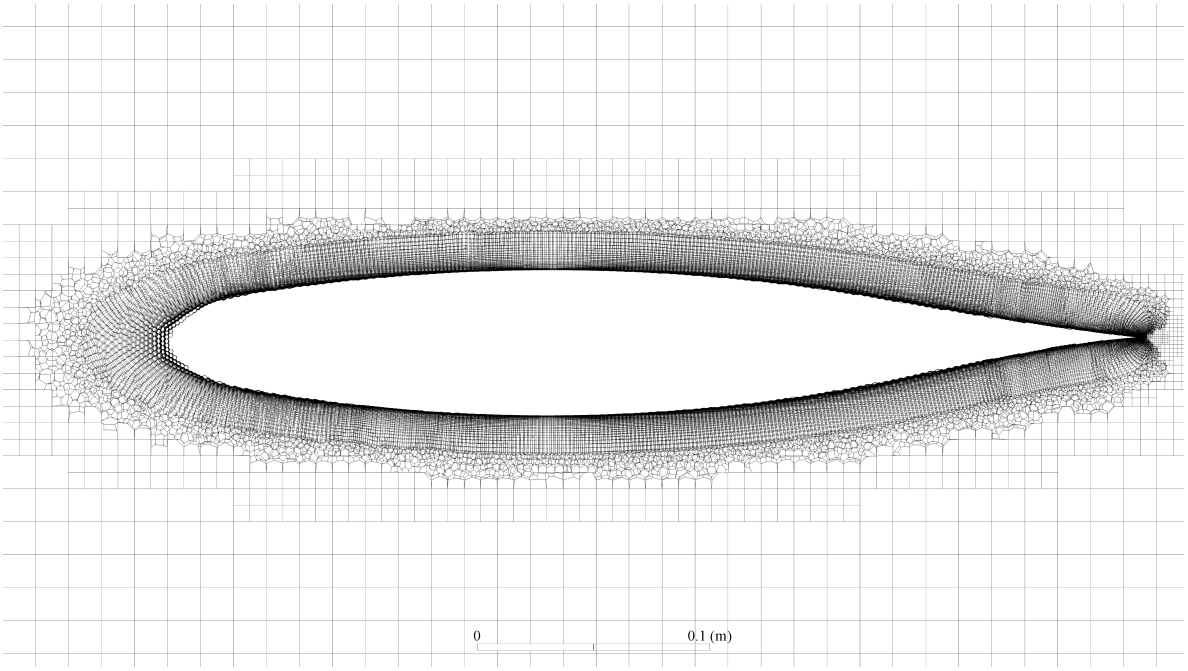

Figure 22. Perpendicular view of scaled volume mesh cut at outer wing - close zoom

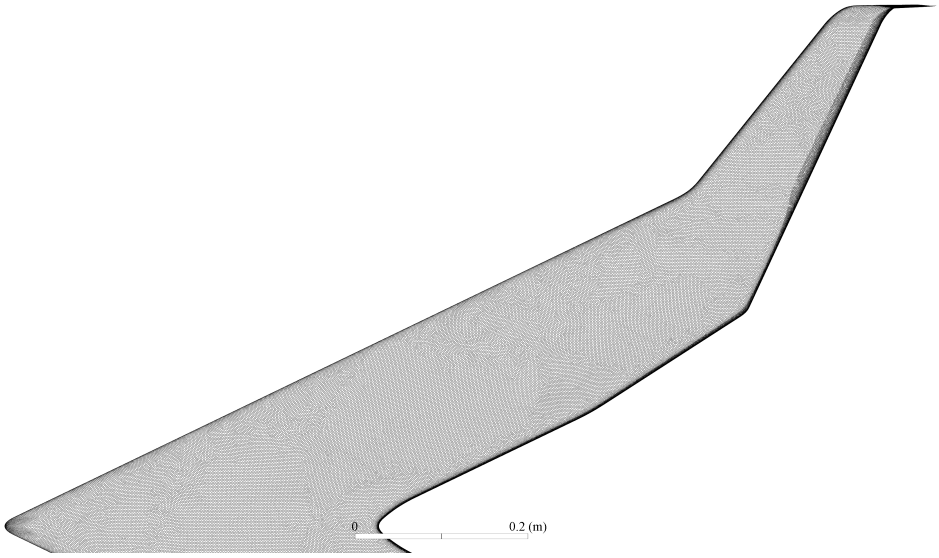

Figure 23. Overview of scaled and wind tunnel surface mesh

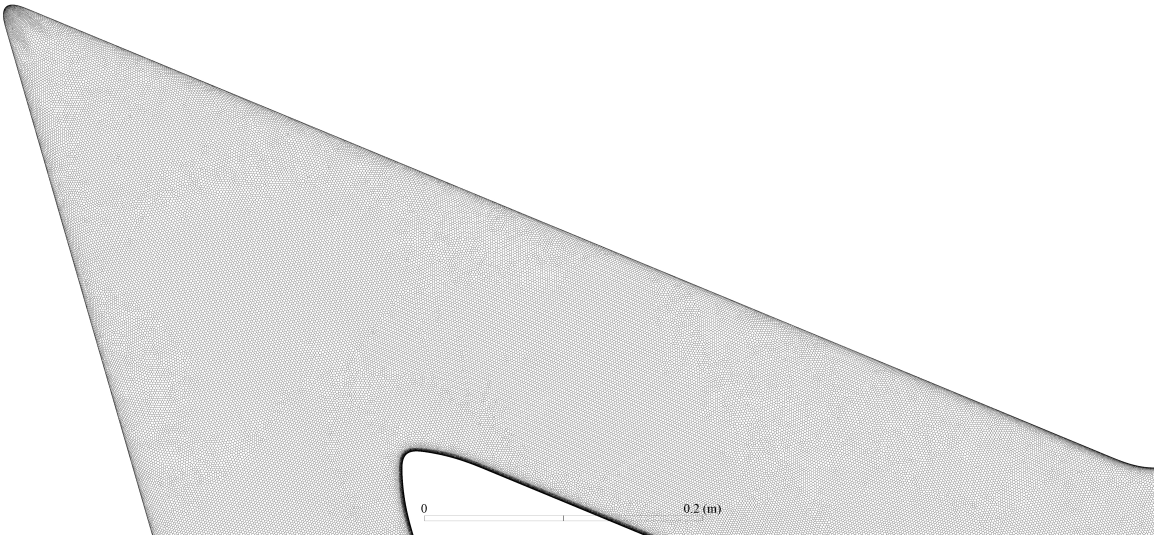

Figure 24. Overview of scaled and wind tunnel surface mesh - zoom on forward section

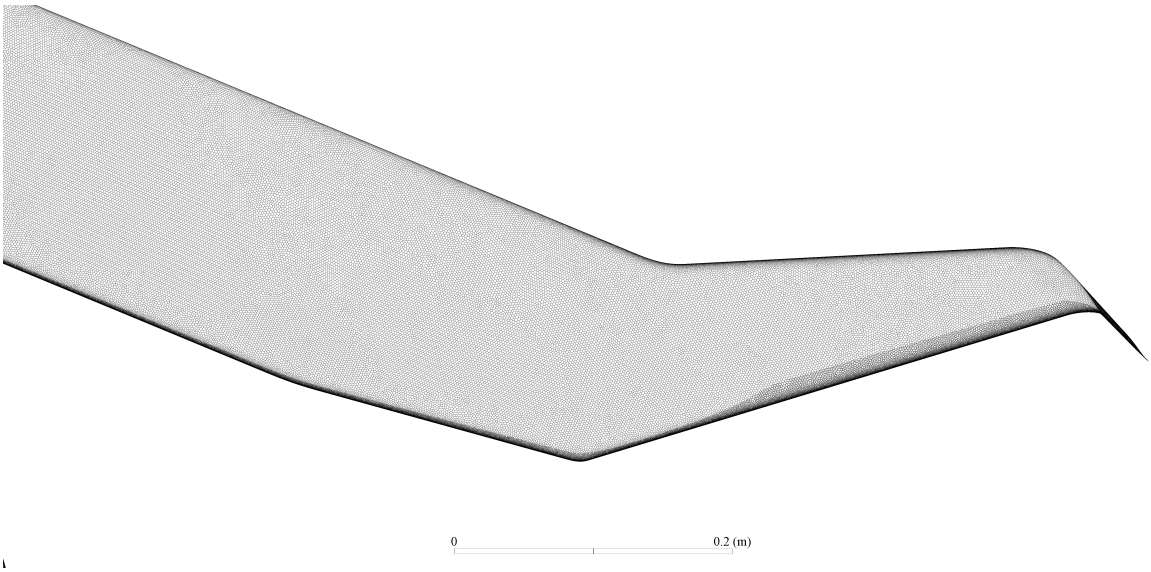

Figure 25. Overview of scaled and wind tunnel surface mesh - zoom on aft section

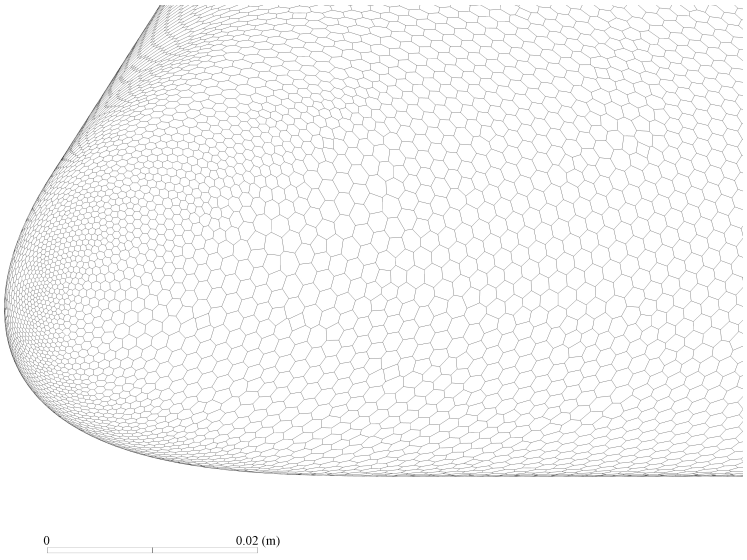

Figure 26. Overview of scaled and wind tunnel surface mesh - zoom on nose

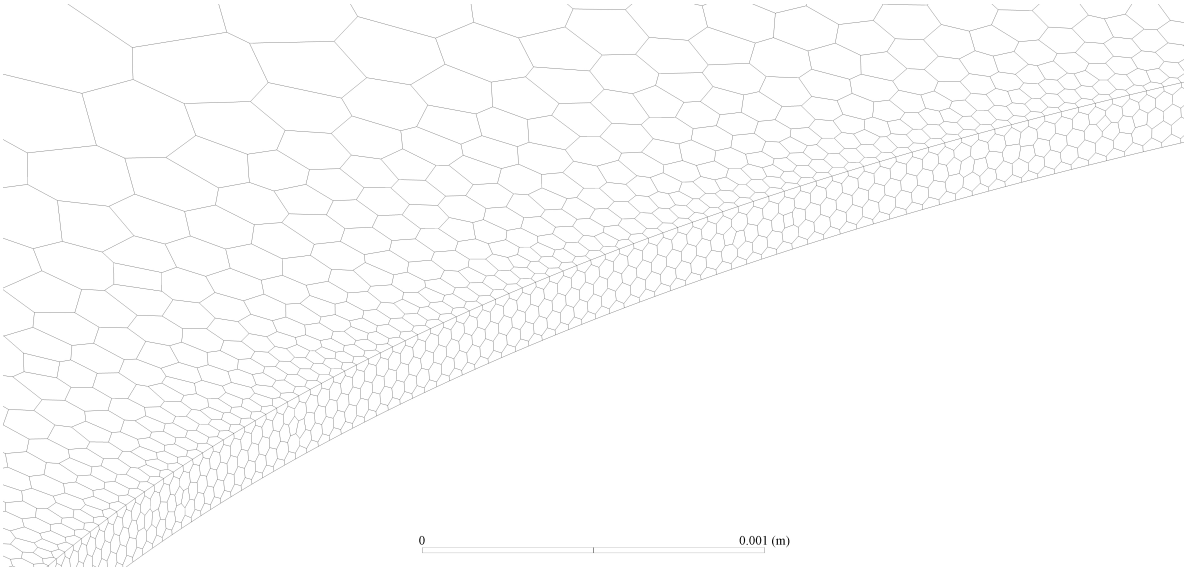

Figure 27. Overview of scaled and wind tunnel surface mesh - zoom on tail

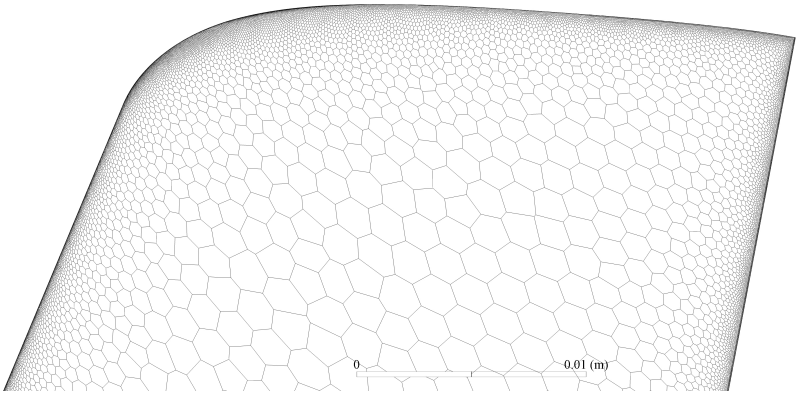

Figure 28. Overview of scaled and wind tunnel surface mesh - zoom on wingtip

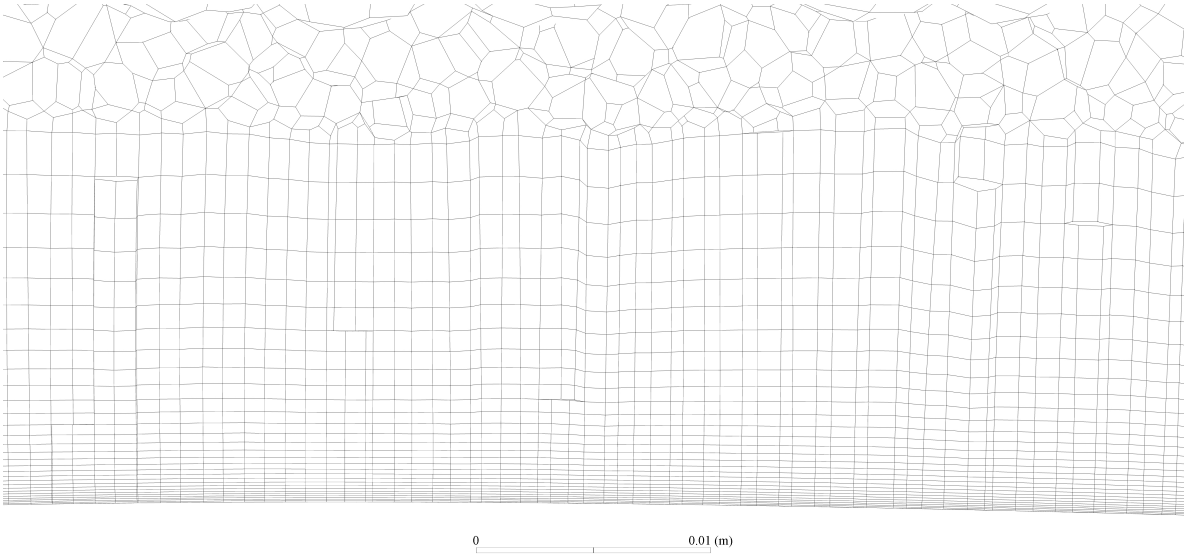

Figure 29. Perpendicular view of scaled mesh inflation layers at centreline

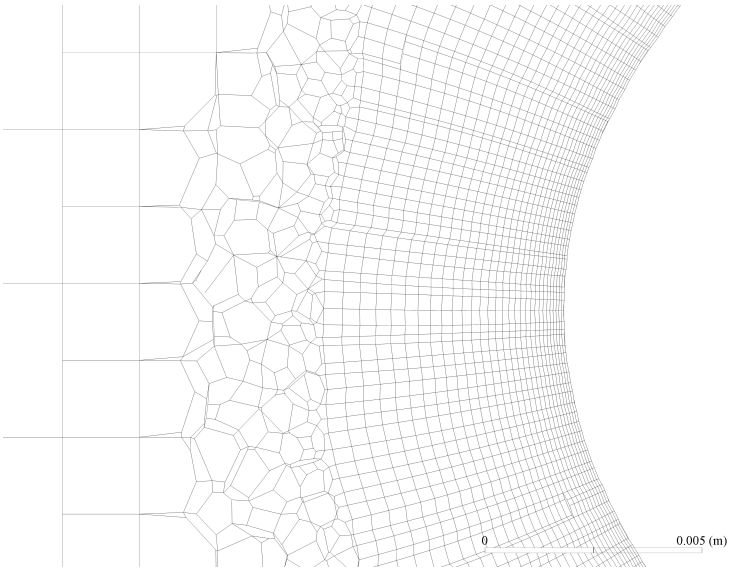

Figure 30. Perpendicular view of scaled mesh inflation layers at centreline - zoom on leading edge

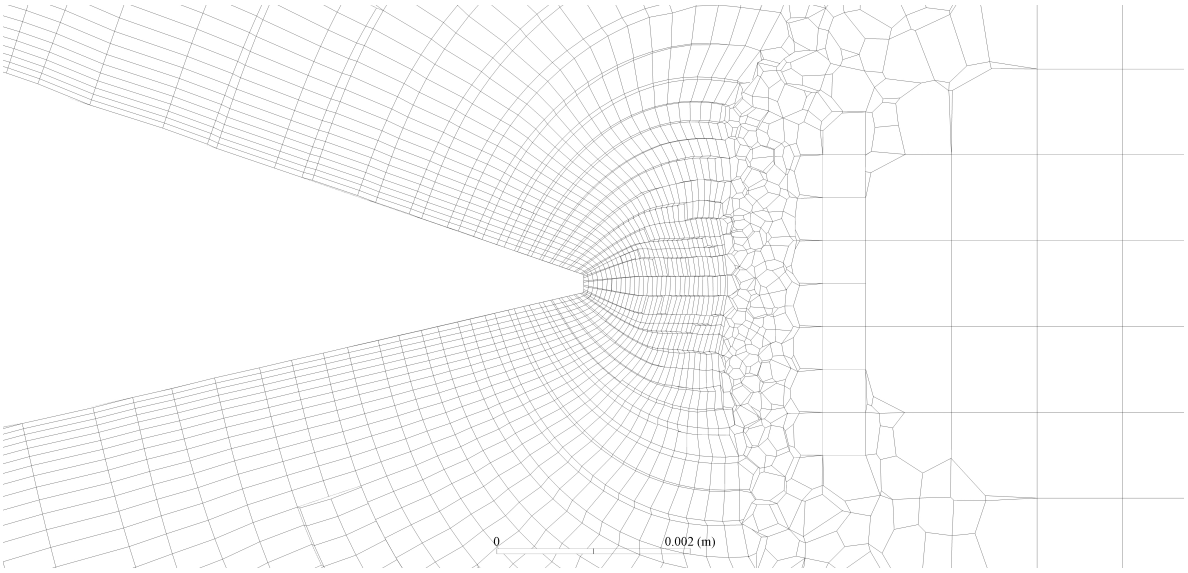

Figure 31. Perpendicular view of scaled mesh inflation layers at centreline - zoom on trailing edge

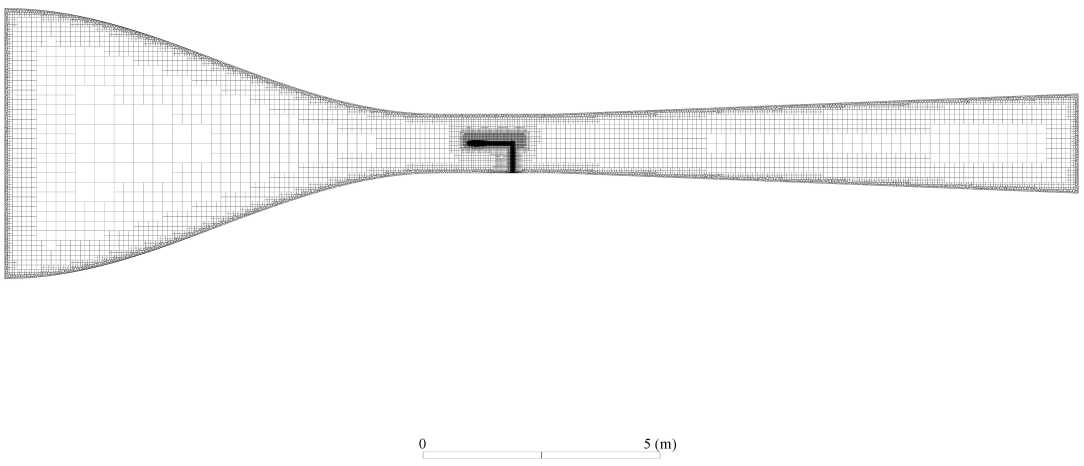

Figure 32. Perpendicular view of wind tunnel volume mesh ($\alpha = 0°, \beta = 0°$) cut along symmetry plane

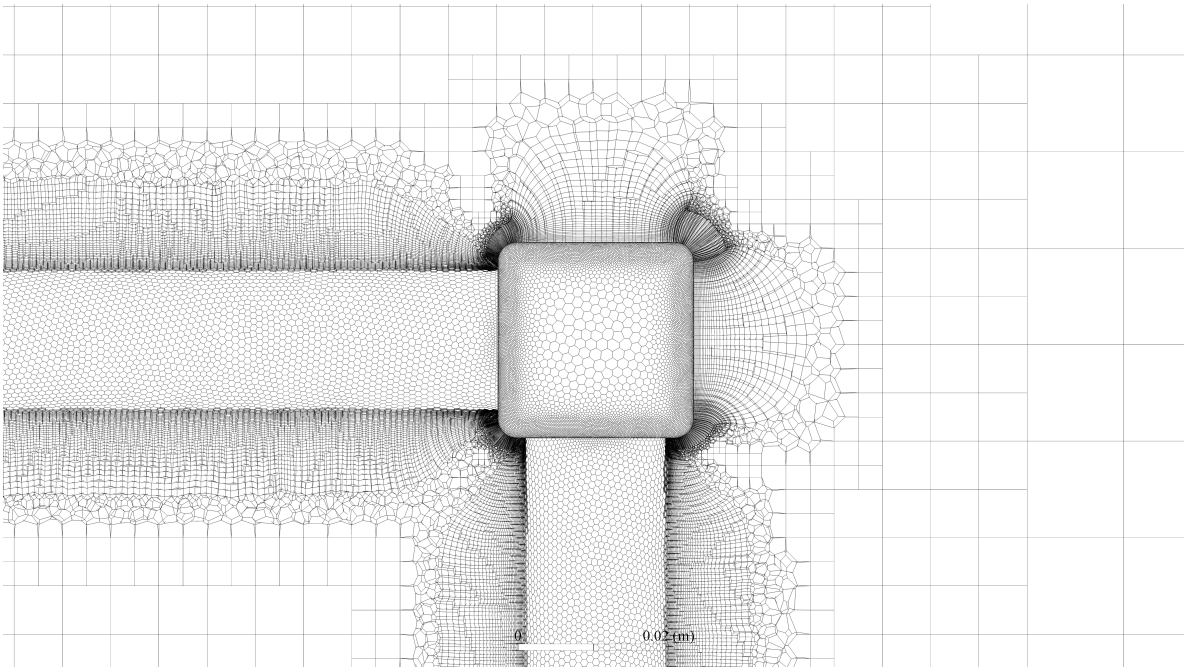

Figure 33. Perpendicular view of wind tunnel volume mesh ($\alpha = 0°, \beta = 0°$) cut along symmetry plane - zoom on aft strut

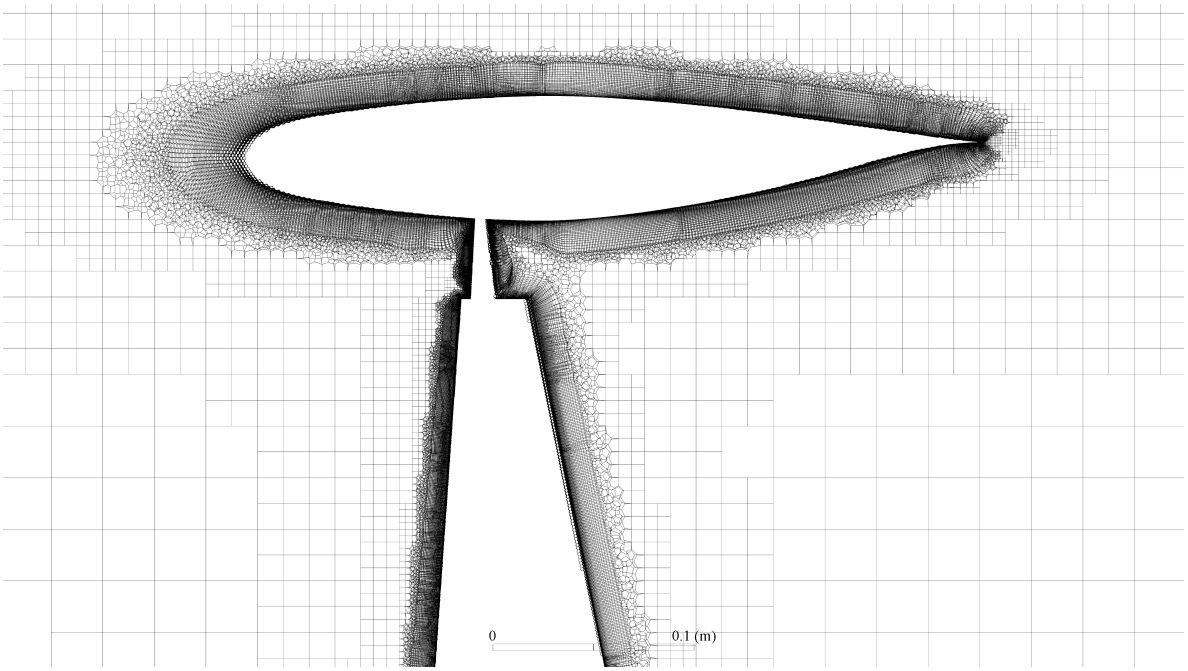

Figure 34. Perpendicular view of wind tunnel volume mesh ($\alpha = 0°, \beta = 0°$) cut along symmetry plane - zoom on upper section of right main strut

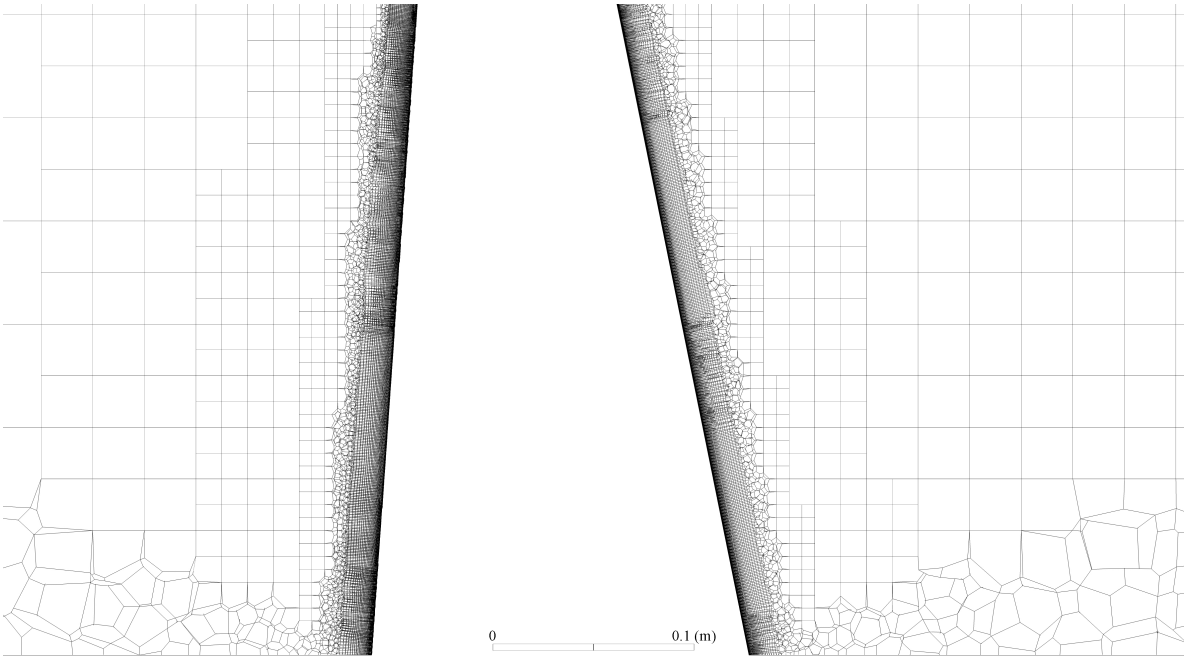

Figure 35. Perpendicular view of wind tunnel volume mesh ($\alpha = 0°, \beta = 0°$) cut along symmetry plane - zoom on lower section of right main strut

C. Force and Moment Polars

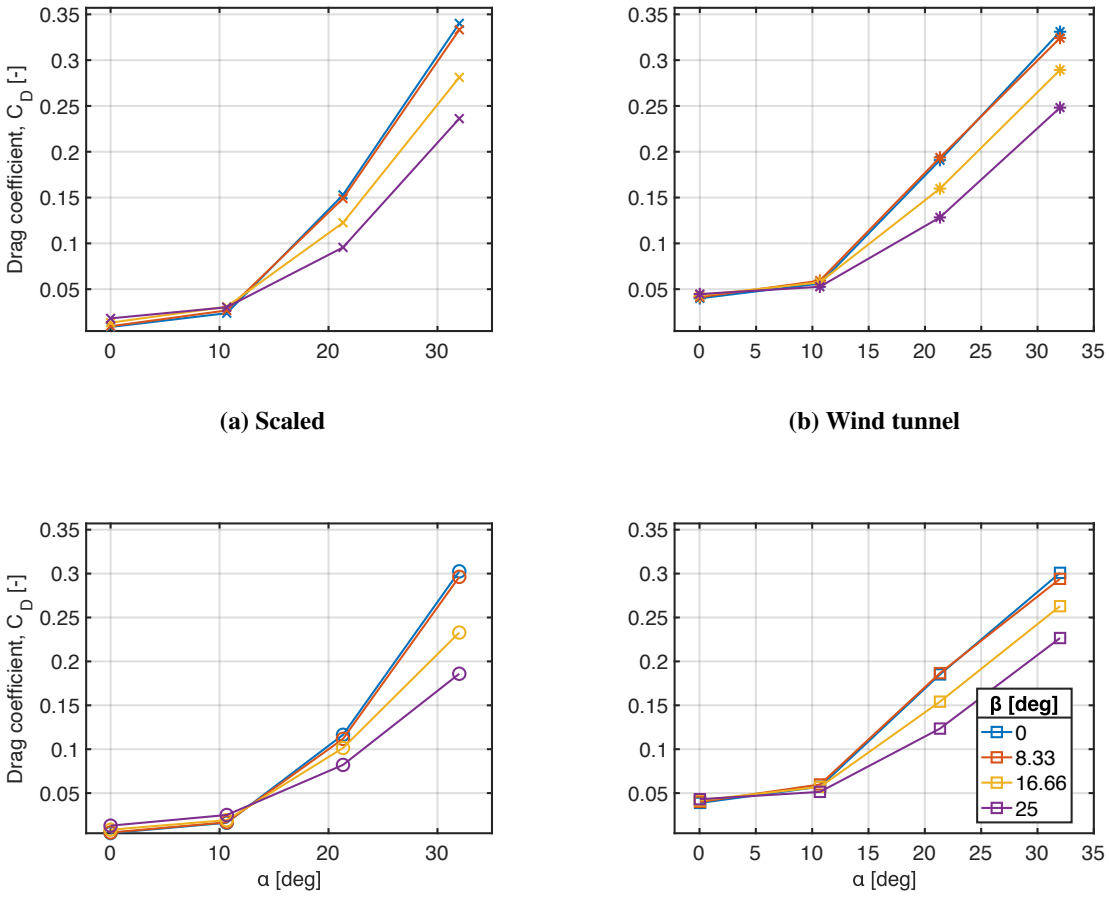

(a) Scaled

(b) Wind tunnel

(c) Full-scale

(d) Wind tunnel (corrected)

Figure 36. Flying V drag coefficient polars

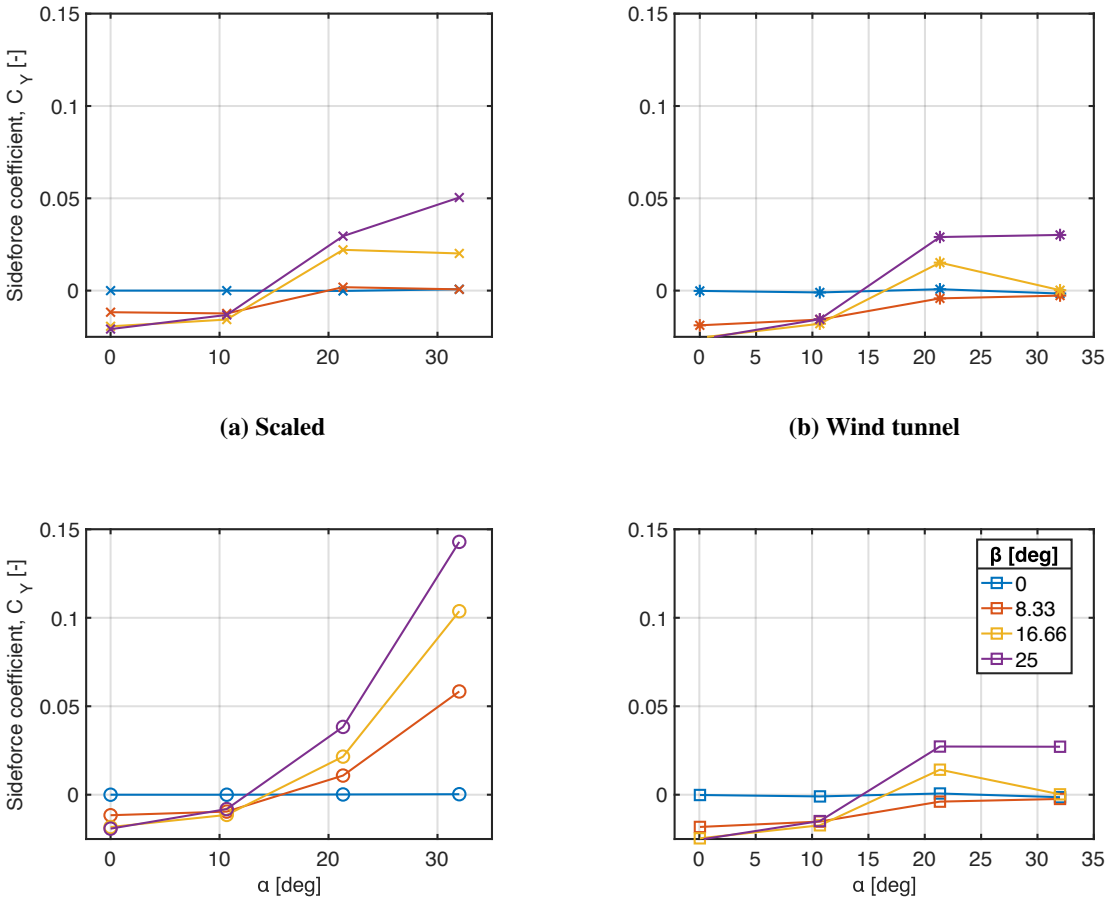

(a) Scaled

(b) Wind tunnel

(c) Full-scale

(d) Wind tunnel (corrected)

Figure 37. Flying V sideforce coefficient polars

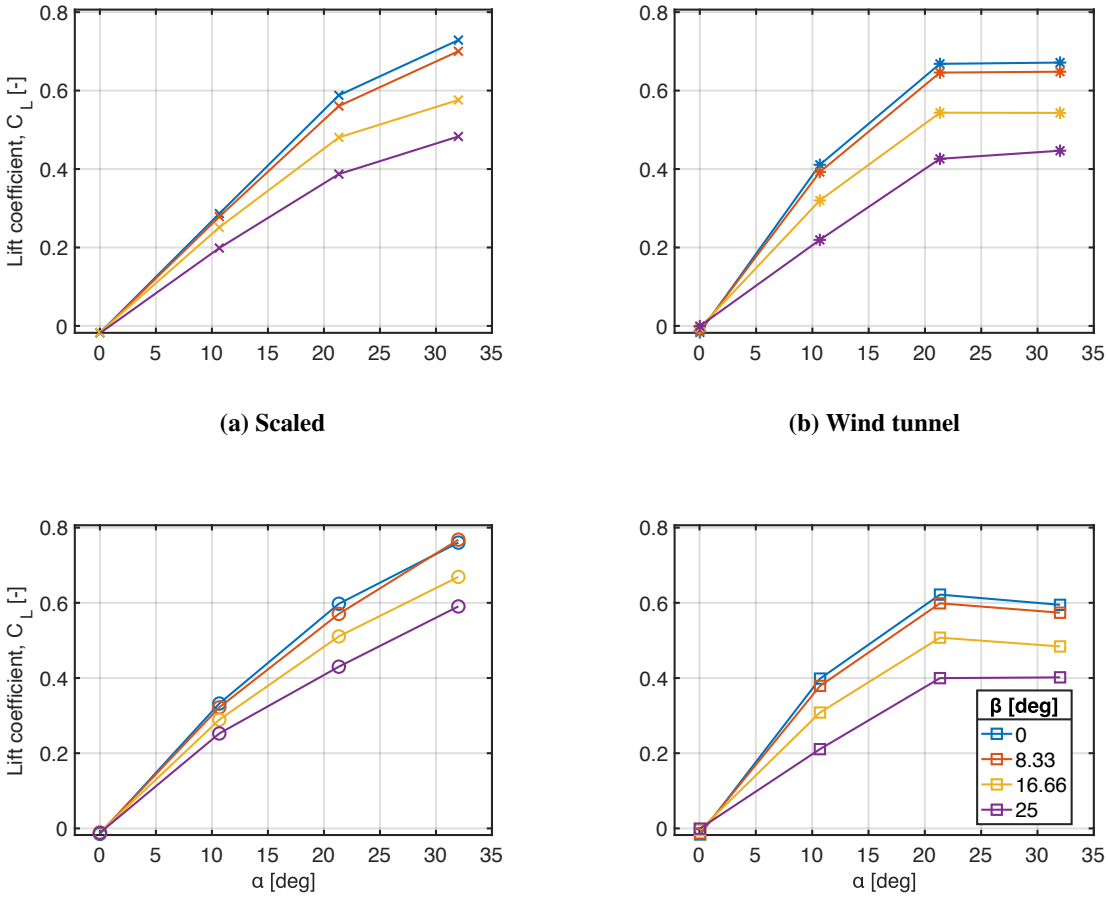

(a) Scaled

(b) Wind tunnel

(c) Full-scale

(d) Wind tunnel (corrected)

Figure 38. Flying V lift coefficient polars

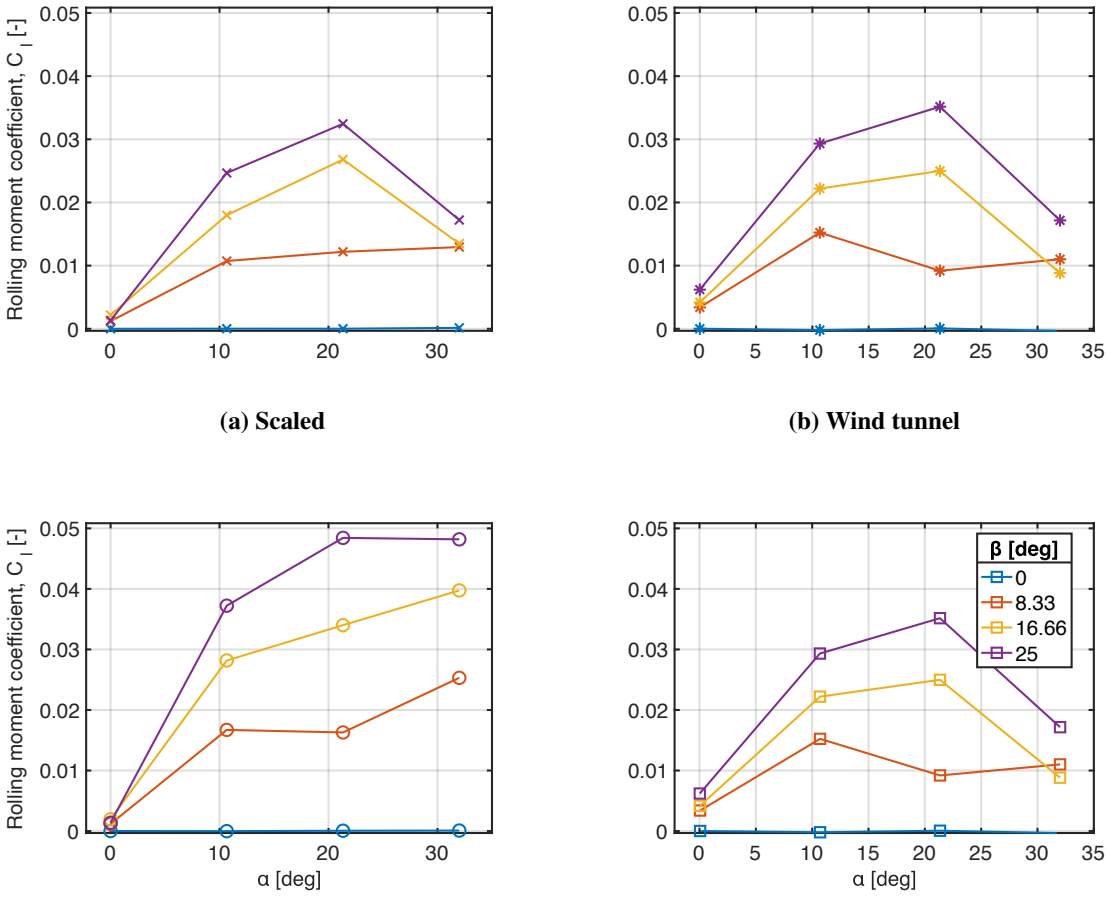

(a) Scaled

(b) Wind tunnel

(c) Full-scale

(d) Wind tunnel (corrected)

Figure 39. Flying V rolling moment coefficient polars

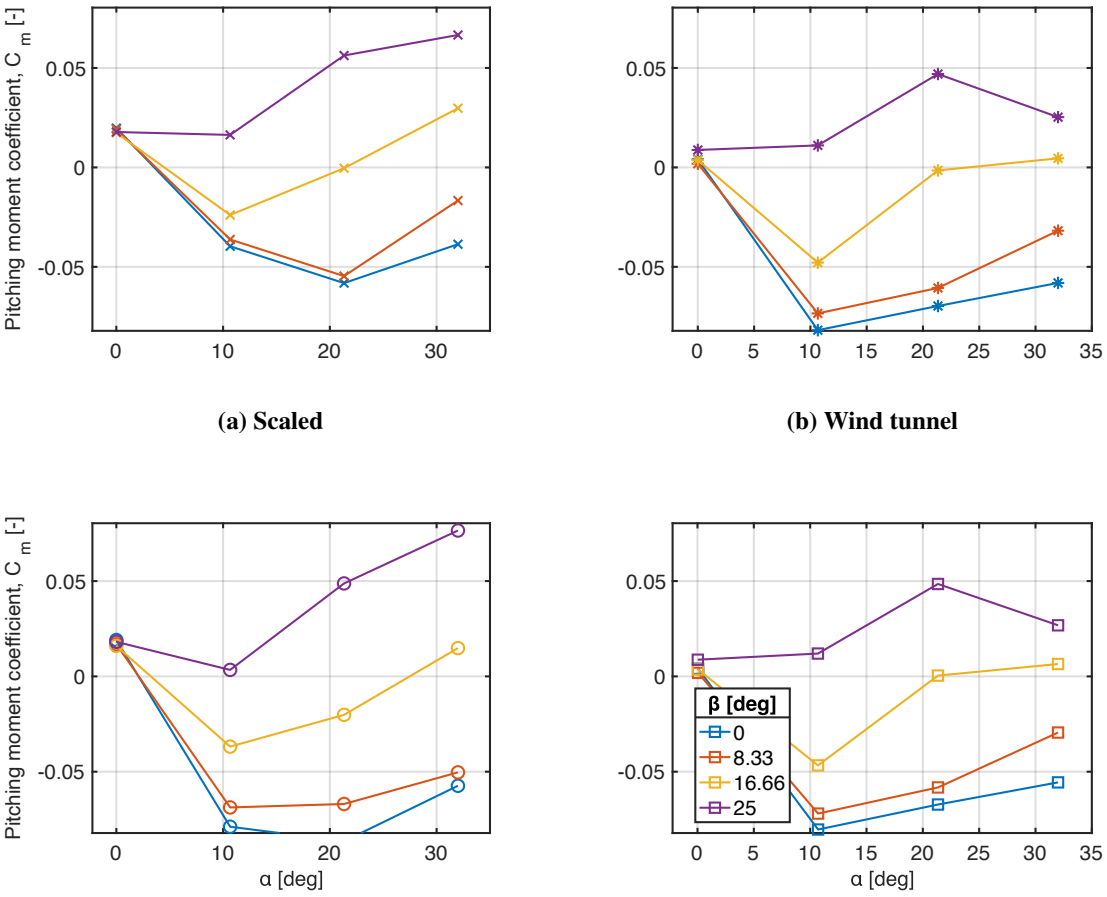

(a) Scaled

(b) Wind tunnel

(c) Full-scale

(d) Wind tunnel (corrected)

Figure 40. Flying V pitching moment coefficient polars

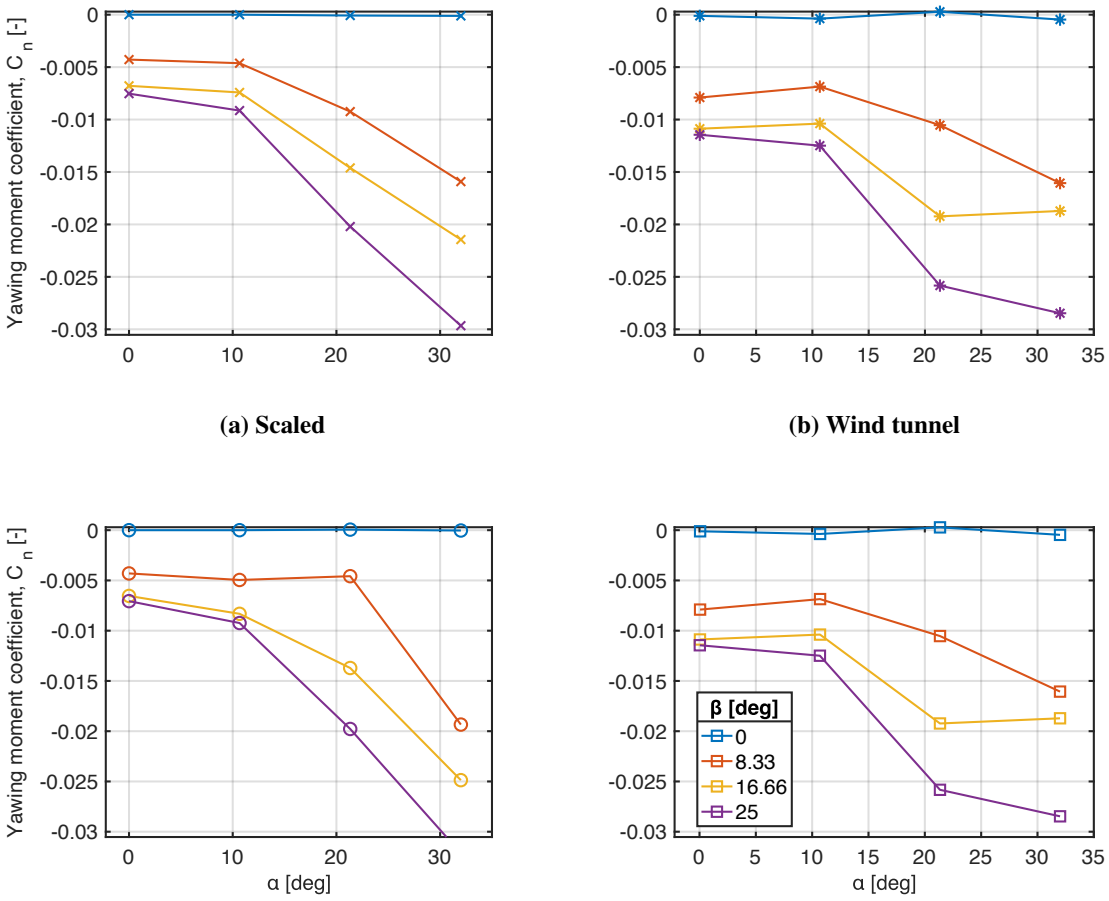

(a) Scaled **(b) Wind tunnel**

(c) Full-scale **(d) Wind tunnel (corrected)**

Figure 41. Flying V yawing moment coefficient polars

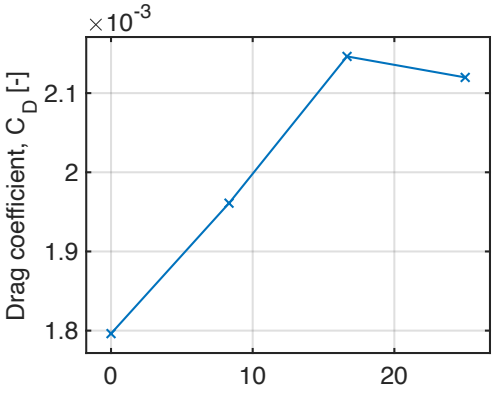

(a) Drag

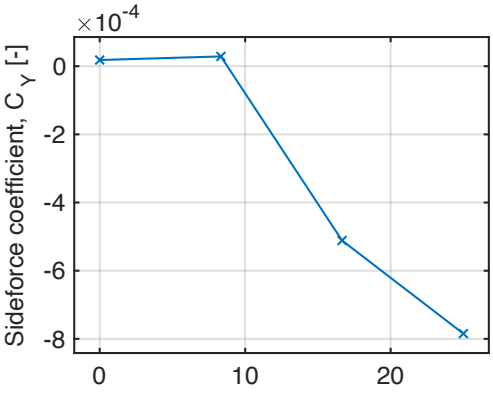

(b) Sideforce

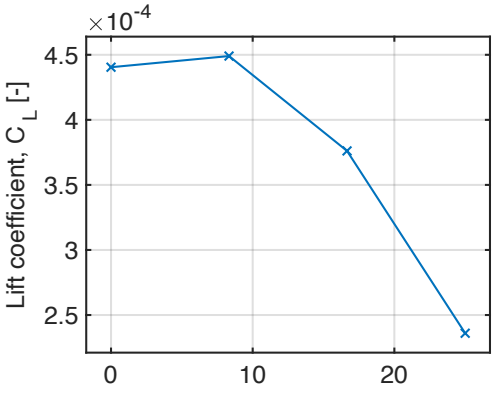

(c) Lift

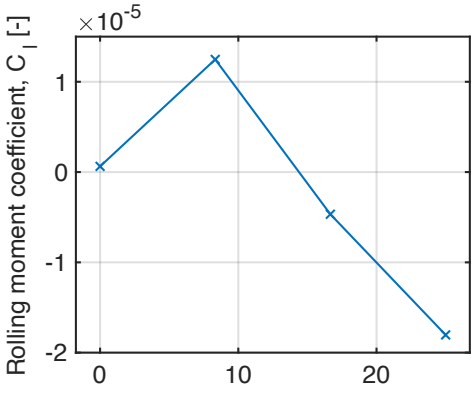

(d) Rolling moment

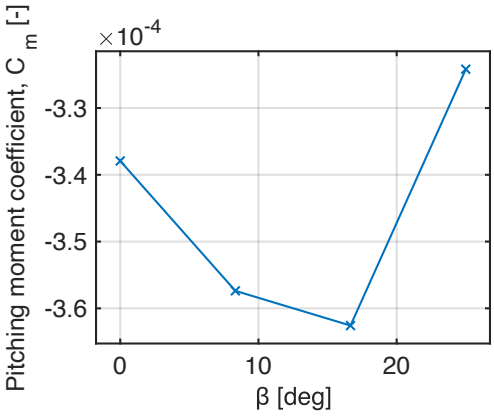

(e) Pitching moment

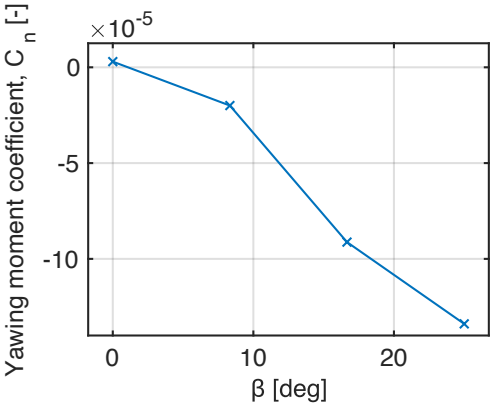

(f) Yawing moment

Figure 42. LTT strut force and moment coefficient polars

Table 6. Scaled Flying V interpolation validation data

Run	Interpolated coefficient					
	Drag	**Sideforce**	**Lift**	**Rolling moment**	**Pitching moment**	**Yawing moment**
1	0.2327	0.0080	0.6321	0.0133	-0.0179	-0.0130
2	0.0088	-0.0029	-0.0179	0.0003	0.0200	-0.0011
3	0.0735	0.0078	0.3650	0.0290	0.0200	-0.0138
4	0.0430	-0.0080	0.3414	0.0101	-0.0368	-0.0039

D. Thin-Plate Spline Coefficients

$$\mathbf{c}\,(\beta,\alpha) = \begin{bmatrix} 0^\circ & 0^\circ \\ 0^\circ & 10.66^\circ \\ 0^\circ & 21.33^\circ \\ 0^\circ & 32^\circ \\ 8.33^\circ & 0^\circ \\ 8.33^\circ & 10.66^\circ \\ 8.33^\circ & 21.33^\circ \\ 8.33^\circ & 32^\circ \\ 16.66^\circ & 0^\circ \\ 16.66^\circ & 10.66^\circ \\ 16.66^\circ & 21.33^\circ \\ 16.66^\circ & 32^\circ \\ 25^\circ & 0^\circ \\ 25^\circ & 10.66^\circ \\ 25^\circ & 21.33^\circ \\ 25^\circ & 32^\circ \end{bmatrix} \tag{11}$$

$$\begin{bmatrix} \mathbf{a}_{scaled} \\ \mathbf{a}_{wind\ tunnel} \\ \mathbf{a}_{full\text{-}scale} \end{bmatrix}^{\mathsf{T}}_{C_D} = \begin{bmatrix} 5.2944\times10^{-5} & 5.0290\times10^{-5} & 3.6956\times10^{-5} \\ -1.0637\times10^{-4} & -1.3080\times10^{-4} & -6.2490\times10^{-5} \\ -4.3421\times10^{-5} & -6.6652\times10^{-7} & -7.8447\times10^{-5} \\ 1.7333\times10^{-5} & 9.2261\times10^{-6} & 2.3648\times10^{-5} \\ 2.7131\times10^{-5} & 3.3990\times10^{-5} & 2.3242\times10^{-5} \\ -2.6936\times10^{-5} & -4.9669\times10^{-5} & 1.2130\times10^{-6} \\ 2.8613\times10^{-5} & 1.0740\times10^{-4} & -4.0007\times10^{-5} \\ 1.1102\times10^{-4} & 2.8045\times10^{-5} & 1.6885\times10^{-4} \\ 4.0157\times10^{-6} & 1.5067\times10^{-5} & 7.4955\times10^{-6} \\ -1.0885\times10^{-5} & -3.6594\times10^{-5} & -3.9519\times10^{-5} \\ -1.4765\times10^{-5} & -1.2169\times10^{-5} & 2.5033\times10^{-5} \\ -1.9501\times10^{-5} & 9.9937\times10^{-6} & -5.8623\times10^{-5} \\ 5.2188\times10^{-5} & 5.1843\times10^{-5} & 4.3261\times10^{-5} \\ -1.6012\times10^{-5} & -4.1470\times10^{-5} & -9.1178\times10^{-6} \\ -5.8726\times10^{-5} & -3.0920\times10^{-5} & -1.9508\times10^{-5} \\ 3.3730\times10^{-6} & -3.5623\times10^{-6} & -2.1991\times10^{-5} \\ -1.6029\times10^{-3} & -1.3001\times10^{-3} & -1.8576\times10^{-3} \\ 8.1568\times10^{-3} & 6.5849\times10^{-3} & 7.1378\times10^{-3} \\ -3.1933\times10^{-1} & -1.8520\times10^{-1} & -2.8673\times10^{-1} \end{bmatrix} \tag{12}$$

$$\begin{bmatrix} \mathbf{a}_{scaled} \\ \mathbf{a}_{wind\ tunnel} \\ \mathbf{a}_{full\text{-}scale} \end{bmatrix}^{\mathsf{T}}_{C_Y} = \begin{bmatrix} 1.0579 \times 10^{-5} & 2.2901 \times 10^{-5} & 3.3635 \times 10^{-5} \\ 1.7823 \times 10^{-5} & 9.6539 \times 10^{-6} & 1.9944 \times 10^{-5} \\ 1.2143 \times 10^{-6} & 1.5508 \times 10^{-5} & 3.9851 \times 10^{-5} \\ 1.2832 \times 10^{-5} & -5.5646 \times 10^{-6} & -9.9037 \times 10^{-5} \\ 1.1140 \times 10^{-6} & -1.9918 \times 10^{-5} & -1.4531 \times 10^{-5} \\ -2.8085 \times 10^{-5} & -2.1446 \times 10^{-5} & -3.0523 \times 10^{-5} \\ -1.3507 \times 10^{-5} & -3.6583 \times 10^{-5} & -1.2421 \times 10^{-5} \\ -3.3051 \times 10^{-5} & 2.5270 \times 10^{-5} & 5.9504 \times 10^{-5} \\ 1.0733 \times 10^{-5} & 1.4466 \times 10^{-5} & 1.0806 \times 10^{-5} \\ -3.0291 \times 10^{-5} & -1.8995 \times 10^{-5} & 2.3176 \times 10^{-5} \\ 8.5630 \times 10^{-5} & 7.6308 \times 10^{-5} & -3.1469 \times 10^{-5} \\ -4.6340 \times 10^{-5} & -9.3883 \times 10^{-5} & 1.0238 \times 10^{-5} \\ 7.0439 \times 10^{-6} & 6.1690 \times 10^{-6} & -1.5472 \times 10^{-6} \\ -4.4551 \times 10^{-5} & -5.7869 \times 10^{-5} & -1.8343 \times 10^{-5} \\ 8.4932 \times 10^{-6} & 5.1246 \times 10^{-5} & -6.9531 \times 10^{-5} \\ 4.0365 \times 10^{-5} & 3.2736 \times 10^{-5} & 8.0247 \times 10^{-5} \\ 4.0803 \times 10^{-4} & 3.2621 \times 10^{-5} & 2.5573 \times 10^{-3} \\ 7.0007 \times 10^{-4} & 3.4995 \times 10^{-4} & 2.5966 \times 10^{-3} \\ -7.5802 \times 10^{-2} & -5.5565 \times 10^{-2} & -1.7439 \times 10^{-1} \end{bmatrix} \tag{13}$$

$$\begin{bmatrix} \mathbf{a}_{scaled} \\ \mathbf{a}_{wind\ tunnel} \\ \mathbf{a}_{full\text{-}scale} \end{bmatrix}^{\mathsf{T}}_{C_L} = \begin{bmatrix} -5.7081 \times 10^{-5} & -1.6920 \times 10^{-4} & -8.5425 \times 10^{-5} \\ -6.0031 \times 10^{-5} & 1.0423 \times 10^{-4} & 5.3275 \times 10^{-5} \\ 1.3553 \times 10^{-4} & 1.5214 \times 10^{-4} & 9.2603 \times 10^{-5} \\ -1.2291 \times 10^{-4} & -1.7355 \times 10^{-4} & -1.6748 \times 10^{-4} \\ -3.0109 \times 10^{-6} & -7.7319 \times 10^{-5} & -2.9924 \times 10^{-5} \\ -2.3543 \times 10^{-5} & 5.3812 \times 10^{-5} & 5.5182 \times 10^{-5} \\ 8.3721 \times 10^{-5} & 1.3298 \times 10^{-4} & -4.8393 \times 10^{-5} \\ 1.7113 \times 10^{-4} & 7.8872 \times 10^{-5} & 2.4913 \times 10^{-4} \\ -4.1926 \times 10^{-5} & -5.9076 \times 10^{-5} & -4.3224 \times 10^{-5} \\ 7.1271 \times 10^{-6} & 1.7086 \times 10^{-5} & -3.5337 \times 10^{-6} \\ 6.7360 \times 10^{-5} & 6.8476 \times 10^{-5} & 5.1222 \times 10^{-5} \\ -1.7566 \times 10^{-4} & -1.4400 \times 10^{-4} & -1.3535 \times 10^{-4} \\ 6.7792 \times 10^{-5} & 1.3951 \times 10^{-4} & 2.6137 \times 10^{-5} \\ -4.4438 \times 10^{-5} & -1.7880 \times 10^{-4} & 7.3989 \times 10^{-5} \\ 5.7805 \times 10^{-5} & 1.5186 \times 10^{-4} & -5.6072 \times 10^{-5} \\ -6.1865 \times 10^{-5} & -9.7013 \times 10^{-5} & -3.2128 \times 10^{-5} \\ -4.1928 \times 10^{-3} & -3.3224 \times 10^{-3} & -2.5735 \times 10^{-3} \\ 1.7830 \times 10^{-2} & 1.5918 \times 10^{-2} & 2.1515 \times 10^{-2} \\ 5.7557 \times 10^{-1} & 1.0830 & 5.3757 \times 10^{-1} \end{bmatrix} \tag{14}$$

$$\begin{bmatrix} \mathbf{a}_{scaled} \\ \mathbf{a}_{wind\ tunnel} \\ \mathbf{a}_{full\text{-}scale} \end{bmatrix}^{\mathsf{T}}_{C_l} = \begin{bmatrix} 1.4102 \times 10^{-5} & 1.4269 \times 10^{-5} & 2.7058 \times 10^{-5} \\ -1.0977 \times 10^{-5} & -2.3357 \times 10^{-5} & -2.1142 \times 10^{-5} \\ -3.0545 \times 10^{-6} & 7.1167 \times 10^{-6} & 7.9771 \times 10^{-6} \\ -1.1637 \times 10^{-5} & -1.2657 \times 10^{-5} & -2.7352 \times 10^{-5} \\ -8.1201 \times 10^{-6} & -5.8847 \times 10^{-6} & -1.5125 \times 10^{-5} \\ 1.3926 \times 10^{-5} & 3.6863 \times 10^{-5} & 2.4486 \times 10^{-5} \\ -1.9016 \times 10^{-5} & -3.8502 \times 10^{-5} & -2.2682 \times 10^{-5} \\ 3.6097 \times 10^{-5} & 4.9319 \times 10^{-5} & 3.3554 \times 10^{-5} \\ 4.5622 \times 10^{-6} & -7.9287 \times 10^{-6} & -7.9779 \times 10^{-7} \\ -1.2839 \times 10^{-5} & -7.9842 \times 10^{-6} & 8.4740 \times 10^{-6} \\ 2.5952 \times 10^{-5} & 2.0558 \times 10^{-5} & -1.3432 \times 10^{-5} \\ -2.8746 \times 10^{-5} & -4.4337 \times 10^{-5} & 5.6579 \times 10^{-6} \\ -2.2881 \times 10^{-5} & -1.8046 \times 10^{-5} & -3.3761 \times 10^{-5} \\ 1.7635 \times 10^{-5} & 1.4303 \times 10^{-5} & 3.0641 \times 10^{-5} \\ 1.7630 \times 10^{-5} & 2.3932 \times 10^{-5} & 1.1073 \times 10^{-5} \\ -1.2632 \times 10^{-5} & -7.6641 \times 10^{-6} & -1.4629 \times 10^{-5} \\ 3.8315 \times 10^{-4} & 5.7555 \times 10^{-4} & 9.8471 \times 10^{-4} \\ 1.7604 \times 10^{-4} & 1.9964 \times 10^{-4} & 8.5723 \times 10^{-4} \\ 6.5520 \times 10^{-2} & 5.9745 \times 10^{-2} & 5.7274 \times 10^{-2} \end{bmatrix} \tag{15}$$

$$\begin{bmatrix} \mathbf{a}_{scaled} \\ \mathbf{a}_{wind\ tunnel} \\ \mathbf{a}_{full\text{-}scale} \end{bmatrix}^{\mathsf{T}}_{C_m} = \begin{bmatrix} 3.9064 \times 10^{-5} & 7.4163 \times 10^{-5} & 8.3145 \times 10^{-5} \\ -3.2925 \times 10^{-5} & -1.1095 \times 10^{-4} & -8.8254 \times 10^{-5} \\ 2.3792 \times 10^{-5} & 7.9886 \times 10^{-5} & -2.3813 \times 10^{-6} \\ 1.2799 \times 10^{-5} & -7.1885 \times 10^{-6} & 7.4149 \times 10^{-5} \\ 1.7817 \times 10^{-5} & 3.0852 \times 10^{-5} & 3.0517 \times 10^{-5} \\ 1.8505 \times 10^{-5} & -2.4742 \times 10^{-5} & -6.4303 \times 10^{-5} \\ -1.0590 \times 10^{-4} & -8.1892 \times 10^{-5} & 3.8681 \times 10^{-5} \\ -1.1096 \times 10^{-5} & 2.1984 \times 10^{-6} & -1.2557 \times 10^{-4} \\ 4.7157 \times 10^{-5} & 6.1065 \times 10^{-5} & 4.2303 \times 10^{-5} \\ -8.8340 \times 10^{-5} & -1.4542 \times 10^{-4} & -2.1616 \times 10^{-5} \\ 3.2460 \times 10^{-5} & 9.3278 \times 10^{-5} & -3.2129 \times 10^{-5} \\ 4.1890 \times 10^{-5} & 3.0501 \times 10^{-5} & 5.2835 \times 10^{-5} \\ -4.1748 \times 10^{-5} & -6.1003 \times 10^{-5} & -4.0879 \times 10^{-5} \\ -6.4191 \times 10^{-6} & 3.3272 \times 10^{-5} & -4.1378 \times 10^{-5} \\ 8.1197 \times 10^{-5} & 8.9272 \times 10^{-5} & 8.1783 \times 10^{-5} \\ -2.8251 \times 10^{-5} & -6.3294 \times 10^{-5} & 1.3099 \times 10^{-5} \\ 1.7684 \times 10^{-3} & 1.3986 \times 10^{-3} & 2.2566 \times 10^{-3} \\ -4.6686 \times 10^{-4} & -2.0422 \times 10^{-3} & -9.1021 \times 10^{-4} \\ -1.9317 \times 10^{-1} & -1.4937 \times 10^{-1} & -3.3117 \times 10^{-1} \end{bmatrix} \tag{16}$$

$$\begin{bmatrix} \mathbf{a}_{scaled} \\ \mathbf{a}_{wind\ tunnel} \\ \mathbf{a}_{full\text{-}scale} \end{bmatrix}^{\mathsf{T}}_{C_n} = \begin{bmatrix} -2.4072 \times 10^{-6} & 3.9663 \times 10^{-6} & -2.5155 \times 10^{-6} \\ -2.5834 \times 10^{-6} & -5.1150 \times 10^{-6} & -1.6760 \times 10^{-7} \\ -1.4932 \times 10^{-7} & 3.4782 \times 10^{-6} & -1.6495 \times 10^{-5} \\ 2.0450 \times 10^{-5} & 1.7591 \times 10^{-5} & 3.2944 \times 10^{-5} \\ -5.1550 \times 10^{-7} & -8.1678 \times 10^{-6} & 4.5218 \times 10^{-7} \\ 3.9815 \times 10^{-6} & 3.4561 \times 10^{-6} & -4.7304 \times 10^{-6} \\ -2.5580 \times 10^{-6} & 3.7870 \times 10^{-6} & 3.2655 \times 10^{-5} \\ -2.9778 \times 10^{-5} & -3.9442 \times 10^{-5} & -4.8769 \times 10^{-5} \\ -7.0993 \times 10^{-6} & -7.8334 \times 10^{-6} & -4.2022 \times 10^{-6} \\ 6.0578 \times 10^{-9} & 6.1204 \times 10^{-6} & -7.0124 \times 10^{-6} \\ 1.8713 \times 10^{-6} & -1.1862 \times 10^{-5} & -4.9806 \times 10^{-6} \\ 1.7033 \times 10^{-5} & 3.4547 \times 10^{-5} & 1.5690 \times 10^{-5} \\ 2.1764 \times 10^{-6} & 2.1925 \times 10^{-6} & 1.6357 \times 10^{-6} \\ 1.3604 \times 10^{-5} & 2.0923 \times 10^{-5} & 1.3835 \times 10^{-5} \\ -5.6517 \times 10^{-6} & -1.6654 \times 10^{-5} & -1.1435 \times 10^{-6} \\ -8.3808 \times 10^{-6} & -6.9867 \times 10^{-6} & -7.1955 \times 10^{-6} \\ -8.2689 \times 10^{-4} & -9.0159 \times 10^{-4} & -8.2862 \times 10^{-4} \\ -2.6639 \times 10^{-4} & -1.4134 \times 10^{-4} & -3.9386 \times 10^{-4} \\ 2.1489 \times 10^{-3} & -1.0597 \times 10^{-2} & 5.4531 \times 10^{-3} \end{bmatrix} \tag{17}$$

E. Surrogate Model for Corrections

$$\begin{bmatrix} \mathbf{a}_{walls} \\ \mathbf{a}_{Re} \end{bmatrix}^{\intercal}_{\Delta C_D} = \begin{bmatrix} 2.6544 \times 10^{-6} & -1.5988 \times 10^{-5} \\ 2.4430 \times 10^{-5} & 4.3880 \times 10^{-5} \\ -4.2755 \times 10^{-5} & -3.5026 \times 10^{-5} \\ 8.1071 \times 10^{-6} & 6.3151 \times 10^{-6} \\ -6.8588 \times 10^{-6} & -3.8892 \times 10^{-6} \\ 2.2733 \times 10^{-5} & 2.8149 \times 10^{-5} \\ -7.8784 \times 10^{-5} & -6.8620 \times 10^{-5} \\ 8.2975 \times 10^{-5} & 5.7835 \times 10^{-5} \\ -1.1051 \times 10^{-5} & 3.4798 \times 10^{-6} \\ 2.5708 \times 10^{-5} & -2.8634 \times 10^{-5} \\ -2.5961 \times 10^{-6} & 3.9798 \times 10^{-5} \\ -2.9495 \times 10^{-5} & -3.9121 \times 10^{-5} \\ 3.4526 \times 10^{-7} & -8.9268 \times 10^{-6} \\ 2.5458 \times 10^{-5} & 6.8944 \times 10^{-6} \\ -2.7806 \times 10^{-5} & 3.9218 \times 10^{-5} \\ 6.9353 \times 10^{-6} & -2.5364 \times 10^{-5} \\ -3.0286 \times 10^{-4} & -2.5470 \times 10^{-4} \\ 1.5719 \times 10^{-3} & -1.0190 \times 10^{-3} \\ -1.3413 \times 10^{-1} & 3.2608 \times 10^{-2} \end{bmatrix} \tag{18}$$

$$\begin{bmatrix} \mathbf{a}_{walls} \\ \mathbf{a}_{Re} \end{bmatrix}^{\mathsf{T}}_{\Delta C_Y} = \begin{bmatrix} -1.2322 \times 10^{-5} & 2.3056 \times 10^{-5} \\ 8.1688 \times 10^{-6} & 2.1217 \times 10^{-6} \\ -1.4294 \times 10^{-5} & 3.8637 \times 10^{-5} \\ 1.8396 \times 10^{-5} & -1.1187 \times 10^{-4} \\ 2.1032 \times 10^{-5} & -1.5645 \times 10^{-5} \\ -6.6390 \times 10^{-6} & -2.4378 \times 10^{-6} \\ 2.3076 \times 10^{-5} & 1.0862 \times 10^{-6} \\ -5.8321 \times 10^{-5} & 9.2555 \times 10^{-5} \\ -3.7339 \times 10^{-6} & 7.3751 \times 10^{-8} \\ -1.1297 \times 10^{-5} & 5.3467 \times 10^{-5} \\ 9.3215 \times 10^{-6} & -1.1710 \times 10^{-4} \\ 4.7543 \times 10^{-5} & 5.6578 \times 10^{-5} \\ 8.7496 \times 10^{-7} & -8.5911 \times 10^{-6} \\ 1.3318 \times 10^{-5} & 2.6208 \times 10^{-5} \\ -4.2753 \times 10^{-5} & -7.8024 \times 10^{-5} \\ 7.6295 \times 10^{-6} & 3.9882 \times 10^{-5} \\ 3.7541 \times 10^{-4} & 2.1493 \times 10^{-3} \\ 3.5012 \times 10^{-4} & 1.8965 \times 10^{-3} \\ -2.0237 \times 10^{-2} & -9.8585 \times 10^{-2} \end{bmatrix} \tag{19}$$

$$\begin{bmatrix} \mathbf{a}_{walls} \\ \mathbf{a}_{Re} \end{bmatrix}^{\mathsf{T}}_{\Delta C_L} = \begin{bmatrix} 1.1212 \times 10^{-4} & -2.8344 \times 10^{-5} \\ -1.6426 \times 10^{-4} & 1.1331 \times 10^{-4} \\ -1.6608 \times 10^{-5} & -4.2924 \times 10^{-5} \\ 5.0649 \times 10^{-5} & -4.4574 \times 10^{-5} \\ 7.4308 \times 10^{-5} & -2.6913 \times 10^{-5} \\ -7.7355 \times 10^{-5} & 7.8725 \times 10^{-5} \\ -4.9256 \times 10^{-5} & -1.3211 \times 10^{-4} \\ 9.2257 \times 10^{-5} & 7.7997 \times 10^{-5} \\ 1.7150 \times 10^{-5} & -1.2983 \times 10^{-6} \\ -9.9590 \times 10^{-6} & -1.0661 \times 10^{-5} \\ -1.1154 \times 10^{-6} & -1.6138 \times 10^{-5} \\ -3.1665 \times 10^{-5} & 4.0307 \times 10^{-5} \\ -7.1714 \times 10^{-5} & -4.1655 \times 10^{-5} \\ 1.3437 \times 10^{-4} & 1.1843 \times 10^{-4} \\ -9.4060 \times 10^{-5} & -1.1388 \times 10^{-4} \\ 3.5148 \times 10^{-5} & 2.9737 \times 10^{-5} \\ -8.7036 \times 10^{-4} & 1.6193 \times 10^{-3} \\ 1.9117 \times 10^{-3} & 3.6856 \times 10^{-3} \\ -5.0742 \times 10^{-1} & -3.8004 \times 10^{-2} \end{bmatrix} \tag{20}$$

$$\begin{bmatrix} \mathbf{a}_{walls} \\ \mathbf{a}_{Re} \end{bmatrix}^{\mathsf{T}}_{\Delta C_l} = \begin{bmatrix} -1.6751 \times 10^{-7} & 1.2957 \times 10^{-5} \\ 1.2379 \times 10^{-5} & -1.0164 \times 10^{-5} \\ -1.0171 \times 10^{-5} & 1.1032 \times 10^{-5} \\ 1.0198 \times 10^{-6} & -1.5715 \times 10^{-5} \\ -2.2353 \times 10^{-6} & -7.0047 \times 10^{-6} \\ -2.2937 \times 10^{-5} & 1.0560 \times 10^{-5} \\ 1.9486 \times 10^{-5} & -3.6655 \times 10^{-6} \\ -1.3222 \times 10^{-5} & -2.5434 \times 10^{-6} \\ 1.2491 \times 10^{-5} & -5.3600 \times 10^{-6} \\ -4.8545 \times 10^{-6} & 2.1313 \times 10^{-5} \\ 5.3932 \times 10^{-6} & -3.9384 \times 10^{-5} \\ 1.5592 \times 10^{-5} & 3.4404 \times 10^{-5} \\ -4.8341 \times 10^{-6} & -1.0880 \times 10^{-5} \\ 3.3311 \times 10^{-6} & 1.3007 \times 10^{-5} \\ -6.3021 \times 10^{-6} & -6.5569 \times 10^{-6} \\ -4.9677 \times 10^{-6} & -1.9976 \times 10^{-6} \\ -1.9240 \times 10^{-4} & 6.0156 \times 10^{-4} \\ -2.3604 \times 10^{-5} & 6.8119 \times 10^{-4} \\ 5.7749 \times 10^{-3} & -8.2463 \times 10^{-3} \end{bmatrix} \tag{21}$$

$$\begin{bmatrix} \mathbf{a}_{walls} \\ \mathbf{a}_{Re} \end{bmatrix}^{\mathsf{T}}_{\Delta C_m} = \begin{bmatrix} -3.5100 \times 10^{-5} & 4.4081 \times 10^{-5} \\ 7.8022 \times 10^{-5} & -5.5329 \times 10^{-5} \\ -5.6094 \times 10^{-5} & -2.6173 \times 10^{-5} \\ 1.9988 \times 10^{-5} & 6.1350 \times 10^{-5} \\ -1.3035 \times 10^{-5} & 1.2699 \times 10^{-5} \\ 4.3247 \times 10^{-5} & -8.2808 \times 10^{-5} \\ -2.4010 \times 10^{-5} & 1.4458 \times 10^{-4} \\ -1.3295 \times 10^{-5} & -1.1447 \times 10^{-4} \\ -1.3908 \times 10^{-5} & -4.8546 \times 10^{-6} \\ 5.7084 \times 10^{-5} & 6.6724 \times 10^{-5} \\ -6.0817 \times 10^{-5} & -6.4589 \times 10^{-5} \\ 1.1389 \times 10^{-5} & 1.0945 \times 10^{-5} \\ 1.9254 \times 10^{-5} & 8.6979 \times 10^{-7} \\ -3.9691 \times 10^{-5} & -3.4959 \times 10^{-5} \\ -8.0756 \times 10^{-6} & 5.8617 \times 10^{-7} \\ 3.5043 \times 10^{-5} & 4.1350 \times 10^{-5} \\ 3.6975 \times 10^{-4} & 4.8822 \times 10^{-4} \\ 1.5753 \times 10^{-3} & -4.4335 \times 10^{-4} \\ -4.3793 \times 10^{-2} & -1.3800 \times 10^{-1} \end{bmatrix} \tag{22}$$

$$\begin{bmatrix} \mathbf{a}_{walls} \\ \mathbf{a}_{Re} \end{bmatrix}^{\mathsf{T}}_{\Delta C_n} = \begin{bmatrix} -6.3735 \times 10^{-6} & -1.0830 \times 10^{-7} \\ 2.5316 \times 10^{-6} & 2.4158 \times 10^{-6} \\ -3.6275 \times 10^{-6} & -1.6345 \times 10^{-5} \\ 2.8593 \times 10^{-6} & 1.2494 \times 10^{-5} \\ 7.6523 \times 10^{-6} & 9.6768 \times 10^{-7} \\ 5.2538 \times 10^{-7} & -8.7119 \times 10^{-6} \\ -6.3450 \times 10^{-6} & 3.5213 \times 10^{-5} \\ 9.6640 \times 10^{-6} & -1.8991 \times 10^{-5} \\ 7.3405 \times 10^{-7} & 2.8971 \times 10^{-6} \\ -6.1144 \times 10^{-6} & -7.0185 \times 10^{-6} \\ 1.3733 \times 10^{-5} & -6.8519 \times 10^{-6} \\ -1.7513 \times 10^{-5} & -1.3434 \times 10^{-6} \\ -1.6142 \times 10^{-8} & -5.4068 \times 10^{-7} \\ -7.3185 \times 10^{-6} & 2.3022 \times 10^{-7} \\ 1.1003 \times 10^{-5} & 4.5082 \times 10^{-6} \\ -1.3942 \times 10^{-6} & 1.1853 \times 10^{-6} \\ 7.4706 \times 10^{-5} & -1.7317 \times 10^{-6} \\ -1.2505 \times 10^{-4} & -1.2747 \times 10^{-4} \\ 1.2746 \times 10^{-2} & 3.3042 \times 10^{-3} \end{bmatrix} \tag{23}$$

F. Pressure Coefficient Contours and Streamlines

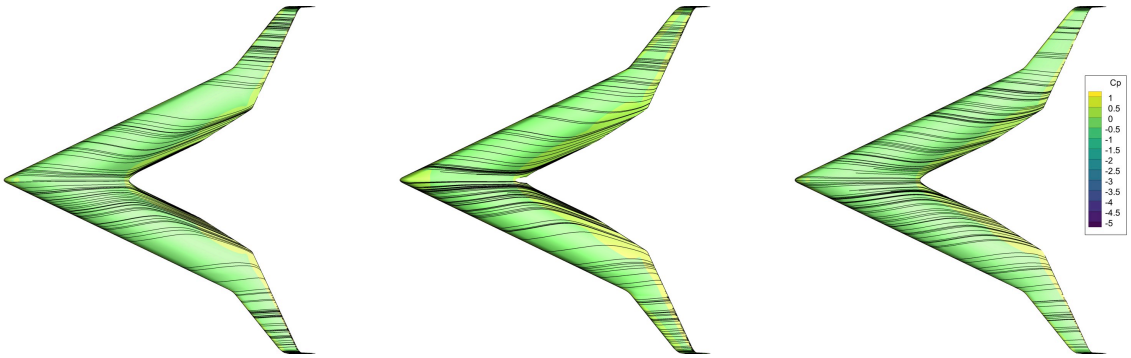

(a) Scaled **(b) Wind tunnel** **(c) Full-scale**

Figure 43. Flying V pressure coefficient contours and surface streamlines ($\alpha = 0°, \beta = 0°$)

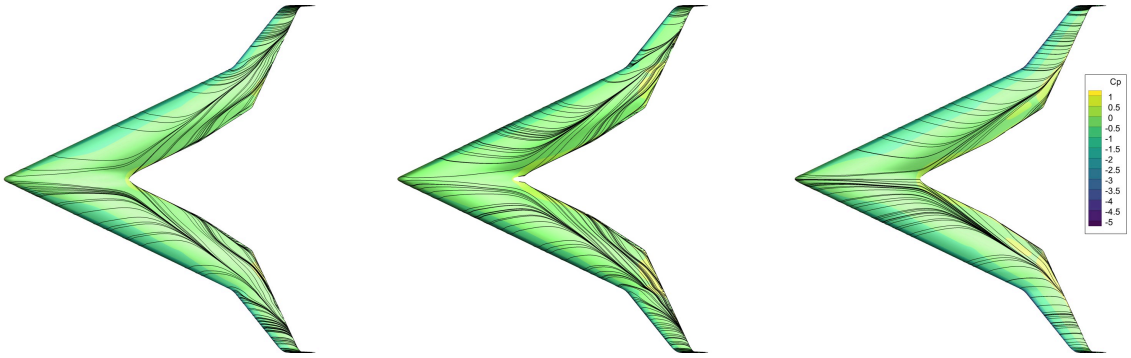

(a) Scaled **(b) Wind tunnel** **(c) Full-scale**

Figure 44. Flying V pressure coefficient contours and surface streamlines ($\alpha = 10.66°, \beta = 0°$)

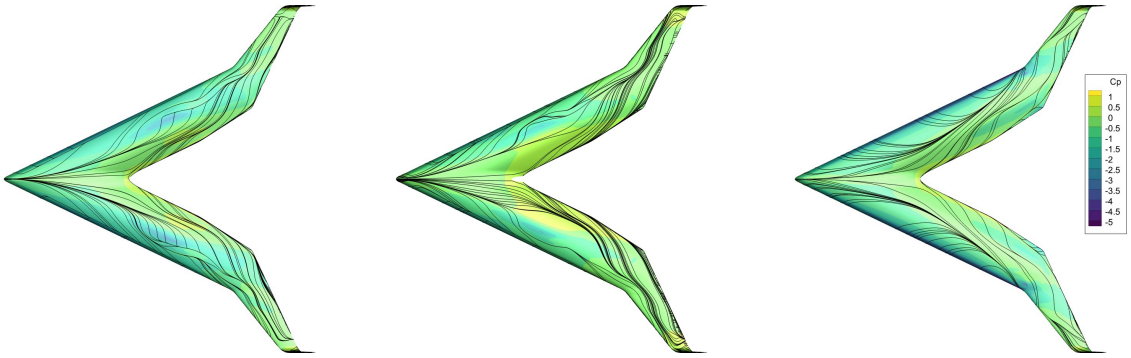

(a) Scaled **(b) Wind tunnel** **(c) Full-scale**

Figure 45. Flying V pressure coefficient contours and surface streamlines ($\alpha = 21.33°, \beta = 0°$)

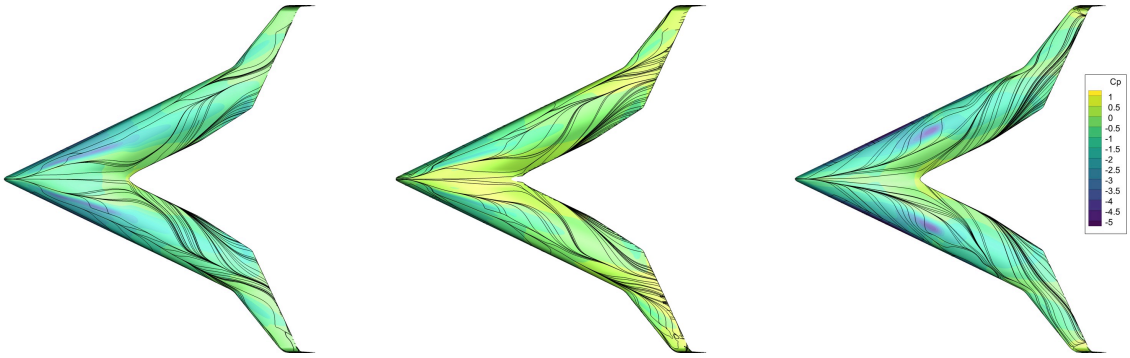

(a) Scaled **(b) Wind tunnel** **(c) Full-scale**

Figure 46. Flying V pressure coefficient contours and surface streamlines ($\alpha = 32°, \beta = 0°$)

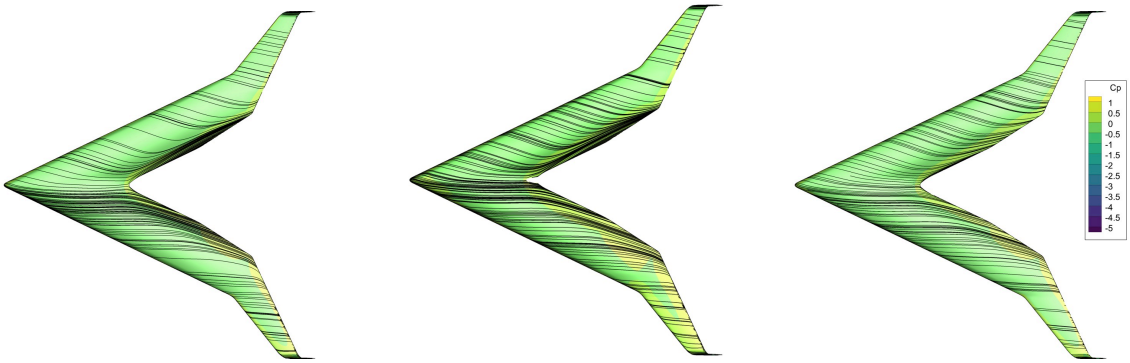

(a) Scaled **(b) Wind tunnel** **(c) Full-scale**

Figure 47. Flying V pressure coefficient contours and surface streamlines ($\alpha = 0°, \beta = 8.33°$)

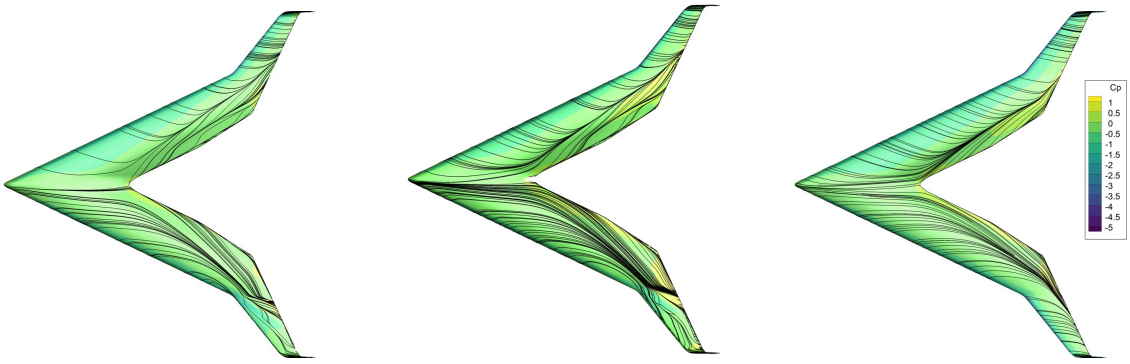

(a) Scaled **(b) Wind tunnel** **(c) Full-scale**

Figure 48. Flying V pressure coefficient contours and surface streamlines ($\alpha = 10.66°, \beta = 8.33°$)

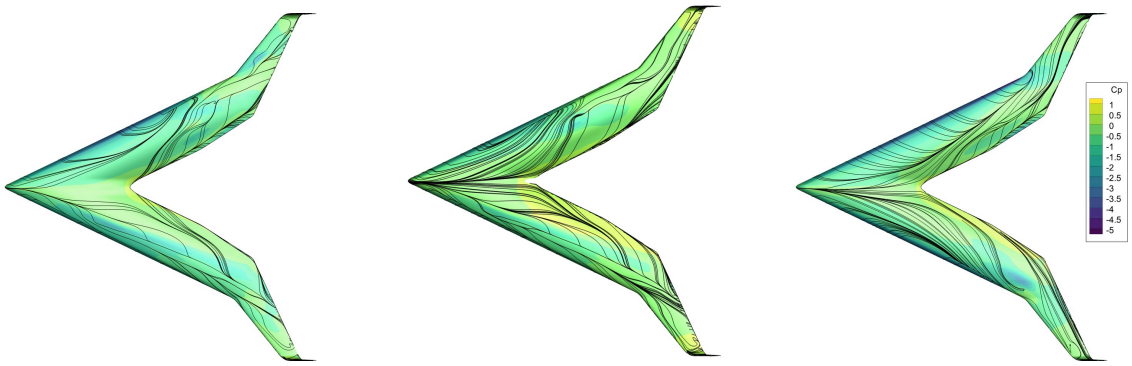

(a) Scaled **(b) Wind tunnel** **(c) Full-scale**

Figure 49. Flying V pressure coefficient contours and surface streamlines ($\alpha = 21.33°, \beta = 8.33°$)

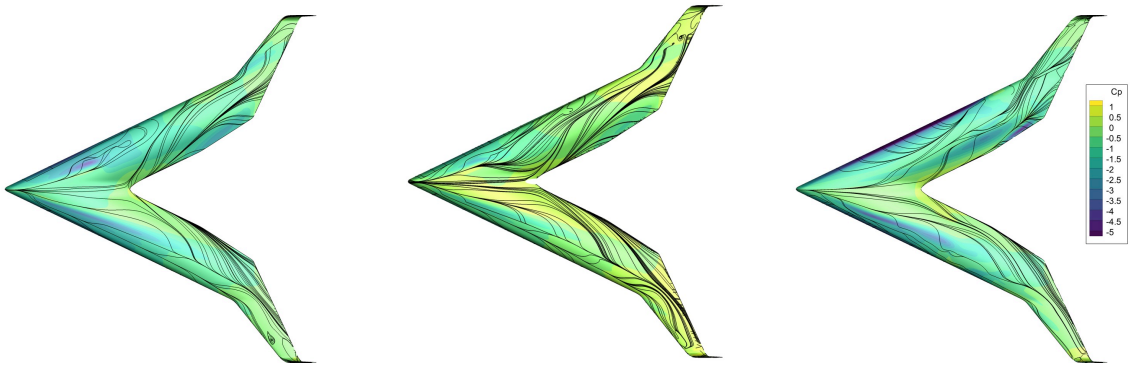

(a) Scaled **(b) Wind tunnel** **(c) Full-scale**

Figure 50. Flying V pressure coefficient contours and surface streamlines ($\alpha = 32°, \beta = 8.33°$)

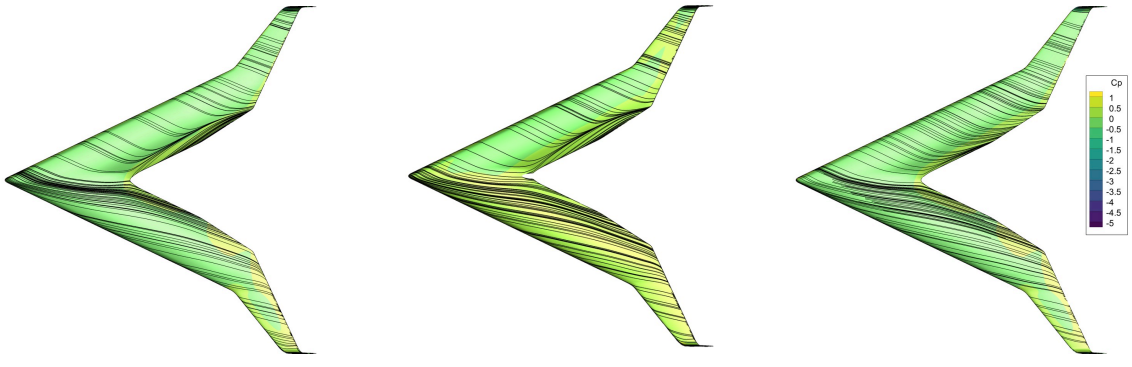

(a) Scaled **(b) Wind tunnel** **(c) Full-scale**

Figure 51. Flying V pressure coefficient contours and surface streamlines ($\alpha = 0°, \beta = 16.66°$)

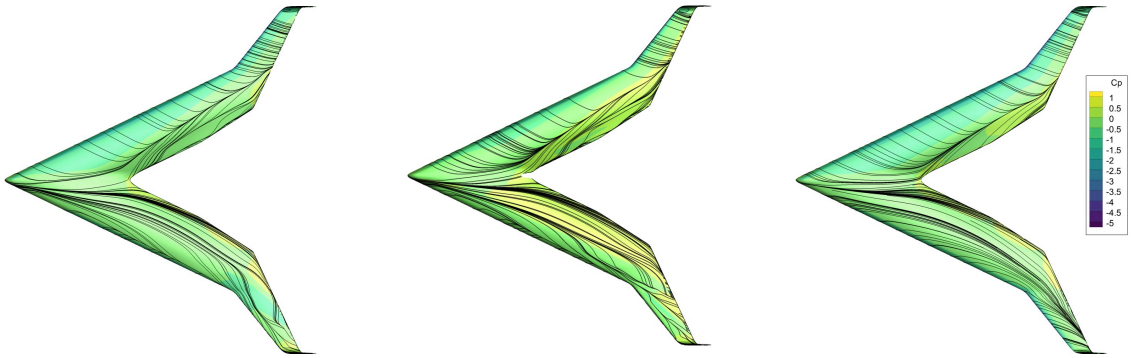

(a) Scaled **(b) Wind tunnel** **(c) Full-scale**

Figure 52. Flying V pressure coefficient contours and surface streamlines ($\alpha = 10.66°, \beta = 16.66°$)

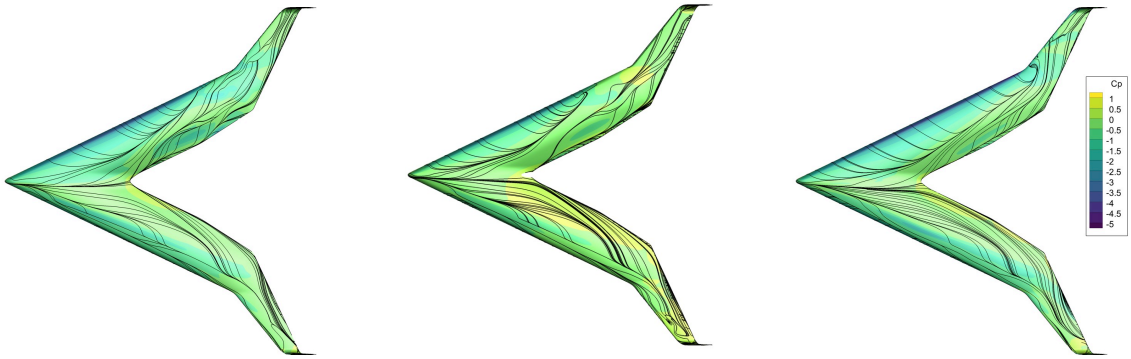

(a) Scaled **(b) Wind tunnel** **(c) Full-scale**

Figure 53. Flying V pressure coefficient contours and surface streamlines ($\alpha = 21.33°, \beta = 16.66°$)

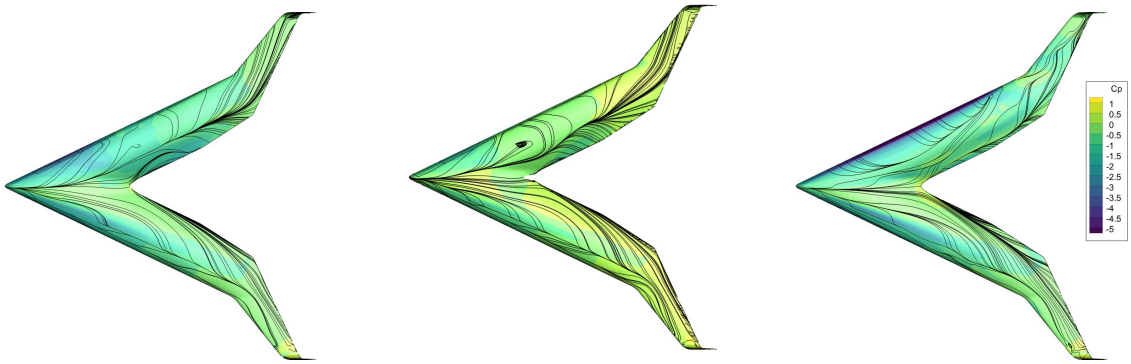

(a) Scaled **(b) Wind tunnel** **(c) Full-scale**

Figure 54. Flying V pressure coefficient contours and surface streamlines ($\alpha = 32°, \beta = 16.66°$)

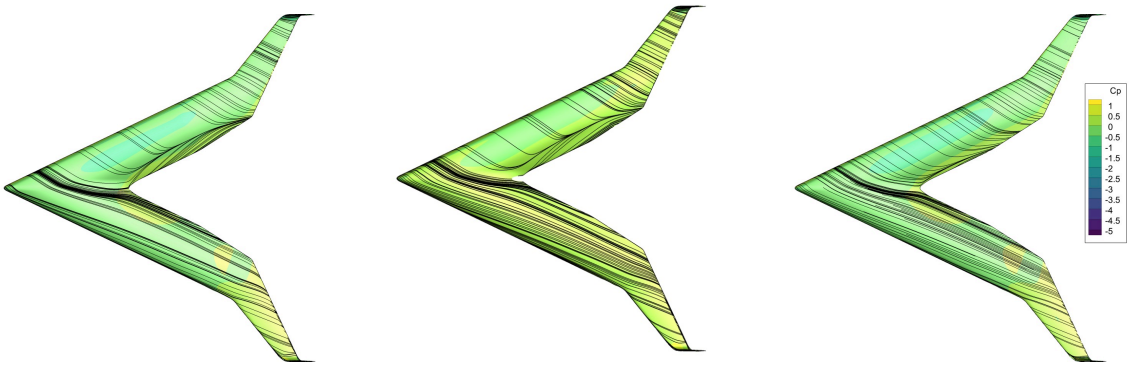

(a) Scaled **(b) Wind tunnel** **(c) Full-scale**

Figure 55. Flying V pressure coefficient contours and surface streamlines ($\alpha = 0°, \beta = 25°$)

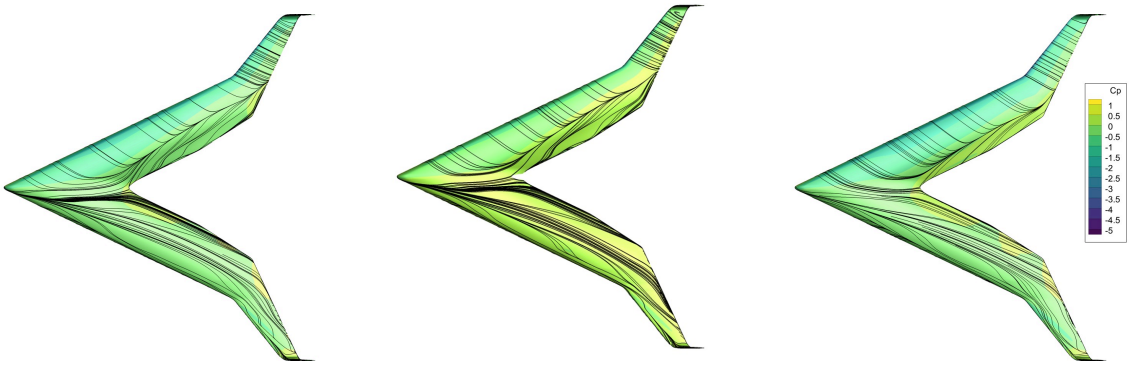

(a) Scaled **(b) Wind tunnel** **(c) Full-scale**

Figure 56. Flying V pressure coefficient contours and surface streamlines ($\alpha = 10.66°, \beta = 25°$)

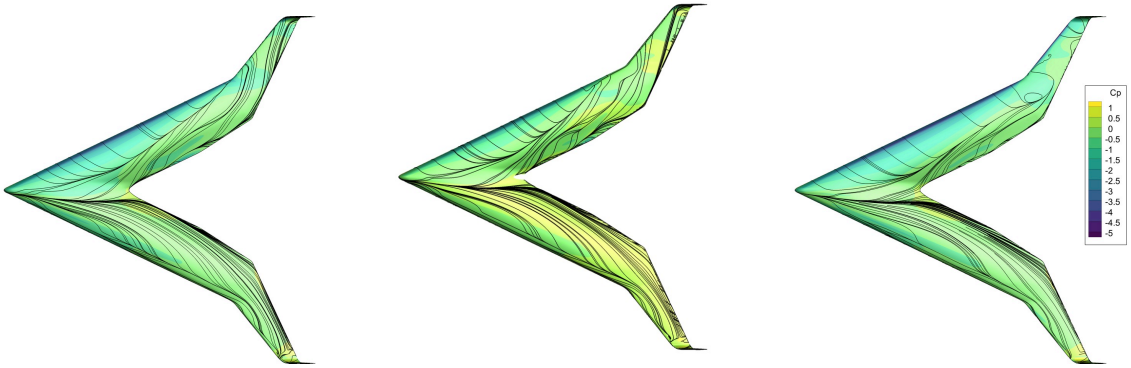

(a) Scaled **(b) Wind tunnel** **(c) Full-scale**

Figure 57. Flying V pressure coefficient contours and surface streamlines ($\alpha = 21.33°, \beta = 25°$)

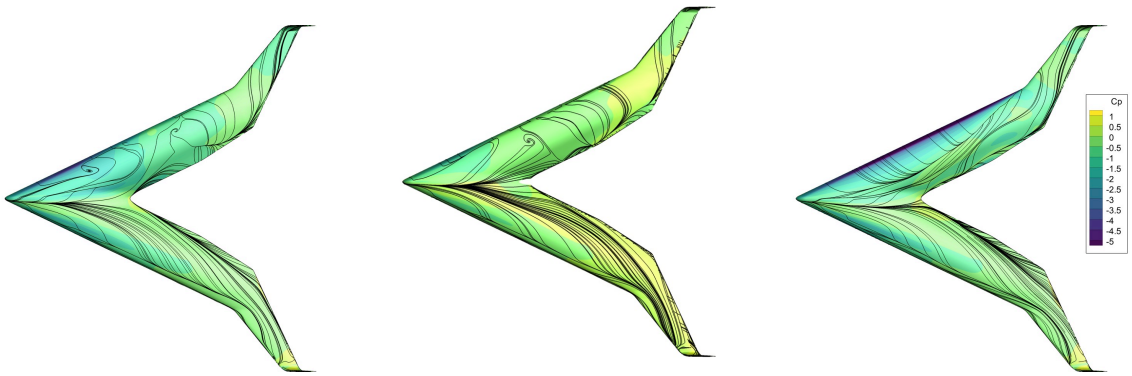

(a) Scaled **(b) Wind tunnel** **(c) Full-scale**

Figure 58. Flying V pressure coefficient contours and surface streamlines ($\alpha = 32°, \beta = 25°$)

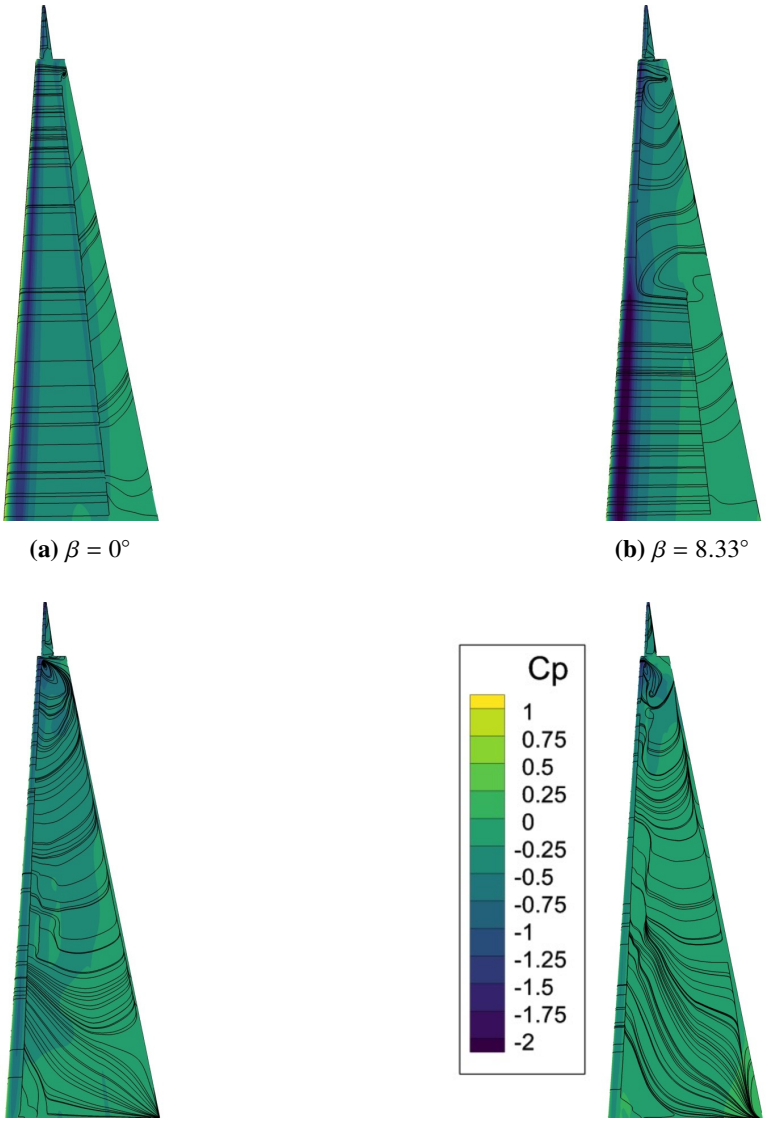

(a) $\beta = 0°$ **(b)** $\beta = 8.33°$

(c) $\beta = 16.66°$ **(d)** $\beta = 25°$

Figure 59. LTT strut pressure coefficient contours and surface streamlines

G. Pressure Loss Slices

(a) Scaled **(b) Wind tunnel** **(c) Full-scale**

Figure 60. Flying V total pressure loss at slices of constant x ($\alpha = 0°, \beta = 0°$)

(a) Scaled **(b) Wind tunnel** **(c) Full-scale**

Figure 61. Flying V total pressure loss at slices of constant x ($\alpha = 10.66°, \beta = 0°$)

(a) Scaled **(b) Wind tunnel** **(c) Full-scale**

Figure 62. Flying V total pressure loss at slices of constant x ($\alpha = 21.33°, \beta = 0°$)

(a) Scaled **(b) Wind tunnel** **(c) Full-scale**

Figure 63. Flying V total pressure loss at slices of constant x ($\alpha = 32°, \beta = 0°$)

(a) Scaled **(b) Wind tunnel** **(c) Full-scale**

Figure 64. Flying V total pressure loss at slices of constant x ($\alpha = 0°, \beta = 8.33°$)

(a) Scaled **(b) Wind tunnel** **(c) Full-scale**

Figure 65. Flying V total pressure loss at slices of constant x ($\alpha = 10.66°, \beta = 8.33°$)

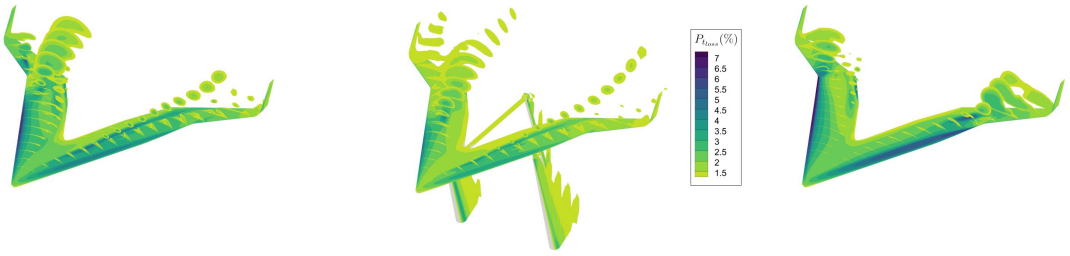

(a) Scaled **(b) Wind tunnel** **(c) Full-scale**

Figure 66. Flying V total pressure loss at slices of constant x **(**$\alpha = 21.33°, \beta = 8.33°$**)**

(a) Scaled **(b) Wind tunnel** **(c) Full-scale**

Figure 67. Flying V total pressure loss at slices of constant x **(**$\alpha = 32°, \beta = 8.33°$**)**

(a) Scaled **(b) Wind tunnel** **(c) Full-scale**

Figure 68. Flying V total pressure loss at slices of constant x **(**$\alpha = 0°, \beta = 16.66°$**)**

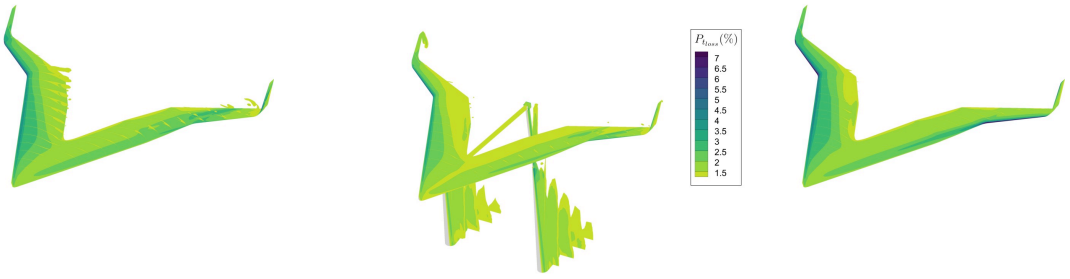

(a) Scaled **(b) Wind tunnel** **(c) Full-scale**

Figure 69. Flying V total pressure loss at slices of constant x **(**$\alpha = 10.66°, \beta = 16.66°$**)**

(a) Scaled **(b) Wind tunnel** **(c) Full-scale**

Figure 70. Flying V total pressure loss at slices of constant x **(**$\alpha = 21.33°, \beta = 16.66°$**)**

(a) Scaled **(b) Wind tunnel** **(c) Full-scale**

Figure 71. Flying V total pressure loss at slices of constant x **(**$\alpha = 32°, \beta = 16.66°$**)**

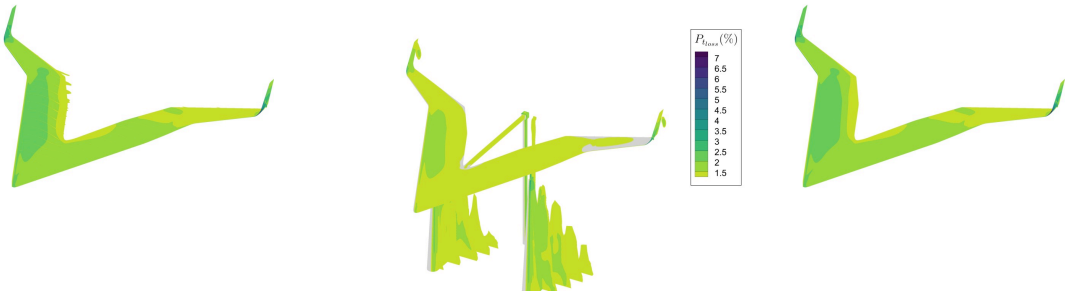

(a) Scaled **(b) Wind tunnel** **(c) Full-scale**

Figure 72. Flying V total pressure loss at slices of constant x ($\alpha = 0°, \beta = 25°$)

(a) Scaled **(b) Wind tunnel** **(c) Full-scale**

Figure 73. Flying V total pressure loss at slices of constant x ($\alpha = 10.66°, \beta = 25°$)

(a) Scaled **(b) Wind tunnel** **(c) Full-scale**

Figure 74. Flying V total pressure loss at slices of constant x ($\alpha = 21.33°, \beta = 25°$)

(a) Scaled **(b) Wind tunnel** **(c) Full-scale**

Figure 75. Flying V total pressure loss at slices of constant x **(**$\alpha = 32°, \beta = 25°$**)**

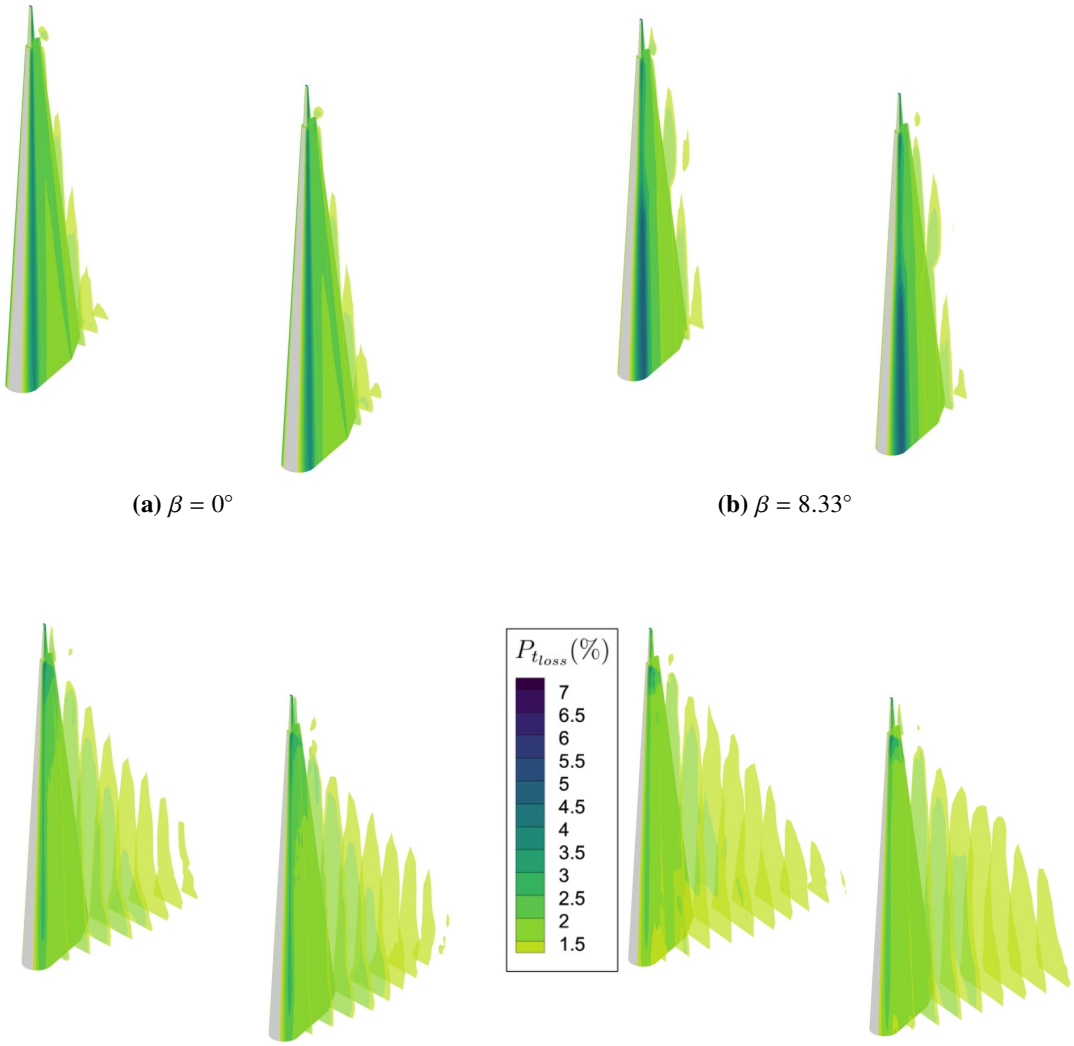

(a) $\beta = 0°$ **(b)** $\beta = 8.33°$

(c) $\beta = 16.66°$ **(d)** $\beta = 25°$

Figure 76. LTT strut total pressure loss at slices of constant x

H. Dimensionless Wall Distance Contours

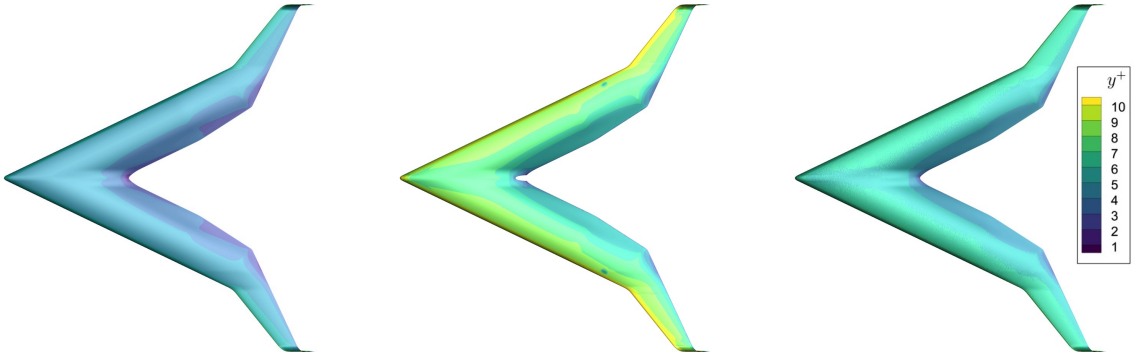

(a) Scaled **(b) Wind tunnel** **(c) Full-scale**

Figure 77. Flying V y^+ value over surface $(\alpha = 0°, \beta = 0°)$

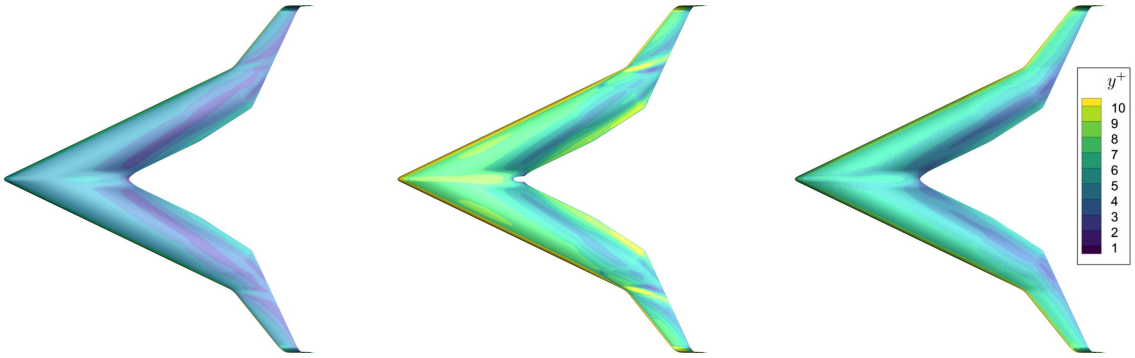

(a) Scaled **(b) Wind tunnel** **(c) Full-scale**

Figure 78. Flying V y^+ value over surface $(\alpha = 10.66°, \beta = 0°)$

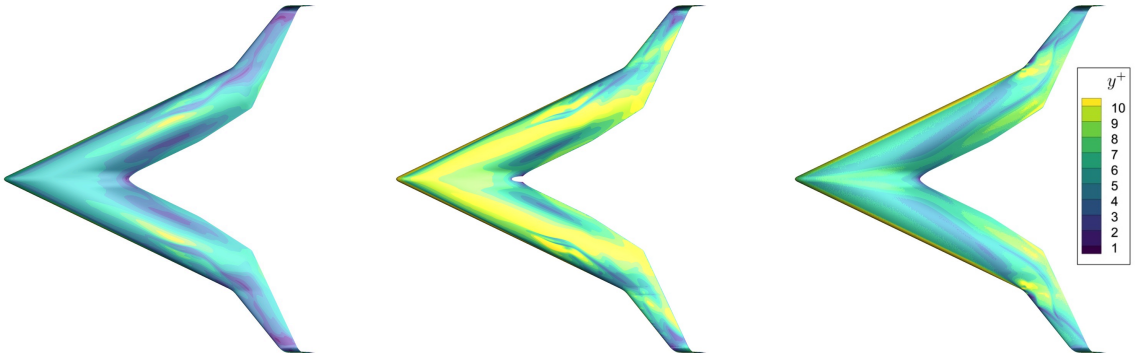

(a) Scaled **(b) Wind tunnel** **(c) Full-scale**

Figure 79. Flying V y^+ value over surface $(\alpha = 21.33°, \beta = 0°)$

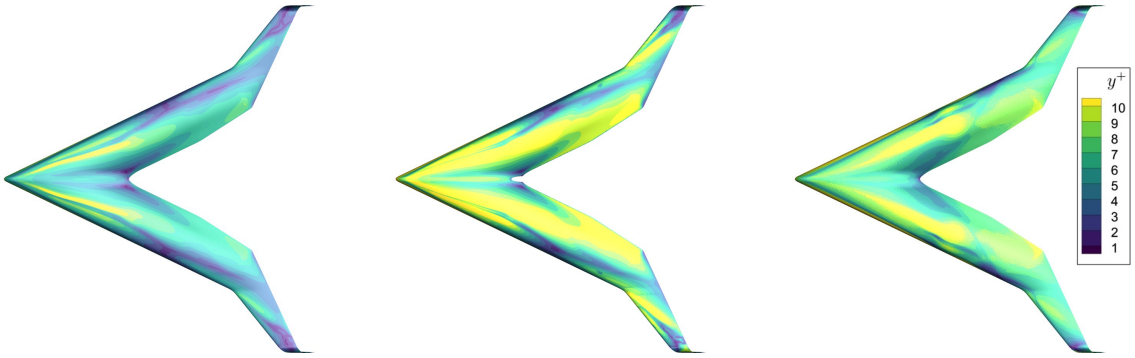

(a) Scaled **(b) Wind tunnel** **(c) Full-scale**

Figure 80. Flying V y^+ value over surface ($\alpha = 32°, \beta = 0°$)

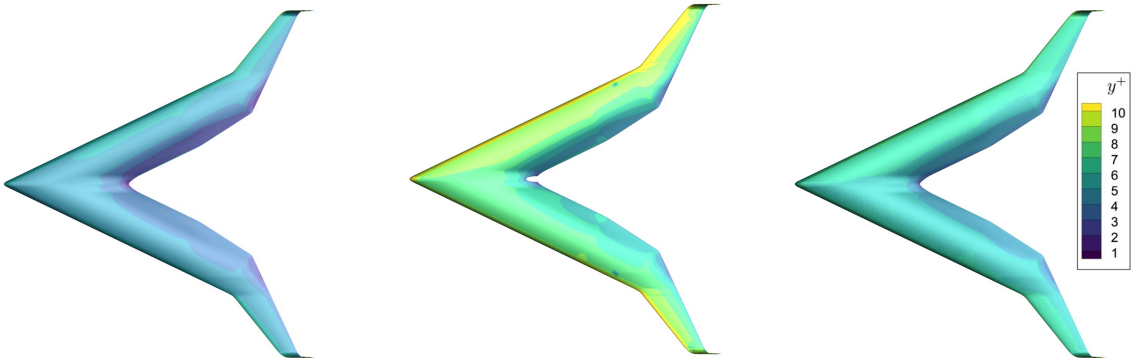

(a) Scaled **(b) Wind tunnel** **(c) Full-scale**

Figure 81. Flying V y^+ value over surface ($\alpha = 0°, \beta = 8.33°$)

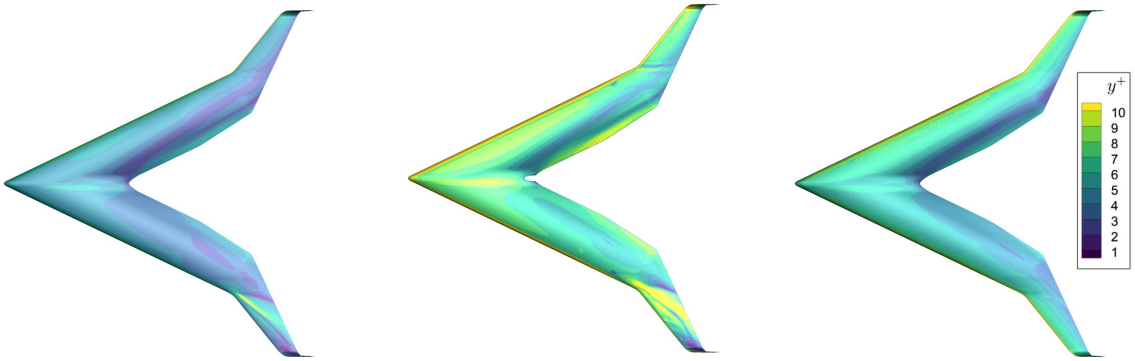

(a) Scaled **(b) Wind tunnel** **(c) Full-scale**

Figure 82. Flying V y^+ value over surface ($\alpha = 10.66°, \beta = 8.33°$)

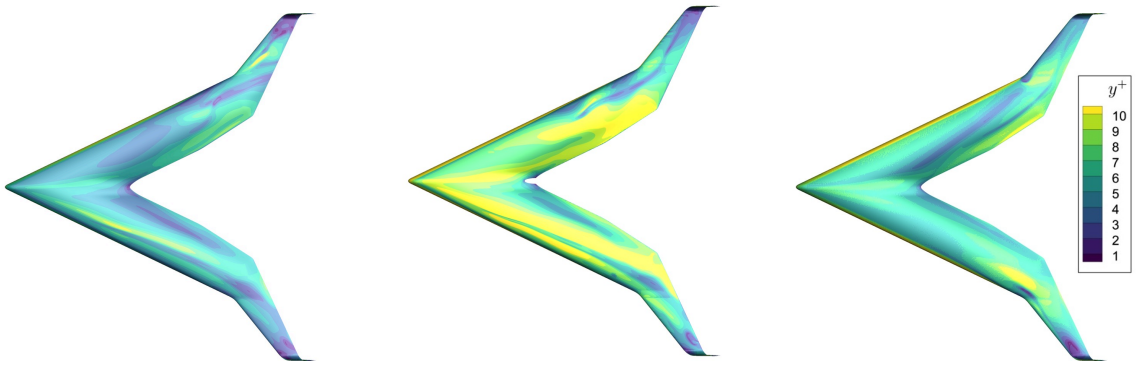

(a) Scaled **(b) Wind tunnel** **(c) Full-scale**

Figure 83. Flying V y^+ value over surface ($\alpha = 21.33°, \beta = 8.33°$)

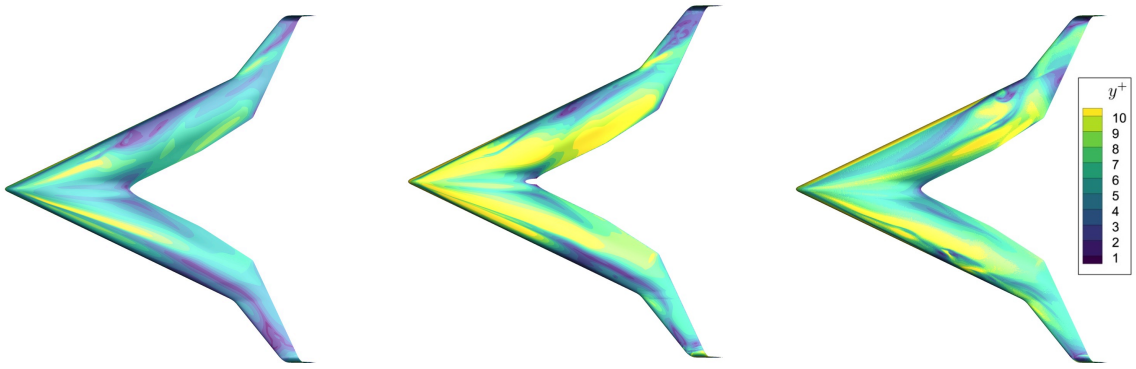

(a) Scaled **(b) Wind tunnel** **(c) Full-scale**

Figure 84. Flying V y^+ value over surface ($\alpha = 32°, \beta = 8.33°$)

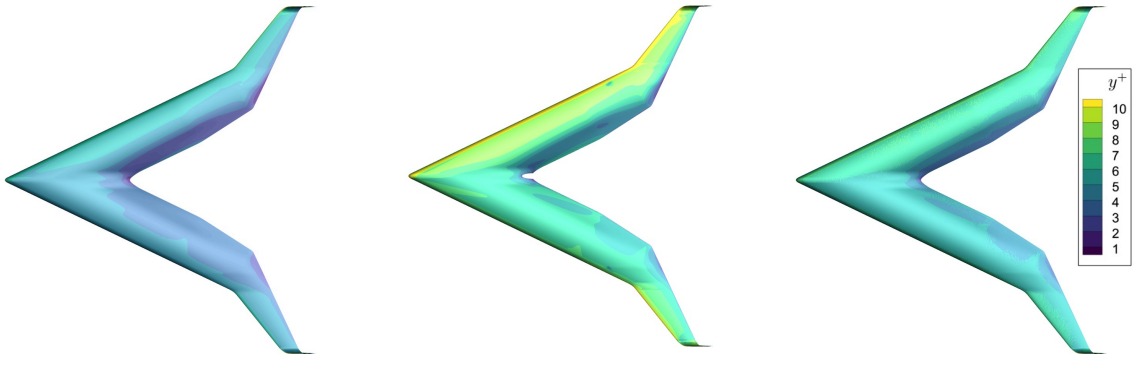

(a) Scaled **(b) Wind tunnel** **(c) Full-scale**

Figure 85. Flying V y^+ value over surface ($\alpha = 0°, \beta = 16.66°$)

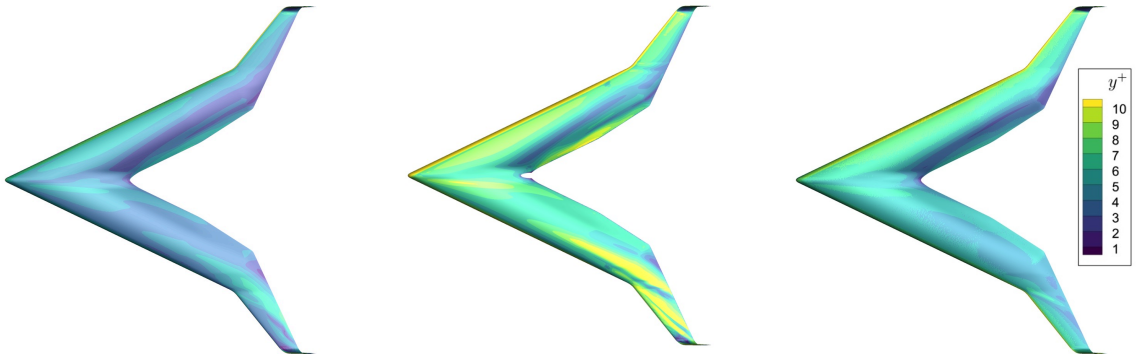

(a) Scaled **(b) Wind tunnel** **(c) Full-scale**

Figure 86. Flying V y^+ value over surface ($\alpha = 10.66°, \beta = 16.66°$)

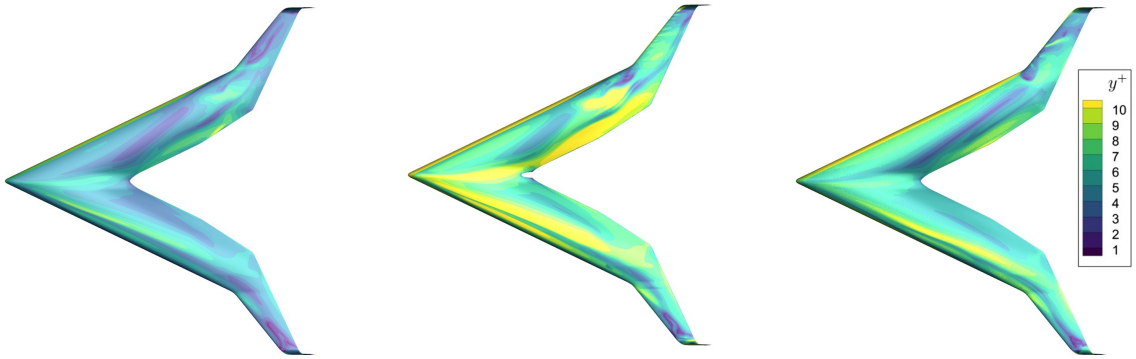

(a) Scaled **(b) Wind tunnel** **(c) Full-scale**

Figure 87. Flying V y^+ value over surface ($\alpha = 21.33°, \beta = 16.66°$)

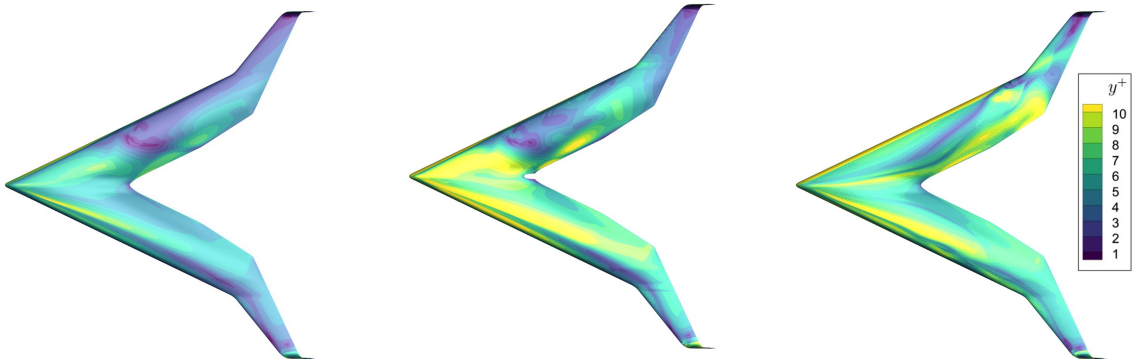

(a) Scaled **(b) Wind tunnel** **(c) Full-scale**

Figure 88. Flying V y^+ value over surface ($\alpha = 32°, \beta = 16.66°$)

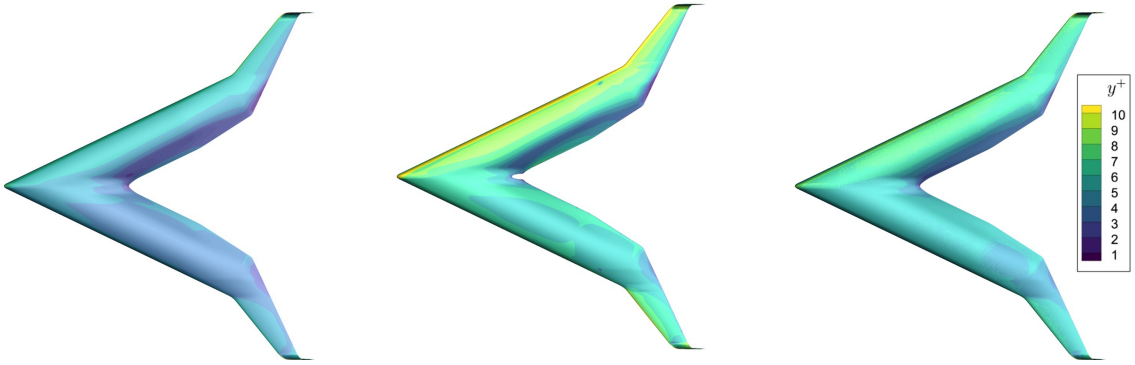

(a) Scaled **(b) Wind tunnel** **(c) Full-scale**

Figure 89. Flying V y^+ value over surface ($\alpha = 0°, \beta = 25°$)

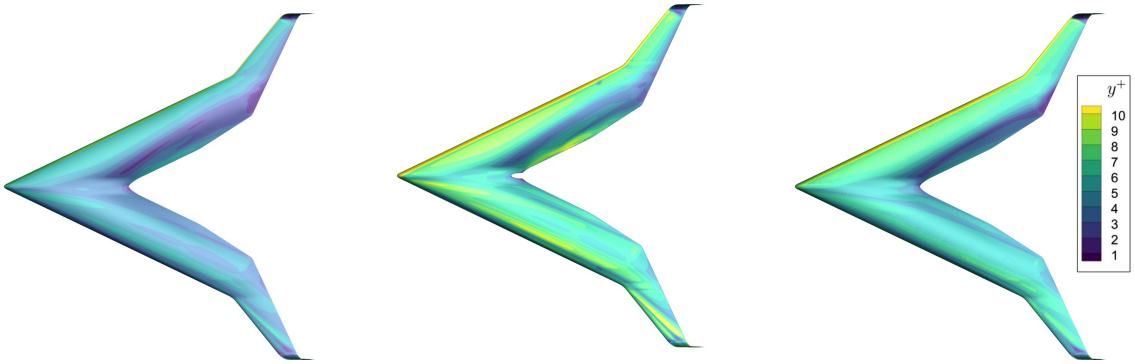

(a) Scaled **(b) Wind tunnel** **(c) Full-scale**

Figure 90. Flying V y^+ value over surface ($\alpha = 10.66°, \beta = 25°$)

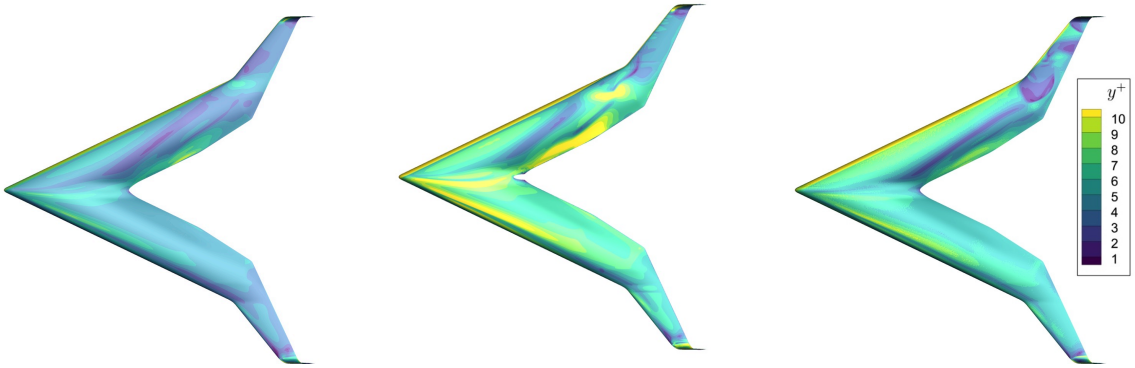

(a) Scaled **(b) Wind tunnel** **(c) Full-scale**

Figure 91. Flying V y^+ value over surface ($\alpha = 21.33°, \beta = 25°$)

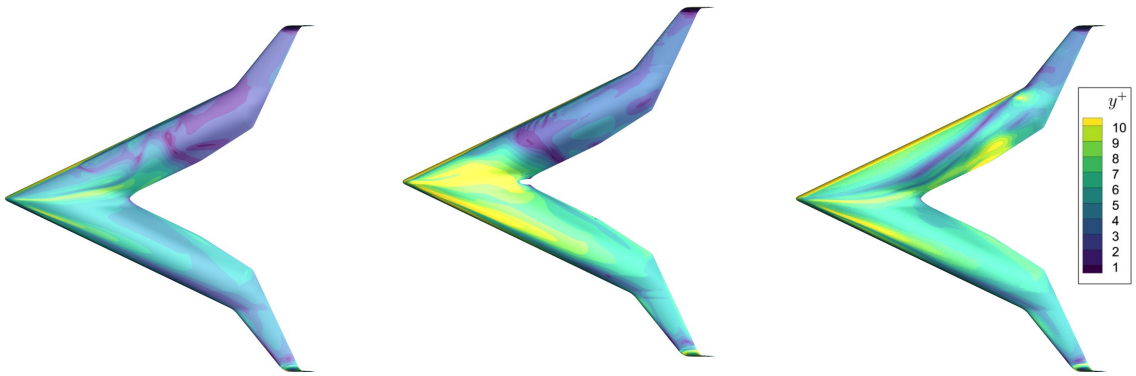

(a) Scaled **(b) Wind tunnel** **(c) Full-scale**

Figure 92. Flying V y^+ value over surface ($\alpha = 32°, \beta = 25°$)

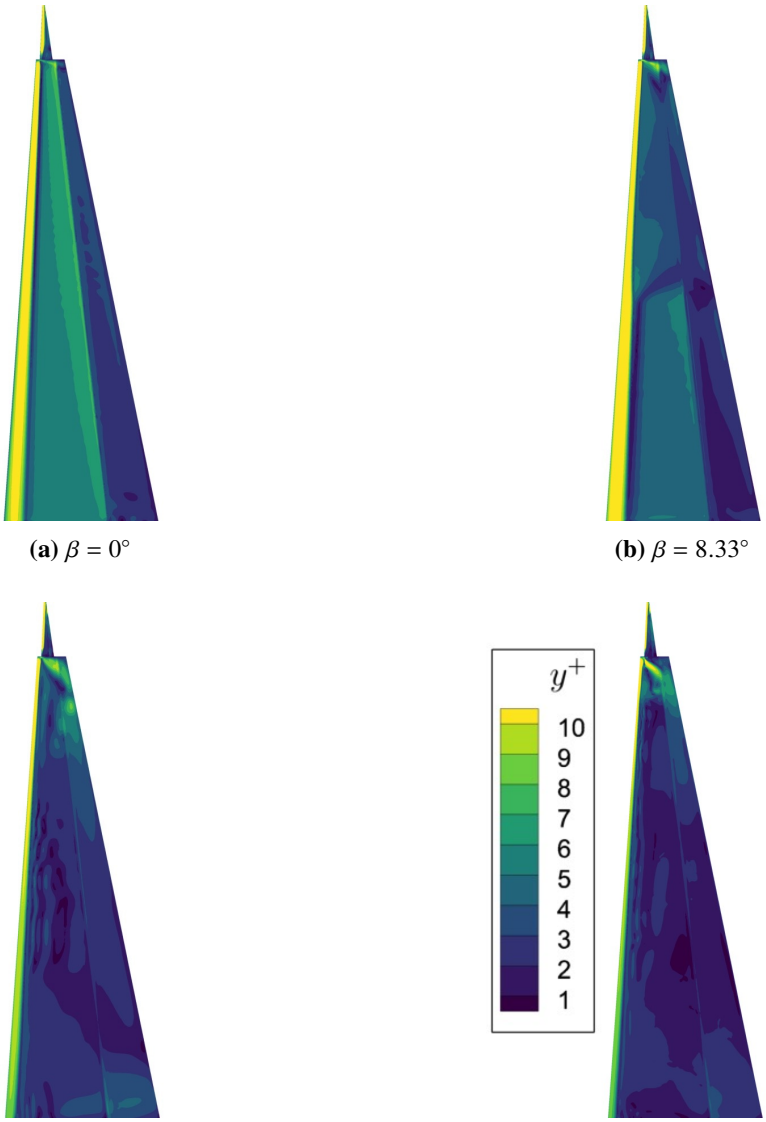

(a) $\beta = 0°$ **(b)** $\beta = 8.33°$

(c) $\beta = 16.66°$ **(d)** $\beta = 25°$

Figure 93. LTT strut y^+ value over surface

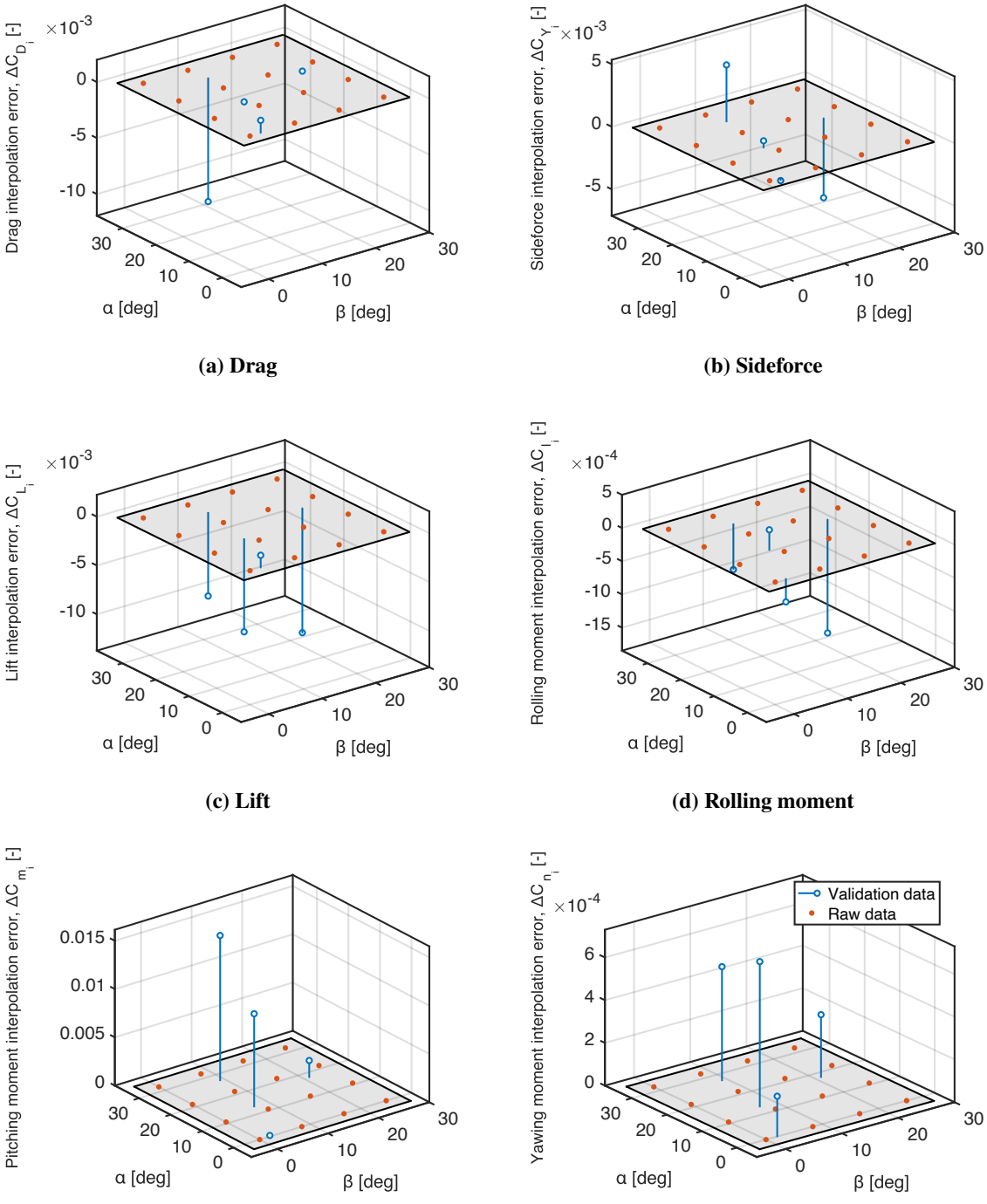

(a) Drag **(b) Sideforce**

(c) Lift **(d) Rolling moment**

(e) Pitching moment **(f) Yawing moment**

Figure 94. Interpolation errors of scaled Flying V interpolation validation runs

J. Residuals

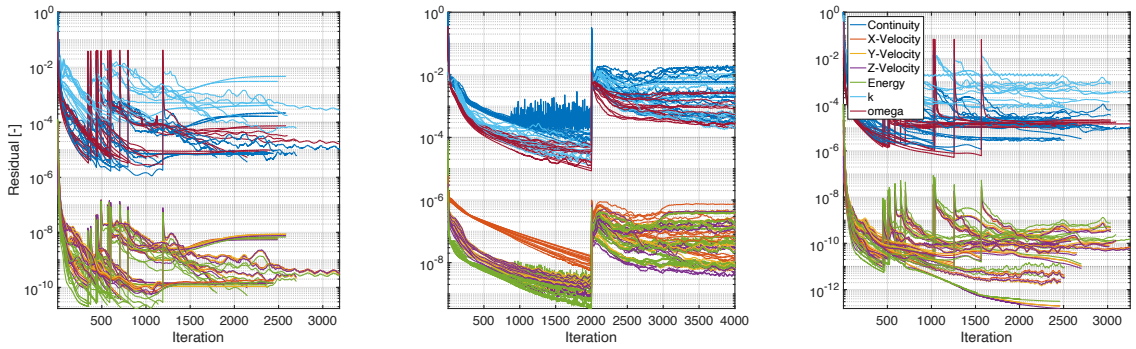

(a) Scaled **(b) Wind tunnel** **(c) Full-scale**

Figure 95. Convergence of Flying V simulation residuals

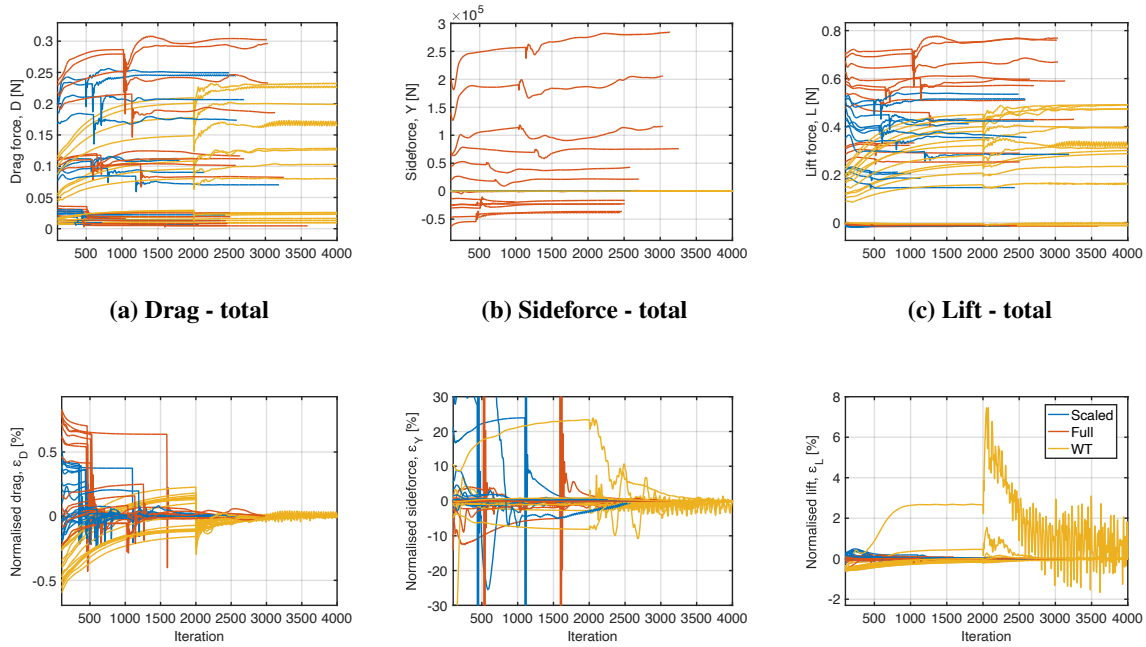

(a) Drag - total **(b) Sideforce - total** **(c) Lift - total**

(d) Drag - normalised **(e) Sideforce - normalised** **(f) Lift - normalised**

Figure 96. Convergence of Flying V body forces

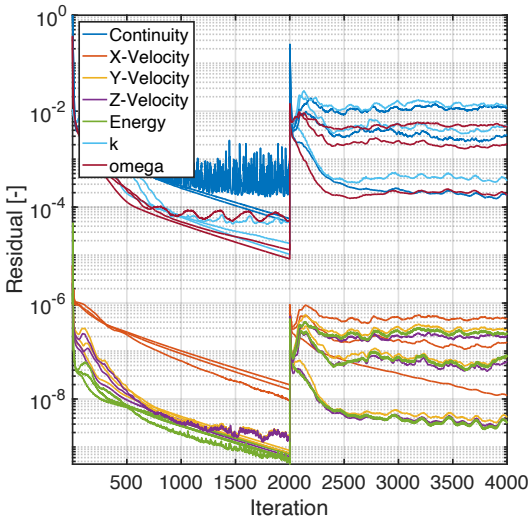

Figure 97. Convergence of LTT strut simulation residuals

K. Combined Wind Tunnel Corrections

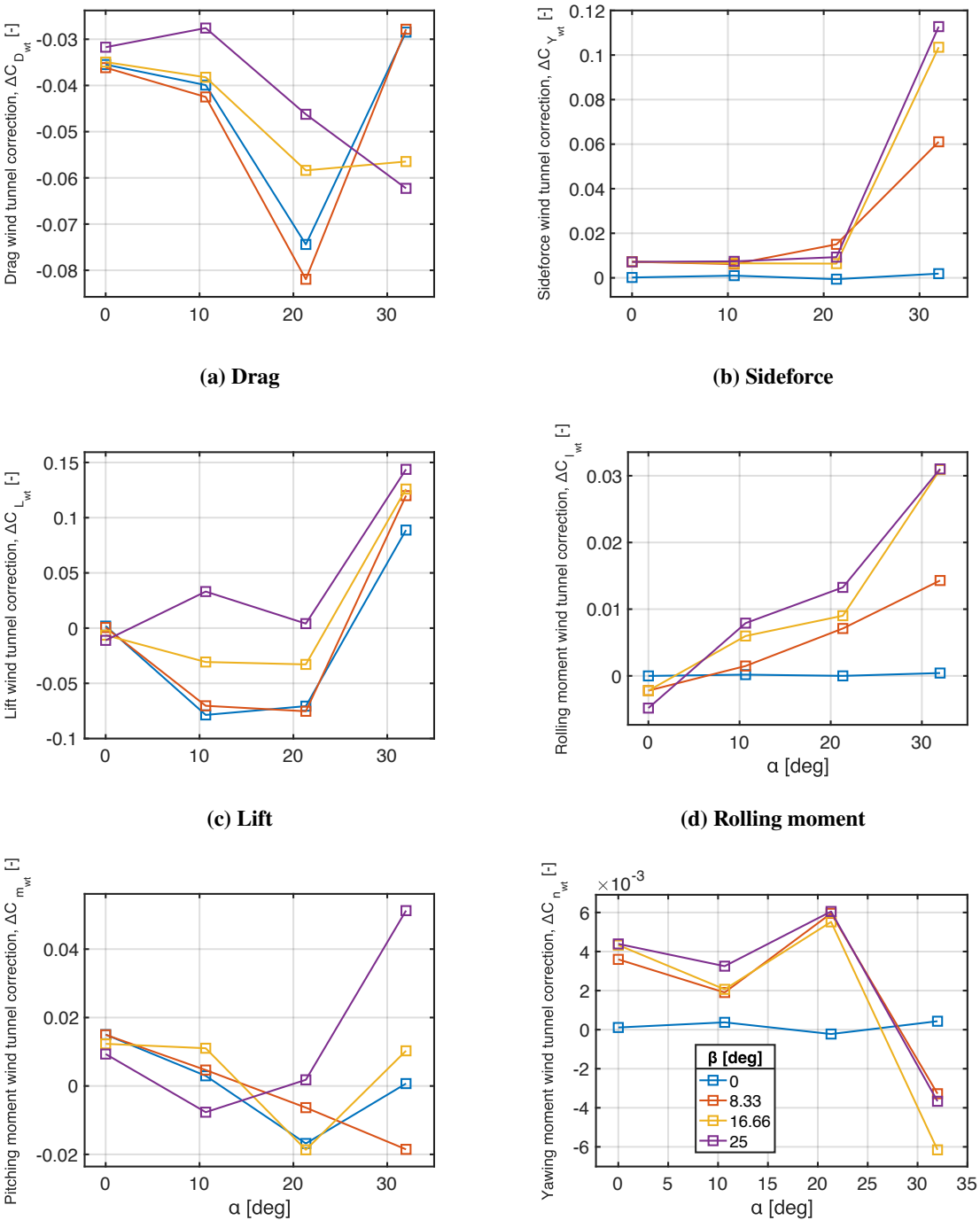

(a) Drag **(b) Sideforce**

(c) Lift **(d) Rolling moment**

(e) Pitching moment **(f) Yawing moment**

Figure 98. Deltas between wind tunnel and full-scale simulation data